Hydrothermal synthesis of nano-scaled pure, Sn-doped, and Zn-doped Co_3O_4 structures and their gas sensing applications

By

Letsoalo Modjadji Rebecca

(BSc. Hons)

Thesis presented in fulfilment of the requirements for the degree of

Master of Science

at the

University of Venda

Supervisor: Dr Katekani Shingange

Co-supervisor: Prof. Eric Maluta

February 2024

Declaration:

I, **Modjadji Rebecca Letsoalo [22020620]**, declare that this dissertation is my original work and has not been submitted for any degree at any other university or institution. The dissertation does not contain other persons' writing unless specifically acknowledged and referenced accordingly.

Signed:

Student:_____ Date: 28 February 2024

For my daughter, Khensani Bohlale Letsoalo

ACKNOWLEDGEMENTS

- I would like to express my deepest gratitude to **God**, whose presence has been a persistent companion throughout my academic journey, in all my needs. His grace has been sufficient for me.
- My sincere gratitude goes to my esteemed Supervisors, **Dr. Katekani Shingange and Prof. Eric Maluta** for their consistent support, guidance, love, and invaluable insights which helped shape my research process.
- I would like to extend my special thanks to **Dr. Katekani Shingange** for not only being my supervisor but also a nurturing figure, Dr. thank you for the academic and emotional support you have offered me, constructive feedback, and scholarly contributions that helped me grow in research. I owe my accomplishments to your mentorship; you are very much appreciated.
- A sincere thank you to **Mr. Steve Dima**, my research assistant.Your computational expertise greatly enriched the quality of my research.
- I am grateful to my family, especially my parents **Rosina and Klaas Letsoalo**, and my grandmother **Annah Diale** for their support, encouragement, and understanding that have been my pillars during this demanding academic journey. I appreciate and love you dearly. And to **Tshifhiwa Ranwaha and Kevin Malitsha (vho khotsi)**: In you guys, I have found lifetime brothers who always have my back and take good care of me, thank you!!
- Thanks to **Vhuthu Tshilengo** (mamas) for checking up on me from time to time and making sure I was well. And to **Takalani Nethavhanani** (makhadzi muhulu) for the positive compliments, they surely boosted me when I was at my lowest. **Ndo livhuwa.**
- Heartfelt gratitude to my daughter **Khensani**: mama you have brought so much joy and peace in my life. You're a little friend I have never had before. Those little feet distracted me and kept me smiling during my academic tough times. I hope to provide you with a good life I never had.
- Additionally, I acknowledge the financial support from the Department of Science and Innovation CSIR Inter-Programme Bursary that made this research possible.

- Many thanks to the CSIR Centre for Nanostructures and Advanced Materials (CeNAM) characterization facility for XRD, SEM, TEM, BET, UV-VIS, PL, and the University of Free State for XPS.
- This thesis represents my work and the collective efforts of a supportive community at CSIR, MINTEK, and the University of Venda. Thank you all for being part of this significant milestone in my academic career.
- I would like to thank **myself** for my determination and resilience in this journey. So many times, I experienced fatigue, shed tears, experienced impatience, and endured moments of hurt. In all these, I remained strong and never allowed the challenges I faced to overshadow the commitment to completing my work. Dear self, Thank you!!

Conference, publications, community engagements and honors

Conferences:

1. **M.R Letsoalo**, N.E Maluta, K Shingange,. "*Fabrication of Co_3O_4 nanostructures: Characterization and gas sensing applications*". 8th International Conference on Nanoscience and Nanotechnology in Africa (NanoAfrica 2022), The Lord Charles Hotel, Cape Town, South Africa, 26 – 28 October 2022. **(Oral presentation)**
2. **M.R Letsoalo**, N.E Maluta, K Shingange. "*Fabrication, characterization, and gas detection performance of Co_3O_4 hierarchical structures*". The 9th South African Conference on Photonic Materials (SACPM), Nombolo Mdhluli Conference Centre, Skukuza Rest Camp, Kruger National Park, South Africa, May 9-11, 2023. **(Oral presentation) 2nd prize best presentation**
3. **M.R Letsoalo**, S.R Dima, N.E Maluta, K Shingange. "*Gas sensing mechanism of Ethylene on Co_3O_4 (311) surface: Density Functional Theory Study*". The 67th Annual Conference of the South African Institute of Physics, University of Zululand Richards Bay Campus, South Africa, 03 – 07 July 2023. **(Poster presentation)**

Journal articles:

1. **Modjadji R. Letsoalo**, Thabang J. Theka, Eric N. Maluta, Katekani Shingange, "Review of resistive gas sensors based on cobalt dioxide and its modified counterparts" (**2024, submitted to journal)**
2. Boitumelo Mabakachaba, Nagla Numan; Katekani Shingange; Itani Given Madiba; **Modjadji Rebecca Letsoalo;** Zakhelumuzi Khumalo; Bhekumuzi Khanyile; Mlungisi Nkosi; Gugu Mhlongo; Sylvain Halindintwali; Malik Maaza, *"Mg-Functionalized Nanorods-based Sensor with Enhanced Sensing Performance for Toxic Gas Detection"* **(2024, submitted to journal)**

3. **Modjadji R. Letsoalo**, Steve R. Dima, Eric N. Maluta, and Katekani Shingange, "*Fabrication, characterization, and gas detection performance of Co_3O_4 sheet-like hierarchical structures: Experimental and DFT calculations*" **(under review)**

Book chapters:

1. Katekani Shingange, Steve R. Dima, **Modjadji R. Letsoalo** and Eric N. Maluta, "*2D Metal Oxides and their Heterostructures for Gas Chemical Sensing*", CRC Advanced Two-Dimensional Nanomaterials for Environmental and Sensing Applications. **(Book chapter accepted for publication)**

Conference proceedings:

1. K Shandukani, S.R Dima, **M.R Letsoalo**, T.S Ranwaha, N.E. Maluta, and R.R Maphanga, "Doping of Co and Ni to ZnO (101) surface using DFT Method: For gas sensing application", ISBN: 978-0-7961-3774-6, Proceedings of SAIP 2023. (Published)

Community engagements:

1. Physics comment magazine assistant for South African Institute of Physics(SAIP),01 September 2023-to date.
2. Role model speaker during National Science Week at Vuwani Science Center and Burgersfort region, 31 July 2023- 5 August 2023.
3. Presenter, on **Discover traditions of each country** during an International virtual exchange project named "DigiUp" hosted by Youth for Exchange and Understanding(YEU), 01 June 2023.
4. Role model speaker during the WIPISA event launch at Vuwani Science Center,10 March 2023.

5. Motivational speaker during Women in Physics in South Africa (WiPiSA) Empower her outreach to high school learners in Mpumalanga, 23 October 2022.
6. Role model speaker during science week outreach at Vuwani Science Center, 1 August 2022-6 August 2022.

Radio Interviews

1. Univen FM, SAWISA award Winner interview, 20 September 2023 at 14h30
2. Power FM, SAWISA(South African Women in Science awards) Finalist interview. 08 September 2023 at 16h00
3. Phalaphala FM, Nanomaterials education,20 July 2023 at 14h00
4. Makhado FM, Youth empowerment, 21 June 2023 at 14h15

Honors:

1. Winner for the South African Women in Science Awards (SAWiSA 2023) under the DSI Ndoni Mcunu Masters Fellowship category.
2. 2nd prize winner for student/post-doc oral presentation at the 9th South African Conference on Photonic Materials in 2023.
3. Nationally selected by ASSAF (Academy of Science of South Africa) to attend the 73rd Lindau Nobel Laureate Meeting dedicated to Physics on site from 30 June – 5 July 2024 in Germany.

Table of Contents

LIST OF FIGURES

Chapter 1

Introduction

1.1 Overview

Nanotechnology is increasingly enticing attention and investments globally. Nanotechnology functions at the nanoscale level, i.e., the first level of an atom and molecule body, which forms the starting point for the definition of materials' fundamental and functional properties [1]. Through nanotechnology, the knowledge and understanding of the material can be acquired, leading to the discovery of fundamentally new applications and the first steps towards industrial prototyping and commercialization. Therefore, the control of materials at the nanoscale is necessary to achieve novel, wide-ranging and innovative technologies, and platforms for different areas of interest, such as medicine, energy conversion, industry, security, and food resources quality control. Particularly, nano-sensors have an increasing impact on many aspects of everyday life as they act as an interface to obtain chemical information out of the surroundings in real time [2]. With the obtained information, control systems will be able to give feedback on a variety of chemical processes such as detection of explosives, and toxic gases, alarming systems for gas appliances, security systems to identify chemical hazards, environmental monitoring, health, and food security control.

However, for chemical sensors to be used in real applications, they should satisfy strict requirements such as sensitivity, good selectivity, fast response kinetics, and reliability. These requirements are heavily interrelated with the materials used and hence the importance of materials design as it is the basis of the development of novel gas sensor technologies. For that reason, the control of material design in the research and development of chemical sensors is vital.

Chemical sensors are divided into different classes based on the transduction principle: electrochemical, optical, mass sensitive, magnetic, thermometric, and electrical [3]. Out of all these sensors, most research attention has been fixated on electrical sensors; specifically, semiconductor metal oxide (SMO) based gas sensors. SMO-based sensors are characterized by changes in resistance when in contact with gas molecules. Changes in the resistance are caused by the release of electrons from the gas molecule to the SMO sensing material or vice versa. Usually, electron transfer takes place when SMOs are operated at a high working temperature. The optimum working temperature varies based on the sensing material used and the target gas molecules. As much as SMOs are interesting, they suffer from poor selectivity, this

means that they respond to different types of gas molecules, but with a different sensitivity per gas species. Due to this character, SMO-based sensors can be applied to diverse applications [4,5]

One of the applications that can benefit from using SMO-based gas sensors is the food industry. There are different shelf-life stages of food products including production, storage, shipment, and consumption. Physical, biological, and chemical reactions can occur in a food product during the shelf life and these reactions can cause modifications to the food product that can negatively affect the food product's quality and safety. So, it is very critical to have reliable sensors for accurate detection for use in different applications in the shelf-life stages of food products.

Amongst the many SMO-based materials, spinel cobalt oxide (Co_3O_4) has been studied as a potential material for gas sensing applications. Co_3O_4 has p-type conductivity with an indirect band gap of 1.6-2.2 eV [6]. Co_3O_4 has high catalytic properties which make it suitable for gas sensing applications [7]. Different strategies to modify and improve its sensing capabilities have been ventured into and these include morphology control, formation of heterostructures, and doping.

This project aspires to venture into the use of Co_3O_4 -based electrical gas sensors for application in the monitoring of gases as per applications specific to the food industry sector. The focus will be on optimization of the Co_3O_4 sensing layer for sensitive and specific detection of gases and Volatile organic compounds (VOCs) with the drive of generating innovative solutions toward food quality assurance throughout the entire supply chain in the food industry.

1.2 Problem statement

In many developing and established countries, the food industry is one of the industries that improve the economy. Nevertheless, there is a rise in illnesses due to the consumption of spoiled, pathogenic infested, adulterated, or contaminated foods. So, monitoring and detection of contaminants are very crucial in food securityand this requires simple, less costly, and fast detection techniques which is currently a key problem. Many foodstuffs release certain traces of gases and volatile organic compounds during freshness deterioration, and such gases or VOCs can be used to monitor the freshness level. Owing to their small size, portability, less cost, and easy modification and fabrication, chemical sensors especially those fabricated from semiconductor metal oxides caught a lot of attention recently. Still, SMOs-based chemical sensors have drawbacks like high operating temperature and poor selectivity. To overcome these problems and enhance the SMO sensing performance, doping, noble metals sensitization and formation of heterostructures have been found as viable solutions.

1.3 Justification of the study

The food industry is considered one of the pillars of the economies of several developing and developed nations. However, any contamination, adulteration, spoilage, or pathogenic infestation of food/agricultural products can potentially reduce their nutritive values. In addition, the accidental ingestion of contaminated food can lead to a variety of foodborne illnesses. Therefore, the development of novel sensitive detection techniques capable of monitoring food and agricultural analytes using faster, simpler, and less expensive detection methods continues to be a major challenge and is highly pursued. By far, a substantial advancement of freshness detection has been achieved through the use of gas chromatography-mass spectrometry (GC-MS) combined with headspace solid-phase microextraction (HS-SPME), yet detection equipment such as GC-MS is costly, it requires a complex pre-treatment process, and its real-time performance is poor. Thus, the gas sensor technology has become an imperative implement to replace human senses and GC-MS technology for freshness preservation and food quality status monitoring

Chemical sensors based on semiconductor metal oxides such as cobalt oxide have the potential to complement or even replace the classical analytical methods due to their advantageous features such as low cost, simple sample preparation, miniaturization, and portability. However, chemical sensors based on Co_3O_4 suffer challenges such as poor selectivity and high power consumption. A powerful strategy to bypass these challenges and improve the sensing characteristics of the Co_3O_4-based sensors relies on increasing the specific surface area as the larger the surface area of a sensing material the higher its ability to interact with the analyte gas. In this case, nanomaterials play an important role as they offer the possibility of tailoring the material's size and surface functionalities thus improving the gas sensing performance. Additives on the surface or lattice of SMOs have proven to be an effective way as they improve the catalytic activity of the sensing material, thus improving the overall sensing performance.

1.4 Aim of the study

This project is aimed at the development of nano-enabled Co_3O_4-based gas sensors for the detection of various gases in the agriculture and food industry space. The experimental development of the nanomaterials will be coupled with theoretical studies through computational calculations for a better understanding of the interaction between target gas molecules and the nanomaterials.

1.5 Specific objectives of the study

To achieve the aim of the study, the following objectives must be met:

1.1.1 Synthesis and characterization of nanostructured Co_3O_4

1.1.2 Sensitization of Co_3O_4 with metal additives (Sn/Zn)

1.1.3 Fabrication of Co_3O_4-based sensors and sensing test measurements

1.1.4 Computational calculations of response mechanisms on the Co_3O_4-based sensors

1.6 Hypothesis

If the addition of metal additives to nanostructured Co_3O_4 can improve its microstructural and chemical properties, then the gas sensing properties of nanostructured Co_3O_4 can be enhanced.

1.7 Chapters arrangement

Chapter 1: Introduction

Chapter 2: Literature Review

Chapter 3: Methodology

Chapter 4: Results and discussion

Chapter 5: Conclusion and future work

1.8 References

[1] M.C. Roco, C.A. Mirkin, M.C. Hersam, Nanotechnology research directions for societal needs in 2020: summary of international study, J Nanopart Res . 13 (2011) 897-919.

[2] F. Fan, P. Tang, Y. Wang, Y. Feng, A. Chen, R. Luo, D. Li, Facile synthesis and gas sensing properties of tubular hierarchical ZnO self-assembled by porous nanosheets, Sensors Actuators B: Chem. 215 (2015) 231-240.

[3] A. Hulanicki, S. Glab, F. Ingman, Chemical sensors: definitions and classification, Pure Appl. Chem. 63 (1991) 1247-1250.

[4] H. Kim, A. Haensch, I. Kim, N. Barsan, U. Weimar, J. Lee, The role of NiO doping in reducing the impact of humidity on the performance of SnO_2-Based gas sensors: synthesis strategies, and phenomenological and spectroscopic studies, Adv. Funct. Mater. 21 (2011) 4456-4463.

[5] J. Kim, K. Yong, Mechanism study of ZnO nanorod-bundle sensors for H_2S gas sensing, J. Phys. Chem. C. 115 (2011) 7218-7224.

[6] C. Zhang, L. Li, L. Hou, W. Chen, Fabrication of Co_3O_4 nanowires assembled on the surface of hollow carbon spheres for acetone gas sensing, Sensors Actuators B: Chem. 291 (2019) 130-140.

[7] S. Vladimirova, V. Krivetskiy, M. Rumyantseva, A. Gaskov, N. Mordvinova, O. Lebedev, M. Martyshov, P. Forsh, Co_3O_4 as p-type material for CO sensing in humid air, Sensors. 17 (2017) 2216.

Chapter 2

Literature review

2.1 Introduction

The search for extremely sensitive, reliable gas-sensing materials remains a top priority in the constantly changing world of materials research and sensor technologies. Environmental monitoring, industrial process control, medical diagnostics, and security are just a few of the fields in which gas sensors are of great value. The core component of these sensors is the sensing material which can range from metal-oxide semiconductors [1], conducting polymers and polymer composites [2-4], and carbon nanomaterials [5]. Depending on the transduction mechanism, these materials convert chemical interactions with certain gases into quantifiable electrical signals. Semiconductor metal-oxides (SMO) such as SnO_2, ZnO, NiO, CuO, and Co_3O_4 have emerged as the most exploited materials for gas-sensing applications [6-10]. The reason for their appeal is their sensitivity towards a variety of gases, low cost, robustness, and ease of incorporation into electronic devices [11].

SMO-based sensor transduction mechanism is on the change of the applied sensing material's resistance upon interaction with the target gas. This mechanism is a surface-based process that involves a catalytic reaction between the gas and the sensor surface. The mechanism and overall gas sensing performance are reliant on several factors such as the type of SMO (p-/n-type), type of gas (reducing or oxidizing), morphology, surface area, porosity, defects, operation temperature, and humidity conditions of the environment [12-14]. Thus, it is important to tailor the properties of the SMO material based on the intended application.

In this chapter we seek to explain the present state of knowledge and research around Co_3O_4 through an in-depth overview of the potential of Co_3O_4 to revolutionize the field of gas sensing technology through a comprehensive exploration of its fundamental properties, synthesis techniques, and performance characteristics. The complex mechanics underlying its gas-sensing behavior, highlighting the variables affecting its sensitivity, selectivity, and stability will also be explored. This will be achieved by first discussing the fundamentals of Co_3O_4, the design and fabrication of Co_3O_4 nanostructures and sensors, followed by the gas sensing performance towards different gases as reported in recent literature.

2.2 The interest behind Cobalt oxide

SMO-based gas sensors, which come in both p-type and n-type variants, address the need for gas detection. P-type SMO-based sensors often face limitations due to their high electrical resistance and lower sensitivity to gases in dry air when compared to n-type oxides [7]. However, they do exhibit excellent gas sensing performance, owing to their unique attributes, including robust conduction paths, resistance to humidity, higher catalytic properties, and long-term stability [15]. Moreover, p-type SMO-based sensors excel in adsorbing oxygen at low temperatures, leading to high oxidation levels on their surfaces compared to surface lattice oxygen [16-18]. On the other hand, n-type materials are highly sensitive to humidity, making them challenging to use in outdoor settings. Despite these initial differences and challenges, both p-type and n-type SMO-based sensors offer distinctive benefits and find applications in various fields. Understanding the strengths and weaknesses of each type is crucial for selecting the right sensor for specific use cases. The gap between their study and application may close as science and technology grow, stimulating breakthroughs and improvements in both types of gas sensors.

In the last decade, there has been some research interest in Co_3O_4 due to its gas-sensing properties such as being highly selective and stable when used as a sensing material. Co_3O_4 has a spinel crystal structure and crystallizes in the cubic Fd-3m space group. Co^{2+} is bonded to four equivalent O^{2-} atoms to form CoO tetrahedra that share corners with other tetrahedra to form a three-dimensional network. The structure is based on a cubic closed-packing structure of oxide ions with a lattice constant of approximately 8.08 Å [19]. The interatomic distance that was first observed between the Co1 and O1 atoms is 1.95 Å [20]. Cossee et al. [21] showed from magnetic measurements that Co_3O_4 possesses the normal spinel structure A[B2]O~, with the Co^{2+} and Co^{3+} ions occupying tetrahedral (A-site) and octahedral (B-site) coordination sites [22], as depicted in **Figure 2.1**. The presence of both Co^{2+} and Co^{3+} ions in the structure allows for variable oxidation states which contributes to the effectiveness of spinel Co_3O_4 gas sensing performance by allowing redox reactions to occur, making the material sensitive to both reducing and oxidizing gases.

For instance, reducing gases can cause Co^{3+} ions to be reduced to Co^{2+} ions, leading to increased electrical conductivity, while oxidizing gases can oxidize Co^{2+} ions to Co^{3+} ions, causing a decrease in conductivity. Lastly, the presence of cobalt ions can aid in tailoring the material's sensitivity through adjustment of the ratio of Co^{2+} to Co^{3+} ions or by incorporating dopants, which increases the concentration of Co^{3+} ions that

might enhance sensitivity to reducing gases, whereas increasing the concentration of Co^{2+} ions could enhance sensitivity to oxidizing gases. Giri et al [23] reported on a sensing mechanism for both oxidizing and reducing gases using Co_3O_4 powders through Cu-doping towards CO as a reducing gas and O_2 as an oxidizing gas. The Cu-doped Co_3O_4 nanoscale powders exhibited high sensitivity towards 6 ppm CO compared to when exposed to O_2. This was attributed to an increase in Co^{3+} as adsorption sites contributed by Cu-doping that led to enhanced sensitivity towards CO gas. As a result of the higher sensitivity, response, recovery, and stability even at low and high temperatures, scientific work on Co_3O_4 gas-sensing applications has gradually grown [24,25].

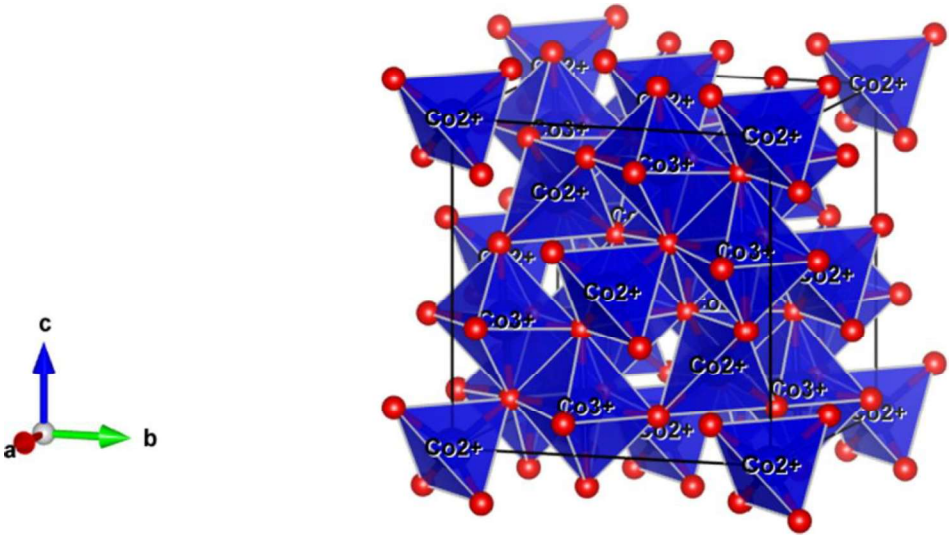

Figure 2. 1: Crystal structure of Co_3O_4 [23].

2.3 Co_3O_4 processing methods

Co_3O_4 nanostructures have been created using a variety of synthesis methods including hydrothermal, electrospinning, solvothermal, thermal decomposition, and sol-gel [18,19,26]. Each technique allows for the creation of Co_3O_4 nanostructures with a variety of morphologies, from zero-dimensional (0D) to three-dimensional (3D) networks. The configuration and structure of the atoms or molecules within the nanomaterial govern the classification of nanostructures into 0–3D. Nanoparticles and nanospheres are examples of 0D nanomaterials, which have all dimensions at the nanometric scale. Nanowires, nanorods, nanotubes, and nanofibers are examples of 1D nanostructures, which are made up of just one dimension that is larger than a nanometer. Nanoprisms, nanoplates, nanodiscs, nanoflakes, and nanosheets are

examples of 2D nanomaterials, while nanoflowers, nanocubes, and hollow nanospheres are examples of 3D nanostructures [27,28]. The choice of synthetic method of Co_3O_4 generally depends on the desired properties as well as applications. For gas sensing applications, different aspects influence the overall sensing performance such as morphology, size, porous structure, and defects, and all are dependent on the synthesis method. The following are common methods used for the fabrication of Co_3O_4-based sensing materials.

2.3.1 Hydrothermal/solvothermal synthesis

Any homogeneous or heterogeneous chemical reaction carried out at high temperatures and pressures inside of sealed containers utilizing water (hydrothermal) or organic solvents (solvothermal), where the reactants can dissolve but the products that are produced are insoluble, is known as a hydrothermal/solvothermal process [29]. The formation of nanomaterials in hydrothermal/solvothermal synthesis can occur at temperatures ranging from room temperature to extremely high temperatures. Depending on the vapor pressure of the main composition in the reaction, either low-pressure or high-pressure conditions can be used to control the morphology of the materials to be prepared. Using this method, different morphologies of Co_3O_4 have been successfully synthesized. By regulating the solvothermal reaction with cobalt acetate, Choi et al. [30] produced a variety of morphologies of cobalt-containing precursors, including nanorods, nanosheets, and nanocubes. These Co_3O_4 nanosheets, nanorods, and nanocubes exhibited respectively 10, 7, and 4.5 times higher response towards 100 ppm C_2H_5OH compared to Co_3O_4 agglomerated nanoparticles operating at 300 °C.

Sun et al. [31] synthesized almost monodisperse Co_3O_4 nanocubes around 20 nm in size using a microwave-assisted solvothermal technique and then examined how well these nanocubes performed as gas sensors for xylene and ethanol. By using facile hydrothermal synthesis, Qiao et al. [32] fabricated 3D Co_3O_4 radial structure nanorods. This morphology was achieved through a subsequent change of hydrothermal reaction time of 4 hours as depicted in **Figure 2.2(a).** Compared to intrinsic Co_3O_4 structures these 3D radial nanorods obtained the highest response of 21.4 towards 20 ppm acetone gas at an optimal temperature of 200 °C, with a response and recovery time of 60/91 s. **Figure 2.2(b)** depicts the solvothermal synthesis of Co_3O_4 hierarchical porous nanosheets prepared by Guo and other researchers [33]. The Co_3O_4 nanosheets sensor exhibited a higher response of 27.6 more than the rest of the sensors towards 50 ppm acetone at 140 °C, with a response/recovery time of 70/64 s. Moreover, Co_3O_4 nanosheets achieved superior selectivity, repeatability, and long-term stability out of all sensors.

From these reports, it can be understood that varying the hydrothermal/solvothermal experimental conditions such as temperature and reaction time can alter the characteristics of the Co_3O_4 nanomaterials. From a gas sensing point of view, changes in material characteristics such as crystallinity and morphology have a paramount influence on gas sensing performance. This will be discussed further when the factors affecting gas sensing performance are discussed later in the review.

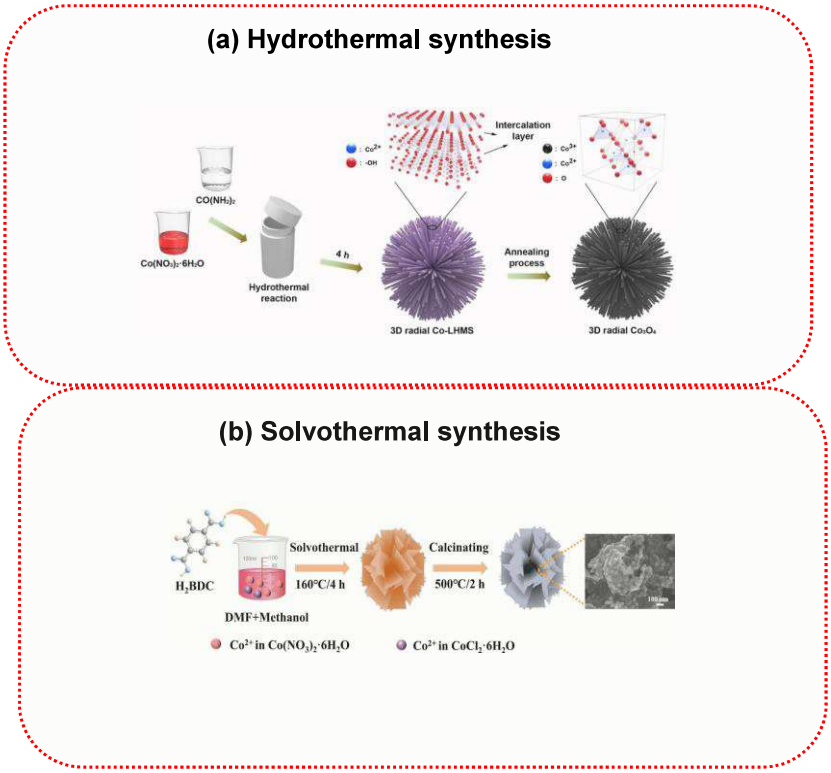

Figure 2. 2: (a) Schematic representation of the hydrothermal method re-used with permission from reference [32] and (b) the schematic representation of the solvothermal method re-used with permission from [33].

2.4 Fabrication of gas sensor films

The resistive gas sensor fabrication involves making a paste using the sensing powder and a solvent ground in a mortar. Owing to their compact size and ease of use, ceramic, silica, and alumina are the types of substrates that are most used in the fabrication of resistive gas sensors. These substrates are integrated with electrodes and heaters for the measurement of the output signal and modulation of heat, respectively. For example, Li et al. [34] fabricated gas sensors based on Co_3O_4, TiO_2, and Co_3O_4@TiO_2. Their sensing properties were measured using an instrument schematically depicted in **Figure 2.6(a)**. 50 mg of sample and deionized water (5 mL) were used to create a paste that was subsequently drop-coated on a 10 mm by 10 mm interdigital electrode. Ultimately, the gas sensor was firmly secured on the 15 mm by 20 mm ceramic heating plate, having the ability to reach a 500 °C heating temperature. Furthermore,

the graphics of Figure 2.6 display the electrodes' dimensions. Therefore, the intended gas sensor is inserted into a quartz tube that is U-shaped and outputs a signal line and a DC heating line. The electrochemical workstation (Shanghai Chenhua Instrument Co., CHI760e, Ltd., China) was used to gather and store the resistance signal. The sampling voltage was set at 0.5 V. The MFC controller completes the target gas at various concentrations (Alite Technology Co., DGD-III, Ltd., China). The gas sensor's response indicates how the sensitive material's resistance changes in the control gas and the target gas, respectively, and the response was calculated as a percentage of the ratio of resistance in gas to resistance in air. On the other hand, Guo et al. [35] created a Sn-Co_3O_4-based sensor on an alumina tube integrated with an Au electrode that was wired with Pt. This was achieved by annealing the alumina tube coated with Sn-Co_3O_4 paste, made of Sn-Co_3O_4 powder and deionized water. The coated alumina tube was subsequently thermally treated for 2 h in air at 300 °C. The operation temperature of the sensor was modulated by a Ni-Cr coil micro-heater that was inserted in the alumina tube. Then the fabricated sensor was fused to the six-foot socket as schematically shown in **Figure 2.6(b)**.

In contrast, Busacca et al. [36] prepared a Co_3O_4-based gas sensor on a 6 mm by 3 mm by 0.5 mm alumina substrate containing Au electrodes and Au heater situated on the opposite side, utilizing the drop coating technique. The film deposited had a thickness of 30 µm with a 3 mm by 3 mm spatial dimensions **Figure 2.6(c)**. Additionally, when the specimen holder is placed within the test chamber made of stainless steel during the electrical analysis process, it can create a hermetic condition. By biasing the Au heater, which serves as both a heater and a temperature sensor, to a maximum of 400 °C, the operational temperature was established. The analysis of the sensor was conducted using an experimental setting shown in **Figure 2.6 (d)**, which permits the performance of measurements in a controlled environment. Using Bronkhorst mass flow controllers, the CO content in the carrier stream was changed to conduct sensing experiments. With increments of 50 °C, tests were made at temperatures between 50 °C and 400 °C in a 100 cm^3 min^{-1} dry air flow stream, gathering resistance measurements in the 4-point method. The chamber's compact size (10 cm^3) and quick setting of the gas level were made possible by the chamber's small capacity. For this, an Agilent 34970A multimeter data acquisition unit fitted onto a 20-channel (2 to 4 wires) multiplexer board Agilent 34901 was utilized, and Agilent E3632A dual-channel power supply equipment was utilized to bias the sensor's integrated heater to conduct measurements at extreme surrounding temperatures. Deng et al. [37] on the other hand, fabricated Co_3O_4 with a paste made like the aforementioned. Nonetheless, their basic component of a gas sensor was a 4 mm ceramic tube with two Au indicator electrodes inside of it. Each electrode had two Pt wires attached to it and was covered by

the prepared paste. The two output electrodes were separated by 1 mm. The dimensions were 1.2 mm for the outer diameter and 0.8 mm for the inner one. A schematic drawing of the sensor as it was manufactured, is shown in **Figure 2.6(e)**, which shows the sensor's construction. The gas sensor acts like a resistor in the circuit, and a heating Ni-Cr wire is positioned in the middle of a ceramic tube to transform current into a source of heat.

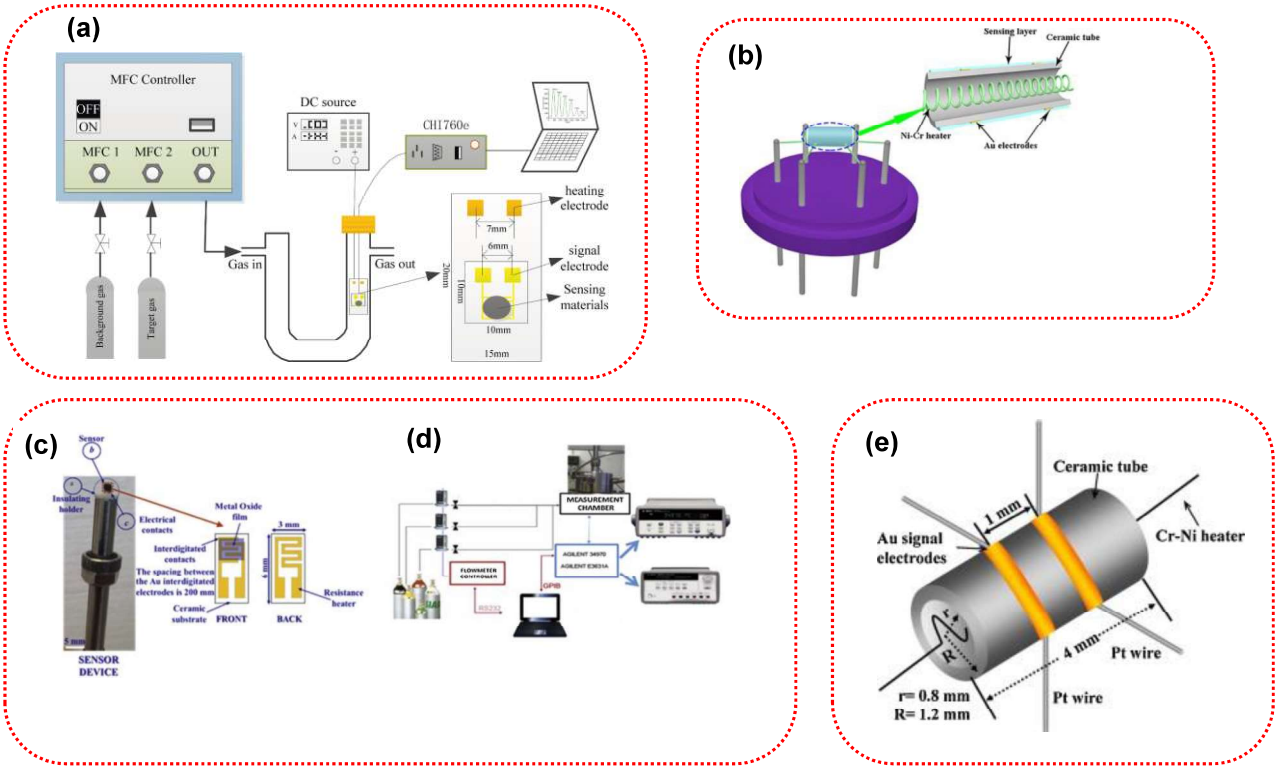

Figure 2. 3: Schematic representation of Co_3O_4 based sensor on (a) ceramic plate with gas detecting apparatus [34], (b) alumina tube [35], (c-d) alumina substrate and gas detecting apparatus [36], and (e) ceramic tube [37].

2.5 Gas sensing parameters and performance of Co_3O_4

The gas sensing performance of Co_3O_4, just like any other SMO-based sensor, is reliant on several features of the sensing material. These features include the morphology, size, operation environment (dry or humid), operation temperature, and others [38,39]. The parameters that are used to measure the gas sensing performance of sensors include:

(i) **Selectivity**- is defined as the sensor's capability to detect a specific gas when it is surrounded by other gases at similar concentration levels. An ideal gas sensor displays high selectivity, showing its ability to primarily detect the target gas while ignoring interfering gases.

Consequently, high selectivity ensures the sensor provides precise and accurate information regarding the presence and concentration of gases [40].

(ii) **Response kinetics (response and recovery time)**- Response time is the duration needed to reach 90% of the ultimate sensor signal, whereas recovery time is defined as the time taken by the sensor to return to 10% of the baseline value after detection [41]

(iii) **Repeatability or stability**- is defined as the sensor's capacity to maintain its characteristics and produce consistent, reliable results when continuously operated over an extended period [42].

(iv) **Limit of detection-** is the capability of a gas sensor to measure the least possible concentration of the analyte gas with reliability under the given conditions [43].

(v) **Operating temperature-** the specific temperature at which a gas sensor exhibits its maximum response to a particular concentration of the analyte gas [44].

(vi) **Response:** When the sensor is exposed to an analyte gas, then the resistance of the sensor is changed. This change in resistance as a function of analyte gas concentration is defined as a response [45]. The estimation of response is defined differently:

$$Response = \frac{|Rg - Ra|}{Ra} \times 100\% \tag{2.1}$$

$$Response = \frac{Ra}{Rg} \tag{2.2}$$

$$Response = \frac{Rg}{Ra} \tag{2.3}$$

where R_a and R_g show the respective sensor resistances in air and analyte gas, respectively.

It is hard for one sensor to be able to fulfill all these parameters, hence the importance of tuning the material for the parameters that are important for the application of interest. **Table 2.1** displays research works on the gas sensing capabilities of Co_3O_4 nanostructures looking at different parameters including operating temperature, selectivity/gas detected best, response, and response kinetics. It can be observed from the displayed data that different nanostructures yield different sensing capabilities. Also, most of the research studies report operating temperatures from as high as 200 °C. High operating temperature is

a huge concern for SMO-based sensors as this results in high energy consumption. A reliable sensor should be energy efficient, hence recent research strives to develop room temperature sensors to address this concern.

Table 2.1: Gas sensing performance of Co_3O_4 nanostructures synthesized with different morphologies.

Morphology	Gas sensing properties			Ref
	Temp. (°C)	Gas, response	$T_{res.}/T_{rec.}$ (s)	
Nanosheets	200	Toluene	1/9	[46]
Nanorods	200	Acetone,194%	3/5	[47]
Nanofibers	301	Ethanol,51.2	22.7/2.4	[48]
Nanofibers	255	Xylene	15/22	[49]
Nanofibers	25	NH_3, 56.20%	7/7	[50]
Nanofibers	200	H_2S, 194%	6/25	[51]
Nanofibers	100	CO,2.4	14/36	[36]
Nanofibers	250	H_2S,2.1	75/258	[52]
Cuboid	320	Ethanol ,10.5	36/40	[53]
Microtubes	160	TEA, 126	5/7	[54]
Microspheres	150	TEA, 34.1	138/86	[55]
Nanorods	225	Acetone, 9.26	38/99	[56]
Nanoparticles	130	TEA, 28.48	113/37	[57]
Thin films	30	CO_2, 13.68	2/12	[58]
Thin films	200	CO, 2%	165/500	[59]
Nanorods	29	NH_3, 14.18	25/8	[60]
Microspheres	210	Xylene, 64.9	203/226	[61]
Nanorods	200	CO, 655	4/6	[62]

2.6 Contributors to gas sensing performance of Co_3O_4 nanostructures

The gas sensing performance of SMO-based sensors relies on the type of sensing material, which takes into consideration the morphology, size, structure, defects, surface area, and porosity characteristics. In

the air, the SMO-based gas sensor adsorbs oxygen gas from the surroundings leading to charge transfer between oxygen and the surface of SMO. The oxygen gas thus ionizes into O_2^-, O^- or O^{2-} corresponding to operation temperatures less than 150 °C, between 150 °C and 400 °C, and more than 400 °C according to equation (2.4) to (2.7). As a result, a layer of ionized oxygen gas forms on the surface of the SMO subsequently making the surface active**.** Because the processes taking place on the SMO surface have an impact on the gas adsorption and desorption on its surface, the temperature of operation of gas sensors based on SMOs is crucial [63-65]:

$$O_2(gas) \rightarrow O_2(ads) \quad (2.4)$$

$$O_2(ads) + e^- \rightarrow O_2^-(ads) \quad (2.5)$$

$$O_2^-(ads) + e^- \rightarrow 2O^-(ads) \quad (2.6)$$

$$2O^-(ads) + e^- \rightarrow O^{2-}(ads) \quad (2.7)$$

In this section we will look at the gas sensing performance of Co_3O_4 nanostructures and their modified counterparts with emphasis on the reasons behind the reported gas sensing performance. The influence of morphology and size and the forming of composites through doping, surface functionalization, and coupling with other materials will be investigated in detail.

2.6.1 Size and morphology control

The assembly and morphologies of Co_3O_4 nanostructures have a significant influence on their gas-sensing performance. Different research studies about morphological control, inclusive of effects induced by crystal size, shape, orientation, porosity, surface area, and even defects have been reported [33,66-71]. The development of solution-based chemical control synthesis of micro-/nanostructured materials has expanded over the past few decades from monodispersed particles to nanowires, nanotubes, nanorods, cables, and polygons [72-74]. Particularly, by adjusting the accessibility of functional components, the curvature of interfaces, and the arrangement of the internal organizations, hierarchical micro-/nanostructure design and synthesis enable the customization of material properties. Che et al. [75] successfully synthesized hierarchical Co_3O_4 flower-like microspheres using the solvothermal method. The key step of this method was to construct flower-like microstructures of the cobalt-containing precursors by manipulating the synthetic parameters in a facile ethylene glycol-mediated solvothermal reaction. The produced Co_3O_4 flower-like microspheres showed a good reaction and sensitivity to ethanol gas when tested as a gas sensor, indicating their intriguing potential for use as gas sensors. This was

attributed to open flower-like nanostructures made of nanosheets which are suggested to be favorable for fast diffusion of gas molecules, resulting in the high rates of gas adsorption and desorption. Also, the thickness of Co_3O_4 nanosheets was 5 nm which resulted in a larger surface area, providing more active sites that increased the electron transfer associated with the chemical reaction between the active sites and ethanol.

Alheshibri et al. [76]synthesized Co_3O_4 nanostructures with different morphologies using pulsed laser ablation in liquid media (PLAL) using high-purity cobalt targets in several ethanol/water mixtures. The morphology was controlled through variation of the ethanol as 0, 10, 20, and 70%. The obtained morphologies ranged from spherical spheres to nanoparticles to sheets. The gas sensing performance revealed good sensing characteristics to 200 ppm CO at 300 °C by the nanosheet structures. The good sensing performance was attributed to the thin sheet morphology and high surface area. Patil et al. [62] synthesized Co_3O_4 nanorods with a diameter of ~ 6–8 nm, and length of ~20–30 nm using a simple co-precipitation/digestion method by calcinating cobalt hydroxyl carbonate in air. These nanorods obtained a good response of 6.55 towards 50 ppm CO at 250 °C with a response/recovery time of approximately 3-4/5-6 s, compared to a response of 2.20 exhibited by commercial Co_3O_4 powder with the morphology of nanoparticles. This observation was attributed to smaller size and higher specific surface area of the nanorods which played a vital role in increasing the gas sensor response, overall enhancing the gas sensing performance towards CO gas. The nanorods also responded to a low concentration of 5 ppm CO at 250 °C, which suggested that they can be reliably used to monitor the concentration of CO gas over the 5-50 ppm range. On the other hand, Guo et al. [33] prepared Co_3O_4-x (x= 0, 1, 2,3) hierarchical porous nanosheets through solvothermal synthesis, by simply varying proportions of cobalt nitrate and cobalt chloride to observe the effects they have on morphology of the structures. The morphology changed from loose and porous nanosheets to smooth and uniform nanosheets. The Co_3O_4-2 sensor exhibited a higher response of 27.6 than the rest of the sensors towards 50 ppm acetone at 140 °C, with a response/recovery time of 70/64 s. Furthermore, the Co_3O_4-2 sensor also displayed superior selectivity, repeatability, and long-term stability out of all sensors. This was credited to the porous nature of the structures prepared with the N/C ratio of 4:2 which increased the electron transport channels, therefore improving gas sensitivity. Lin and other researchers [68] synthesized three different kinds of morphologies namely nanosheets, nanorods, and nanofibers through the hydrothermal and electrospinning methods. The obtained nanosheets achieved the highest response value of 6.1 towards 100 ppm acetone at 160 °C compared to nanorods and nanofibers which had responses of 2.7 and 4.0, respectively. This observation

was attributed to the small size of the nanosheets with an average thickness of 20 nm, edge length of 120 nm, and highly exposed (111) planes, which might have unique surface reactivity or binding sites that enhanced their sensitivity towards acetone molecules. These exposed planes could provide active sites for the adsorption and reaction of acetone molecules, leading to a higher sensitivity even with a small specific surface area.

Based on these works, morphology is a viable strategy to manipulate or optimize the gas sensing performance to suit the specific gas sensing application desired. Control of morphology brings about changes or tuning of other SMO characteristics such as size, exposed facets, surface area, and porosity as well as defects. When it comes to size, which can be either the crystallite/grain or particle size, it has been shown that reduction of the size has positive effects on the gas sensing performance as the smaller the size, the higher the surface area, thus providing more active sites for gas adsorption. By monitoring and controlling the morphology and size of the Co_3O_4 nanostructures, it is possible to optimize the gas sensing performance towards the analyte gas of interest, for instance, Choi et al [30] prepared various morphologies such as nanorods, nanosheets, and nanocubes shown in **Figure 2.7** through the hydrothermal method, to obtain these morphologies, the hydrothermal reaction was controlled using cobalt acetate, L (+)-lysine, and oxalic acid. To test the gas sensitivity of each morphology-based gas sensor, they were exposed to 100 ppm of C_2H_5OH at an operating temperature of 300 °C. The sensors exhibited gas responses of 57.7, 25.7, 24.7, and 5.5 for nanosheets, nanorods, nanocubes, and pure agglomerated Co_3O_4 nanoparticles respectively, it was observed that the responses of nanosheets, nanorods, and nanocubes were 10.5, 4.7, and 4.5 times higher than that of the agglomerated Co_3O_4 nanopowders, thus an enhanced gas sensitivity was attributed to less agglomerated structures obtained. On the other hand, Wang et al. [77] synthesised nanostructures with various morphologies and different sizes, including rhombic dodecahedrons (1 μm), flower-like assembly (1 μm), and octadecahedrons (200 nm and submicron) shown in **Figure 2.8** through alteration of Co^{2+} ions and 2-methylimidazole. The gas sensing performance was tested towards 100 ppm of n-butanol at operating temperatures of 100, 115, and 140 °C. The four sensors fabricated, Co_3O_4-1(dodecahedrons), Co_3O_4-2(flower-like), Co_3O_4-3(octadecahedrons sized1 μm), and Co_3O_4-4 (octadecahedrons size submicron) showed good responses of 4.8, 12.8, 13.1 and 21.0, respectively with a response and recovery time of 127/15 s, 146/30 s, 148/19 s and 146/90 s. The Co_3O_4-4 based gas sensor exhibited high responses compared to other sensors. This observation was influenced by the shape and the size of Co_3O_4 assemblies. Following, the surface area effects and defects properties are discussed.

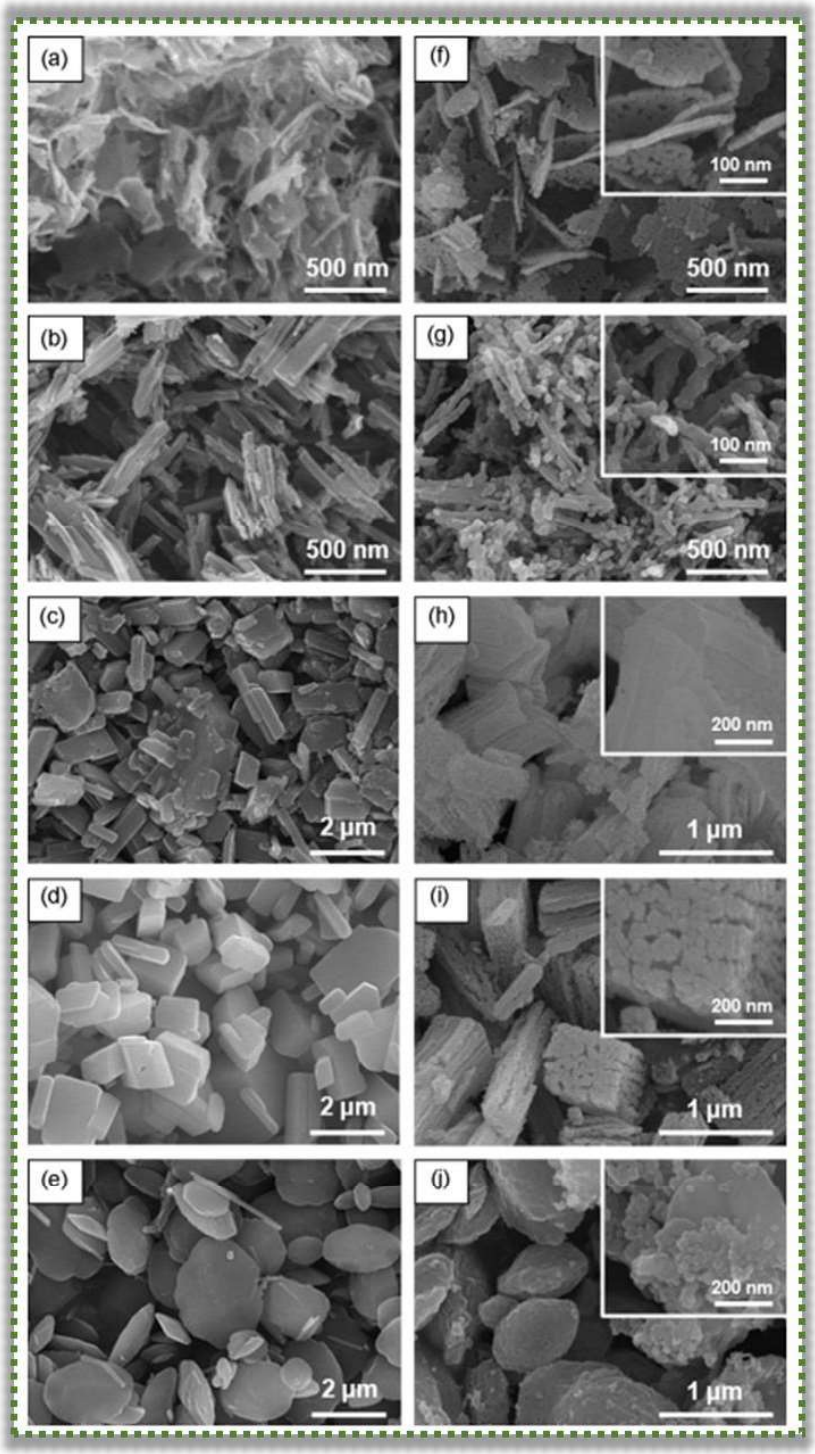

Figure 2. 4: SEM images of the as-prepared cobalt precursors and the Co_3O_4 nanostructures, the latter resulting from the heat treatment (HT) of the former at 400 ◦C for 1 h: (a) CL-18 precursors, (b) CO-1 precursors, (c) CO-18 precursors, (d) CLO-18 precursors, (e) CHO precursors, (f) Co_3O_4 nanosheets prepared by HT of CL-18 precursors, (g) Co_3O_4 nanorods prepared by HT of CO-1 precursors, (h) Co_3O_4 nanocubes prepared by HT of CO-18 precursors, (i) Co_3O_4 nanocubes prepared by HT of CLO-18 precursors, and (j) Co_3O_4 powders prepared by HT of CHO precursors [30].

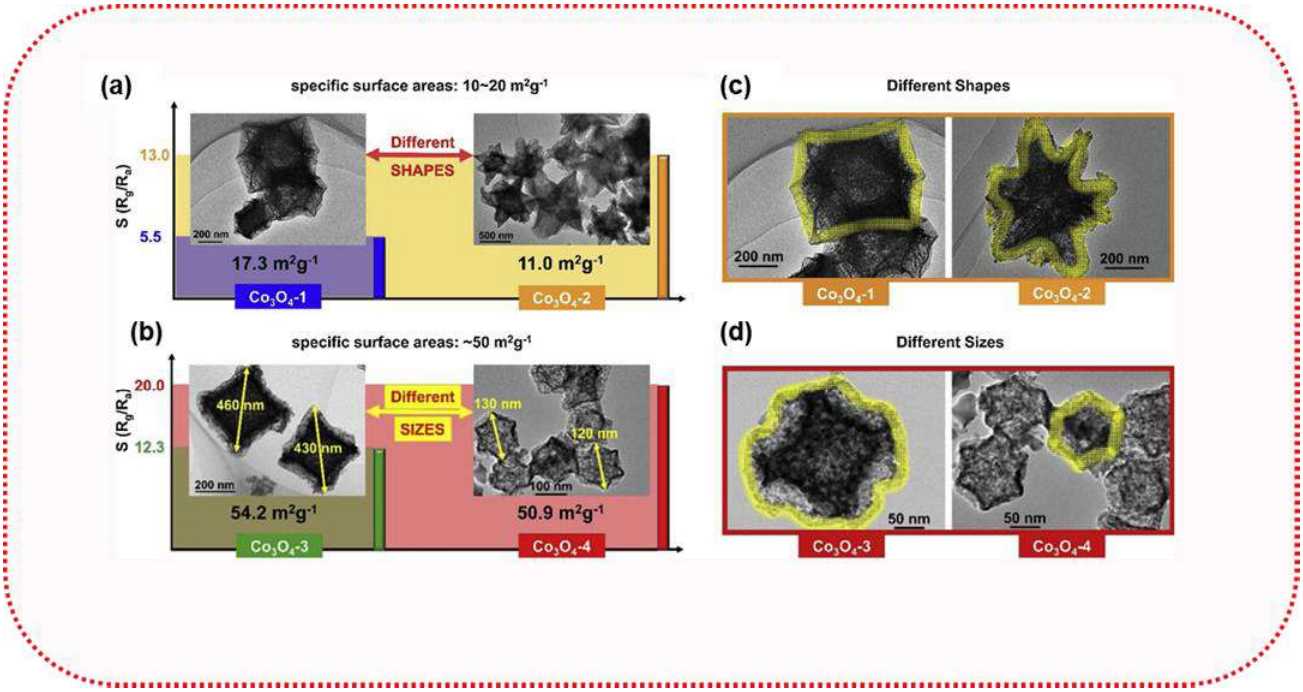

Figure 2. 5: Comparison of responses to 100 ppm n-butanol, specific surface areas, and morphology observed from TEM images of (a) Co_3O_4-1 and Co_3O_4-2; (b) Co_3O_4-3 and Co_3O_4-4. Comparison of internal nanoparticles (which are outlined in yellow) of (c) Co_3O_4-1 and Co_3O_4-2; (d) Co_3O_4-3 and Co_3O_4-4 [77].

2.6.2 Surface area and porosity effects

It is known that the surface area and porous structure play an important role in the sensing performance of SMO. Specifically, porous SMO architectures having high surface area, and large pore volume can ensure them as effective sensor materials for high-performance gas sensors. This is because a high surface area provides a larger reaction contact area between the sensing material and the target gas by increasing active sites for gas adsorption which can improve the sensitivity of the sensing material [39,78]. Furthermore, the sensitivity of SMO materials can significantly be affected by the porosity of the sensing material as porosity increases diffusion and more active sites [79].

In their study, Hu et al. [80] successfully fabricated Bubble-like Co_3O_4 tubes using a ZIF-67 intermediate-assisted thermal decomposition strategy. Furthermore, they carried out a systematic comparison of the gas-sensing properties between Rod-like Co_3O_4 and Bubble-like Co_3O_4. Their findings revealed that the inclusion of the ZIF-67 intermediate had a positive impact on the gas-sensing performance of Bubble-like Co_3O_4. Specifically, the sensor made with Bubble-like Co_3O_4 exhibited a response value around ten times higher than that of the Rod-like Co_3O_4 sensor when detecting 100 ppm triethylamine (TEA) at 180 °C shown in **Figure 2.9(a-b)**, with a low detection limit of 55 ppb. Additionally, the gas sensor displayed

exceptional selectivity displayed in **Figure 2.9(c)** and stability against humidity, with minimal response variation even after 30 days shown in **Figure 2.9(d))**, retaining approximately 98% of its initial value. This impressive sensing performance can be attributed to factors such as the large specific surface area as the Brunauer-Emmett-Teller specific surface area of Rod-like Co_3O_4 and Bubble-like Co_3O_4 was determined to be 25.4 m^2g^{-1} and 58.9 m^2g^{-1}, respectively, depicted in **Figure 2.9(e-f)**. Additionally, their average pore sizes were measured at 6.8 nm and 8.5 nm, respectively. These results highlighted that Bubble-like Co_3O_4 possessed a significantly larger specific surface area and higher pore volume compared to Rod-like Co_3O_4. This difference provided an abundance of active sites and efficient electron transfer channels during gas sensing reactions, ultimately contributing to the marked improvement in sensing performance. The sensing performance was also attributed to the abundant oxygen vacancies, and efficient Co^{3+}/Co^{2+} catalyzing on top of the high surface area.

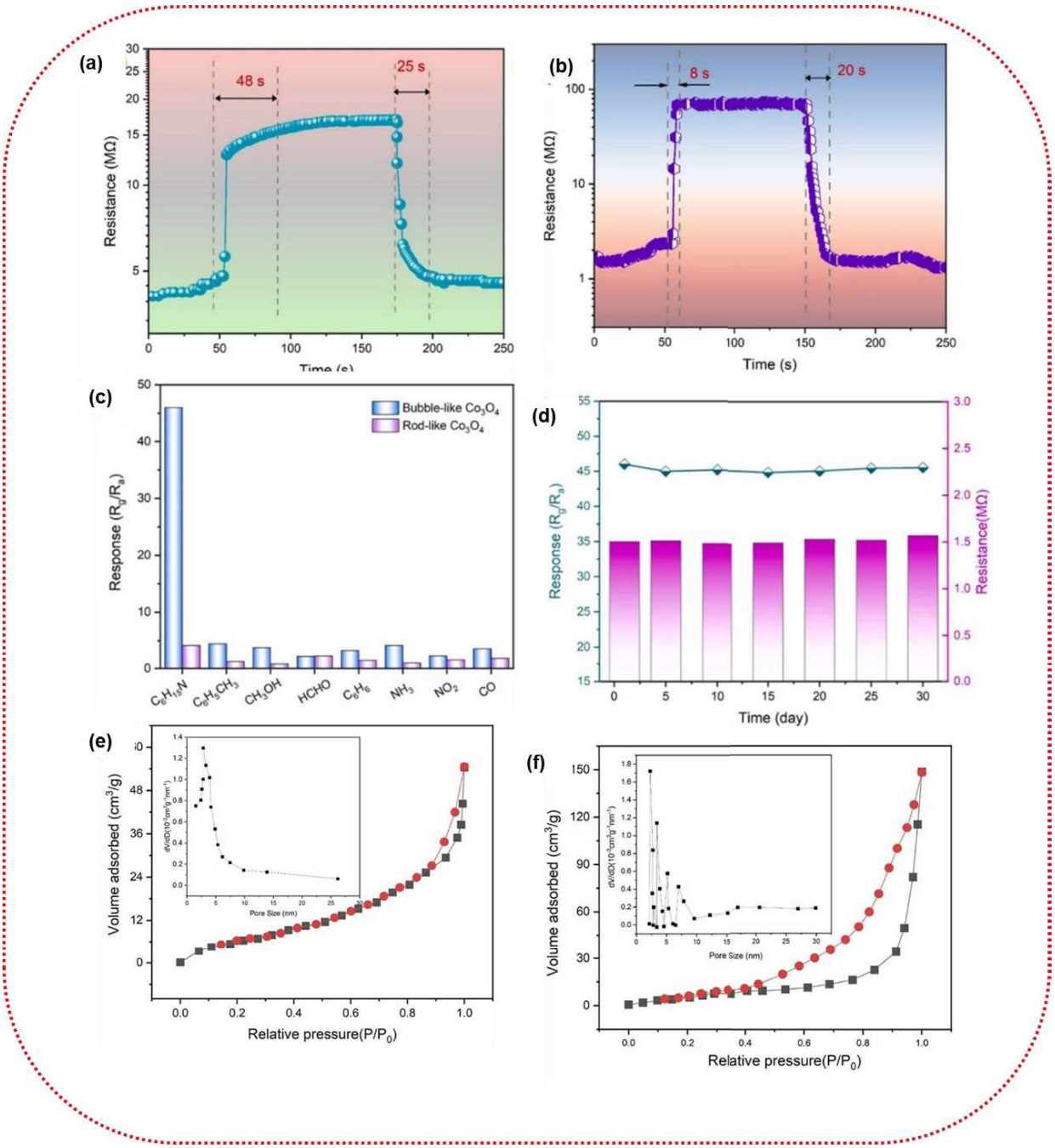

Figure 2. 6: (a-b) Response characteristics (b) selectivity, (c) stability and (e-f) N_2 isotherms of the Rod-like Co_3O_4 and Bubble-like Co_3O_4 used with permission from reference [80].

Lu et al. [81] manufactured porous Co_3O_4 nanocubes through solid chemical transformation methods at different temperatures, 300, 350, and 400 °C. Through this method, the porous nature of these structures was influenced by calcining the Co-MOF precursors at 300 °C. As a result, the Co_3O_4-300 sensor exhibited the maximum response towards 200 ppm ethanol at 300 °C with a response/recovery time of less than 10 s. Furthermore, when compared to Co_3O_4-350 and Co_3O_4-400 sensors; it possessed high

sensitivity, stability, and good reproducibility. This observation was attributed to the porosity of the structure and a large specific surface area of 120.9 $m^2 \cdot g^{-1}$, which resulted in more active sites on the surface available for chemical or physical interactions. The increased number of active sites allowed for a higher probability of interactions between the sensing material and the ethanol gas, which in turn leads to better sensing performance. Xu et al. [82] reported on controlling the shape of Co_3O_4 nanostructures from Co_3O_4 nanorods, nanosheets, platelets, and hexagonal $Co(OH)_2$ synthesized through precipitation technique followed by calcination at 200 °C and 300 °C. The nanosheets sensor reached a maximum response of 22.6 towards 1000 ppm ethanol at 240 °C with a response/recovery time of 145/128 s, compared to acetone (1.35), in contrast to the rest of the sensors, on the other hand, cobalt hexagonal sensor exhibited maximum response towards acetone than the rest of the sensors. The observed nanosheet-based gas sensor performance was due to the large surface area of 131.52 m^2g^{-1}, which provided more sufficient opportunity to react with ethanol molecules under a high gas concentration, resulting in a higher response value. The cobalt hexagonal sensor responded better towards 100 ppm acetone at 250 °C because of the structure's largest macropore volume caused by calcination at 300 °C.

Wang et al. [83] synthesized dispersed and bundled Co_3O_4 nanowires using the nanocasting synthesis method and used ordered mesoporous SBA-15 silica as hard templates. The gas response of Co_3O_4-DNWs sensors in 100 ppm toluene gas at 210 °C was found to be 11.761, which was much higher than the response of 8.437 for Co_3O_4-BNWs. The observed difference in sensing performance was attributed to the large surface area of 44.98 m^2g^{-1} for Co_3O_4-DNWs as compared to 42.59 m^2g^{-1} for Co_3O_4-BNWs. Further, Wang et al. [84] explored the porous Co_3O_4 cubes obtained by the calcination of Prussian blue analogue (PBA) cubes. Comparing PBA Co_3O_4 smashed cubes and as-prepared porous Co_3O_4 towards the exposure to 100 ppm n-butanol at an optimal temperature of 100 °C, the as-prepared porous Co_3O_4 sensor responded up to a maximum value of 80.8 with a response/recovery time of 318/31 s and the smashed Co_3O_4 from PBA cubes responded up to a maximum value of 16.9. This observation was attributed to the large surface area of the initial Co_3O_4 of 42.6 m^2g^{-1} and its bigger pores (>20 nm) that accumulated from cubic assemblies, compared to the one of smashed Co_3O_4 of 39.4 m^2g^{-1} Bigger pores made it easier for n-butanol to diffuse among cubes and then deep inside the sensing layer coated on the sensor. Other works acknowledging the effect of porosity and high surface area can be obtained elsewhere [85-87].

2.6.3 Defects engineering effects

Surface electronic regulation proves to be a highly effective technique for manipulating the electron-trapping capabilities, reducing reaction barriers, and optimizing the kinetics of surface adsorption and desorption. These factors are pivotal in enhancing the overall performance of sensing materials. The precise control of oxygen vacancies serves to facilitate gas adsorption behavior on the surface and modulate the charge structures of sensitive materials, thereby contributing significantly to the outstanding performance exhibited by the sensors [88]. Consequently, the strategic tuning of surface electron states to induce defects and govern the micromorphology of the sensing materials holds substantial promise for accelerating gas mass transfer rates, ultimately leading to a remarkable enhancement in gas sensor performance. For example, Shi et al. [89]employed $Co_2(OH)_2CO_3$ to synthesize Co_3O_4 nanosheets through a hydrothermal process following controlled calcination. They demonstrated that by precisely controlling the annealing temperature, the defect concentration within the Co_3O_4 nanosheets could be fine-tuned, consequently influencing the gas sensing performance. The gas sensing studies showed that the sensors based on the porous Ov-Co_3O_4 nanosheets exhibited excellent gas sensing performance with superb selectivity and rapid response at low temperatures, toward TEA. They attributed the excellent gas sensing performance to the presence of abundant oxygen vacancies, combined with a large specific surface area of the Co_3O_4 nanosheets.

In another study, Liu et al. [90] synthesized flower-like (Co_3O_4-f) composed of thin nanosheets and Co_3O_4-p (nanoparticles) through the solvothermal and subsequent calcination. Their study further compared the gas sensing performance illustrated in **Figure 2.10(a-f)** of Co_3O_4-f and Co_3O_4-p, revealing that Co_3O_4-f outperformed due to several key factors. Firstly, the morphology of Co_3O_4-f, composed of thin nanosheets with exposed (111) crystal planes, enhanced catalytic activity and facilitated gas adsorption. The nanosheets also served as efficient carriers for rapid diffusion throughout the material. Co_3O_4-f's large specific surface area, confirmed by BET characterization, provided sufficient adsorption sites. In contrast, the irregular crystal grains and smooth surface of Co_3O_4-p hindered gas sensitivity. Secondly, XPS analysis in **Figure 2.10(g-k)** demonstrates that Co_3O_4-f exhibited more chemisorbed oxygen displayed in **Figure 2.10 (j)**, correlating with increased gas sensitivity. Lastly, both XPS in **Figure 2.10 (j)** and EPR in **Figure 2.10 (l)** indicated higher oxygen vacancies in Co_3O_4-f. The assembly of the nanosheets created numerous lattice oxygen defects, serving as active centers for improved gas sensing. The resulting increase in donor density enhanced Co^{2+} concentration, promoting additional adsorbed oxygen and further elevating gas sensitivity.

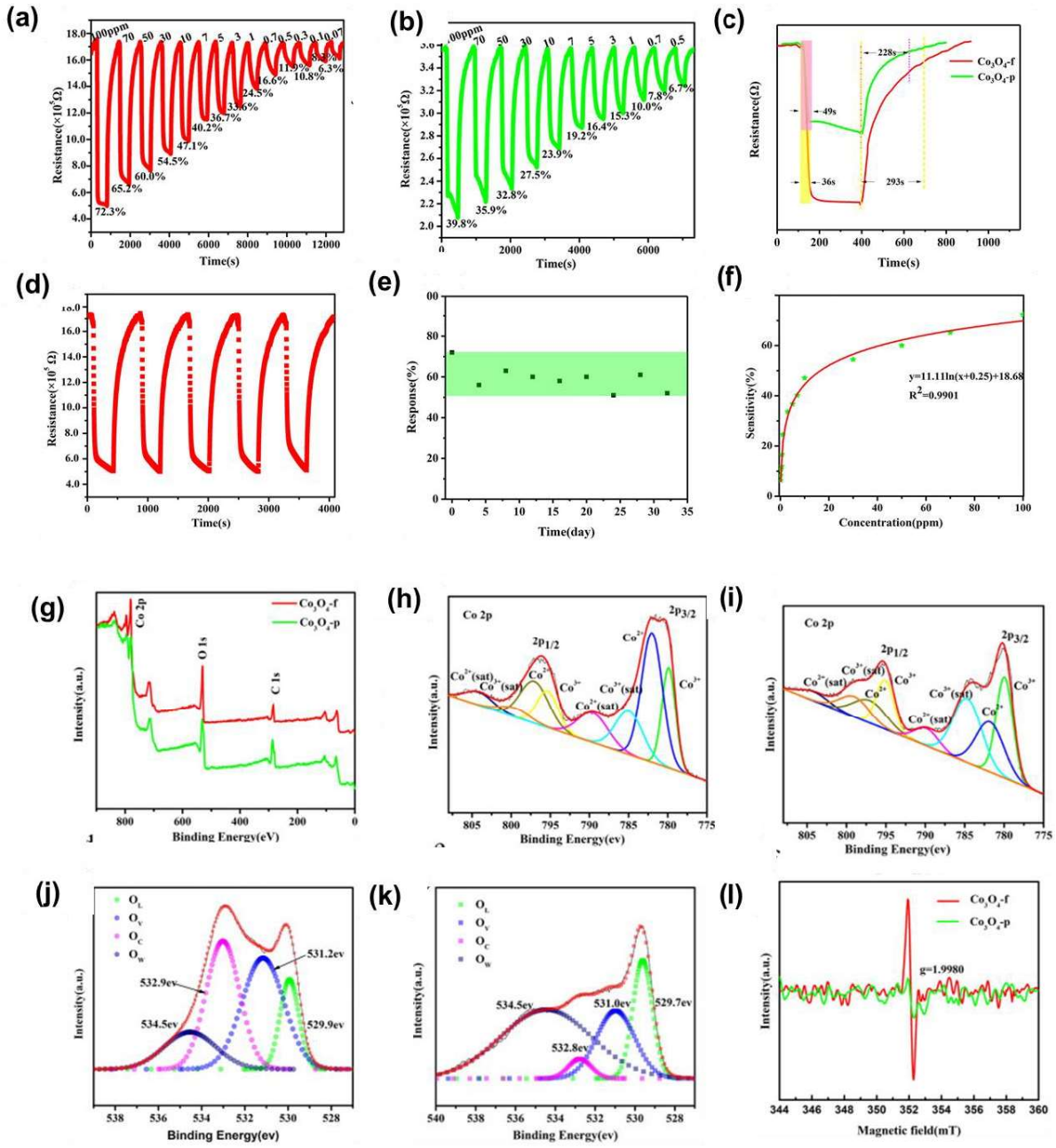

Figure 2. 7: The dynamic response curves of (a) Co_3O_4-f at room temperature and (b) Co_3O_4-p; (c) response and recovery times based on the transient resistance curve of the Co_3O_4-f sensor and Co_3O_4-p, (d) reproducibility of Co_3O_4-f sensor exposed to 100 ppm NO_X for five-cycle testing at room temperature; (e) Long-term stability to 100 ppm NO_X of Co_3O_4-f and (f) Concentration-response relationship of Co_3O_4-f sensor; **(g)** XPS survey spectra of, Co 2p spectra of (h) Co_3O_4-p, (i) Co_3O_4-f, O 1s spectra of (j) Co_3O_4-f and (k) Co_3O_4-p; and the (l) EPR spectra of Co_3O_4-f and Reused with permission from [90].

Cheng et al. [91] fabricated a metal-organic framework (MOF) derived Co_3O_4 nanospheres using hydrothermal synthesis with subsequent calcination from 300-500 °C, to test gas response sensors were tested towards 100 ppm of n-butanol at 140°C, Co_3O_4 nanosphere based gas sensor calcined 400 °C showed an excellent response of 53.78, with response and recovery time of 153/53 s. This observation was ascribed to the calcining treatment that created a lot of oxygen vacancies that resulted in increased active sites improving the gas adsorption thus increasing the overall gas sensing. Hu et al. [80] reported the successful fabrication of bubble-like Co_3O_4 tubes derived for ZIF67 through a thermal decomposition technique for trimethylamine (TEA) gas sensing performance. Bubble-like Co_3O_4 -based gas sensors were compared with rod-like Co_3O_4 gas sensors, and bubble-like Co_3O_4 gas sensors obtained a maximum response of 3.8 towards 100 ppm of TEA at 180 °C with a response and recovery time of 48/25 s. for stability measurement the sensor was further test for 30 days, and it was found that the response values did not decrease significantly which displays good stability. this was attributed to the presence of generous amounts of functional groups containing oxygen on the surface of the material that leads to more active sites for increased gas adsorption, characterized by C-C, C-O, and C=O from the XPS, as the porous nature of the material derived from ZIF-67 played a role as it provided the material with abundant oxygen vacancies.

2.7 Co_3O_4-based nanocomposites

Despite its high surface reactivity, the p-type gas sensor based on Co_3O_4 nanoparticles frequently suffers from a low response to gas molecules due to high-temperature sintering and inefficient resistance modulation. This means that at elevated temperatures, p-type Co_3O_4 has many hole carriers to participate in electrical conduction. However, the higher the carrier concentration, the more difficult it is to change through gas-surface interactions, thus resulting in a low sensitivity [92]. As a result, the design of composites through the addition of a second constituent has been demonstrated as an effective way of improving the gas sensing performance of Co_3O_4-based sensors in comparison to the corresponding pure structures because of synergistic interactions between the different composite constituents [93].

Electronic effects such as band bending due to Fermi level equilibration, charge carrier separation, manipulation of the depletion layer, and increased interfacial potential barrier energy; chemical effects such as decreased activation energy, targeted catalytic activity, and synergistic surface reactions; and geometrical effects [94-103] have all been implicated in the improved sensing performance of these

composites. Understanding the mechanisms that govern sensing behavior in these composites is thus critical for future advances in the gas sensor technology space.

This section investigates some of the Co_3O_4-based composites with a focus on doping, formation of p-n heterojunctions, and loading with noble metals. The effects brought upon by these modifications will be investigated in detail.

2.7.1 Doping

The incorporation of a second component as a dopant is emerging as one of the more intriguing techniques for the optimization of gas-sensing capabilities, in addition to the preparation of diverse Co_3O_4 morphologies and Co_3O_4-based composites.

According to Barreca et al. [104], adding F as a dopant to Co_3O_4 can lead to improved reversibility, higher responses, and lower operating temperatures when compared to Co_3O_4 alone. On the other hand, due to the catalytic activity and a large amount of oxygen absorbed by the Cr oxides, Cr-doping could considerably improve the reactivity of Co_3O_4 to methyl benzenes while inhibiting cross-reactions to interfering gases [105].

Zhang et al. [106] prepared hierarchical Co_3O_4 nanostructures doped with Fe through solvothermal synthesis. Gas sensing performance was tested on pure and doped Co_3O_4 gas sensors at a working temperature of 175 °C toward 100 ppm of Xylene. Amongst the six gas sensors including the pure one, the 6 at% Fe-Co_3O_4 gas sensor exhibited an optimum response of 18.7 with a response and recovery time of 40/35 s. This behavior was ascribed to Fe doping, by substituting Fe^+ for Co^+ which helped with the enhancement of active sites for the generation of more oxygen vacancies on the surface that acted as centers for oxygen adsorption thus increasing the sensitivity of low doped Co_3O_4 gas sensor to xylene. Liu et al. [61] incorporated Co_3O_4 hierarchical microspheres with different Ti doping using the co-precipitation method and sintering at a temperature of 450 °C. Pure and Ti-doped Co_3O_4 sensing performance was tested towards 50 ppm of xylene and toluene at different temperatures shown in **Figure 2.11 (a-d).** Towards 50 ppm xylene, the sensors displayed their optimal operating temperature at 210 °C, with the 3 at.% Ti-doped Co_3O_4 microspheres-based gas sensor obtained the highest response of 64.9 than the rest of the sensors. The sensor's performance towards 50 ppm of toluene revealed optimal operating temperature at 240 °C, with the 1 at.% Ti-doped Co_3O_4 microspheres-based gas sensor exhibiting the highest response of 57.2. These responses were attributed to Ti doping, With the mechanism shown in **Figure 2.11 (g-j)**.

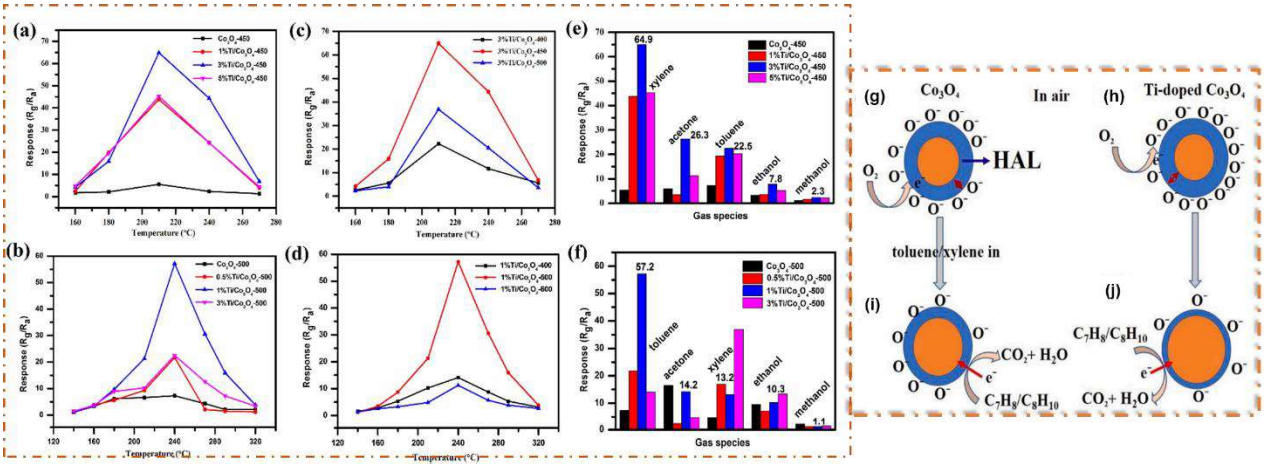

Figure 2. 8: Responses of (a) Ti-doped Co_3O_4-450 to 50 ppm of xylene and (b) Ti-doped Co_3O_4-500 to 50 ppm of toluene at different working temperatures; Responses of (c) 3 %Ti/Co_3O_4 and (d) 1 %Ti/Co_3O_4 obtained at different calcination temperatures to 50 ppm of xylene and toluene, respectively; Responses of (e) Ti-doped Co_3O_4-450 to 50 ppm of various gases at 210 °C and (f) Ti-doped Co_3O_4-500 to 50 ppm of various gases at 240 °C. and the schematic diagram of the sensing mechanism of Co_3O_4 and Ti-doped Co_3O_4 in (g-h) air and (i-j) toluene and xylene [61].

Ru-doped Co_3O_4 flower-like hollow microspheres were successfully synthesized by Jin et al. [107] through the hydrothermal method. The sensitivity of the Ru-doped Co_3O_4 microspheres based gas sensors was investigated by exposing them to 10 ppm of acetone, the 1 at% Ru-doped Co_3O_4 sensor exhibited a good response of 18.8 which was approximately 5.4 times bigger than the response of the pristine Co_3O_4 sensor at an optimal working temperature of 137.5 °C The reason for this observation is because Ru doping changed the charge carrier concentration and oxygen components which improved the response of Ru-doped Co_3O_4 gas sensors.

Mehrabadi et al. [108] prepared Cu-doped Co_3O_4 cubic nanocrystals using sol-gel synthesis method. The prepared Cu–Co oxide nanoparticles had different mole ratios of Cu/Co from 0 to 0.15 namely S1-S6 respectively. All six sensors were exposed to 3000 ppm, 4500 ppm, and 6000 ppm methane gas at 300 °C. In all the concentrations S6 sensor achieved maximum sensitivity compared to the other sensors, with a maximum sensitivity value obtained at 6000 ppm. This was due to doping Co_3O_4 with Cu, which considerably improved the sensitivity by influencing the defect chemistry and decreasing the particle size, thus increasing the sensitivity in general. Jincy et al. [109] also reported on the hydrothermal synthesis of Cu-doped Co_3O_4 round-shaped nanoparticles. The doped and pure Co_3O_4 nanoparticles were tested against 1-5 ppm of NH_3 at room temperature. Cu-doped Co_3O_4 nanoparticles exhibited high sensitivity at 5 ppm for NH_3 gas compared to pure Co_3O_4 nanoparticles, this observation was attributed

to the doping effect of Cu. The impact of the Cu content on the surface oxidoreduction action was connected to their microstructure, composition, and crystalline state. These properties influenced the material's ability to adsorb and react with NH_3 molecules, leading to the observed increase in sensitivity.

Yang et al. [110] incorporated pure and Mo-doped flower-like stacked Co_3O_4 nanosheets through a facile wet-chemical method followed by annealing treatment at 400 °C. The nanosheets became more stacked with increasing concentrations of molybdenum (Mo) dopant (o% Mo/Co_3O_4, 0.25% Mo/Co_3O_4, 0.5% Mo/Co_3O_4 and 1% Mo/Co_3O_4). The gas sensing capacity of pure and Mo-doped Co_3O_4 samples was studied by exposing all four sensors to 100 ppm toluene vapor at a working temperature range of 90-210 °C, 0.5% Mo/Co_3O_4 sensor displayed a maximum response of 44.56 towards 100 ppm toluene at 150 °C which was the highest response accumulated compared to the rest of the sensors. Furthermore, it responded to a low concentration of 1 ppm of toluene as the lowest detection limit which could be advantageous for Occupational Safety and Health. The reason behind this response was due to the formation of more Co^{3+} ions in Co_3O_4 through Mo-doping. When Mo^{6+} ions were incorporated into the Co_3O_4 lattice, the Co^{2+}/Co^{3+} were replaced with Mo^{6+}. This replacement led to a release of electrons through this conversion ($Co^{2+} \rightarrow Co^{3+} + e^-$) according to the electronic compensation mechanism. This conversion promoted the Co^{3+} content in the 0.5% Mo-doped Co_3O_4 sensor. As well known, Co^{3+} could act as an active site for catalytic oxidation of toluene in the sensing process, therefore the increase of Co^{3+} resulted in an improved sensor response. On the other hand, Sun et al. [111] synthesized 2-D spindle-like pure and Sn-doped Co_3O_4 porous nanosheets using a solvothermal technique and subsequent thermal treatment at 500 °C.

The Sn-doping molar ratios were 0%, 3%, 5%, and 7%. All four sensors were introduced to 100 ppm TEA, the 5% Sn-doped Co_3O_4 sensor exhibited an excellent response of 70.7 towards TEA at a working temperature of 180 °C with a fast response/recovery time of 1/17 s and good repeatability compared to the pure Co_3O_4 sensor and other doped sensors. This observation was attributed to Sn doping, Sn^{4+} was incorporated into the Co_3O_4 lattice and replaced the Co site in the Co_3O_4 crystal to produce more electrons and introduced lattice defects which led to the enhancement of gas responses.

Furthermore, Cheng et al. [112] worked on the synthesis of pure and Ni-doped Co_3O_4 hierarchical microflowers using a facile one-step co-precipitation technique. Four samples were carried out based on Ni-doped Co_3O_4 (Ni content: 1.03–9.04 mol. %) and the ratio of ethanol/water was also observed. 5.3 mol. % Ni-doped Co_3O_4 microflower sensor (R-E/W =3/30) displayed a maximum response of 8.34 towards 100 ppm n-butanol at 165 °C with a response/recovery time of 59/63 s, excellent anti-humidity

performance and long-term stability in contrast to other sensors. This behavior was caused by doping of Ni^{2+} into Co_3O_4 which was conducive to the enhancement of sensing performance, the Ni^{2+} sites acted as catalytic sites promoting the occurrence of oxidation reaction. Fareed and other researchers [113] reported on co-precipitation synthesis of Gd-doped Co_3O_4 nanoplates followed by calcination at 600 °C. Four samples were prepared pure, 3%, 6%, and 9% Gd-doped, all the sensors were tested on different concentrations of oxygen (1%,2%,3%, and 4%) at 240 °C. 6% Gd doped Co_3O_4 sensor displayed a high response of 921% towards 4% of oxygen with a response and recovery time of 23/22 s compared to the rest of the sensors. This was attributed to the decrease in particle size and an increase in oxygen adsorption with Gd doping due to created oxygen vacancies. These vacancies acted as active sites for oxygen.

Guo et al. [35] synthesized Sn-doped Co_3O_4 yolk-shell nanostructures derived from a metal-organic framework through the hydrothermal method, Sn doping concentration ranged from 1-5 mol%. Gas sensing sensitivity was measured for Co_3O_4 yolk-shell nanostructures-based gas sensors towards 100 ppm of ethanol at a working temperature of 200 °C, and the gas sensor with 3mol% of Sn displayed a good response of 13.4 with excellent response and recovery time of 18/22 s amongst the four kinds of gas sensors. Not only did it show a good response but also good stability as it was tested for an extra 20 days, and the response decreased to 11.2. This observation was accredited to the suitable amount of Sn doping which tempered with the Ov content of Co_3O_4 yolk-shell nanostructures, increasing Ov contents created more active sites resulting in increased gas reaction and adsorption. Chen and colleagues [114] synthesized 2D Cd-doped Co_3O_4 nanosheets using the microwave-assisted solvothermal method and subsequent calcination.to explore the gas sensing performance of these doped sheets, sensors were exposed to 10 ppm of NO_2 at room temperature, 5 %-Cd-Co_3O_4-based gas sensor displayed a better response value of 3.38 than the rest of the sensors with a recovery time of 620 s. This was attributed to increased oxygen vacancies by a suitable amount of Cd dopant, which led to enhanced gas sensing performance.

2.7.2 SMO n/p-p composites

The combination of Co_3O_4 with secondary SMO has also been reported as an effective way of improving the gas sensing performance, and this is attributed to the effects brought upon the heterojunction formation such as an increase in surface area, different sizes, and shapes of the nanoparticles that result in enhanced gas sensing. For example, due to the formation of p-n heterojunction between ZnO and Co_3O_4 nanograins, the 4:1 ZnO/Co_3O_4 composite sensor outperformed pure ZnO sensor in gas sensing

to NO_2. This was observed due to the synergistic effects between the constituent materials and a larger potential barrier height modulation of the junction which generally made more significant contribution to the response. Again, the gas sensing results showed that Co_3O_4 greatly improved the NO_2 gas sensing properties of ZnO-based gas sensors due to the chemical effects such as the prominent catalytic property of Co_3O_4, high oxygen adsorption property and creation of active adsorption sites by Co_3O_4 nanoparticles. The high catalytic ability of Co_3O_4 expedited the reactions associated with NO_2 gas sensing [115]. Qu et al. [116] prepared a p-n heterojunction of hierarchical Fe_3O_4@Co_3O_4 microspheres using the hydrothermal method. Fe_3O_4@Co_3O_4-based sensor obtained a maximum response value of 102.6 towards 100 ppm acetone gas at optimal temperature of 160°C and response and recovery of 5/15s in comparison with the pure Co_3O_4 and other Fe_3O_4-based sensors. The enhanced gas sensing performance was probably attributed to the synergetic effect of Fe_3O_4 and Co_3O_4 as well as the assembled heterojunction, making Fe_3O_4@Co_3O_4-based sensor a potential candidate for acetone gas sensing applications. P-n heterojunction Co_3O_4/In_2O_3 hollow microtubes were produced by Shi et al. [117] through hydrothermal synthesis followed by annealing treatment.

These hollow microtubes exhibited excellent gas sensing performance towards 50 ppm TEA at an optimal temperature of 250 °C with a response of 786.8 compared to those of pristine In_2O_3. This sensing behavior was ascribed to the combination of changing electronic materials, which led to enhanced charge carrier separation and migration. This in turn improved the sensor's response and sensitivity towards TEA gas molecules. Moreover, the combination of Co_3O_4 and In_2O_3 in the form of hollow microtubes created a large surface area, providing ample sites for TEA molecules to interact with the material, further enhancing the gas sensing performance.

On the other hand, Theka et al. [118] fabricated gas sensors based on MOF-derived Co_3O_4/TiO_2 and MOF-derived Fe/Co_3O_4/TiO_2 with varied Fe levels, i.e., 0.5 wt.%, 1.0 wt.% and 2.0 wt.% Fe/Co_3O_4/TiO_2. MOF-derived 1.0 wt. % Fe/Co_3O_4/TiO_2-based gas sensor exhibited a response of 3.1 towards 0.35 to 1.5 ppm benzene operating at 175 °C, compared to other sensors shown in **Figure 2.12(a).** This sensor showed selectivity towards benzene with minimal interference from other sensors, as shown respectively in **Figure 2.12(b)**, with 0.51 ppm^{-1} sensitivity and 4.17 ppb limit of detection. They attributed surface area, surface porosity, defects, and composition to the enhanced gas sensing properties displayed by the MOF-derived 1.0 wt. % Fe/Co_3O_4/TiO_2 based sensor. They furthermore explored the sensing mechanism of this sensor, nn ambient air, the formation of this heterostructure resulted in electron flow from TiO_2 to Co_3O_4, and hole flow from Co_3O_4 to TiO_2, creating a wide depletion layer in Co_3O_4's conduction band,

after the system balances at the Fermi level, as shown in **Figure 2.12(c)**. This was due to the higher work function of Co_3O_4 in comparison to Fe and TiO_2. The oxidation of Fe into Fe^{2+} and Fe^{3+} increased the depletion layer. The sensor based on 1.0 wt. %Fe/Co_3O_4/TiO_2 had a greater amount of electrons movement, making it more effective for the detection of benzene. **Figure 2,12(d)** shows a decrease in the resistance of the sensor because of oxygen gas adsorption due to the rising hole accumulation layer (HAL) when the sensor is in air. On the other hand, when the sensor was exposed to benzene gas, the reaction between the adsorbed oxygen gas and benzene gas caused a transfer of electrons to the conduction band, thus reducing the HAL (resulting in increased resistance), according to the equation:

$$C_6H_6 + 15O^-(ads) \rightarrow 6CO_2 + 3H_2O + 15e^- \quad (2.8)$$

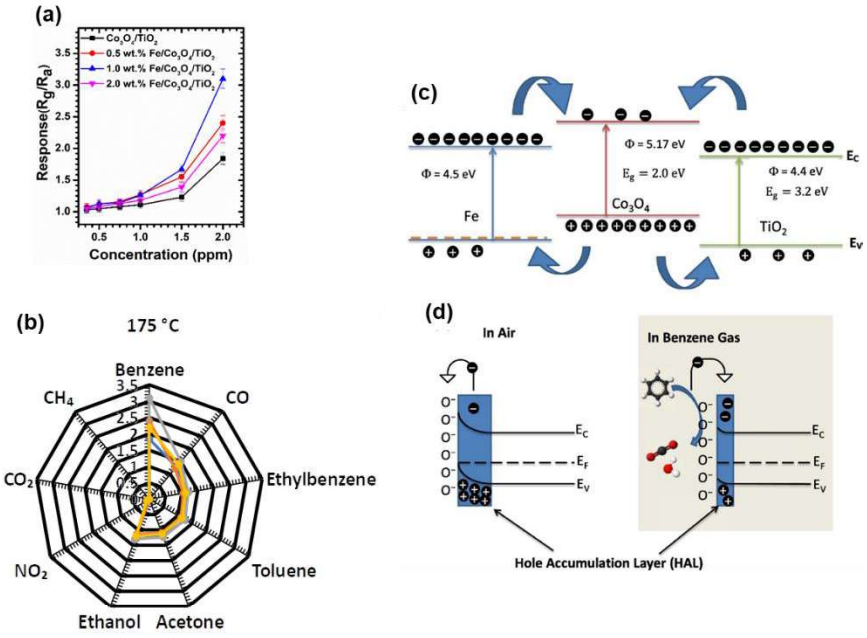

Figure 2. 9: (a) The response towards benzene by different sensors operating at 175 °C as a function of concentration; (b) a radar selectivity map of the sensors against a variety of gases at an operating temperature of 175 °C. Schematic illustrating sensor based on Fe/Co_3O_4/TiO_2 (c) energy band structure and (d) mechanism of sensing towards benzene [118].

Furthermore Bai et al. [119] reported successful incorporation of rhombic dodecahedron Co_3O_4/TiO_2 composites through pyrolyzes of a metal-organic framework (ZIF-67). These composites with different ratios were tested for gas sensing performance towards 50 ppm of xylene at 120 °C, The composite with a Co/Ti molar ratio of 4:1 exhibited the highest response of 6.17 which was 5 times higher than the pure Co_3O_4. This observation was attributed to the formation of a p-n junction that exposed more active sites

for easy adsorption of xylene gas and large modulation of resistance. Similarly, Ji et al. [120] reported on p-n heterojunction effects based on Co_3O_4/In_2O_3 flower-like prepared by hydrothermal synthesis. The gas sensing tests of the Co_3O_4/In_2O_3 and pure In_2O_3-based gas sensors were performed towards 10 ppm TMA at 200 °C and 250 °C, respectively. 5% Co_3O_4/In_2O_3 showed a good response of 11.67, which was 123.14% higher than that of pure In_2O_3 (5.23), with the shortest response and recovery time of 25/68 s. The reason for enhanced sensitivity towards TMA of the p-n heterojunction depicted in it was because of the expansion of the electron depletion layer width caused by the two materials.

Wu et al. [121] presented p-p heterojunction, $CoWO_4$-Co_3O_4 irregular spherical nanocomposites attained from off-stoichiometric cobalt tungstate synthesized using a hydrothermal route, and the samples were carried out as an atomic percentage of W/Co in the compositions 15, 25, 30, 40% and pure Co_3O_4. All the sensors were exposed to 100 ppm xylene at 200 °C, the $CoWO_4$-Co_3O_4-based sensors all exhibited a higher response towards xylene compared to the Co_3O_4-based sensor with a response of 4.4 displayed in **Figure 2.13(a-b)**. Furthermore, the $CoWO_4$-Co_3O_4 (W/Co = 30 at. %) sensor displayed the highest xylene response of 51.6 compared to the rest of the sensors with a response and recovery time of 236/254 s depicted in **Figure 2.13(c).** In addition, the sensor displayed long-term stability and strong anti-humidity in **Figure 2.13(d-f)**. This is owing to the presence of p-p heterojunction which promoted efficient charge carrier transport as shown in **Figure 2.13(g-h)**, Consequently, increased the [W]:[Co] atom ratio that influenced the quantity of p-p heterojunctions in the $CoWO_4$-Co_3O_4 nanocomposites, thereby increasing the sensors' resistance. As depicted in **Figure 2.13(i-j)** when exposed to air, the adsorbed oxygen molecules led to the formation of a Hole accumulation layer, when the Hole accumulation layer is higher than the interior core parts of the materials it resulted in the charge carrier migration, when exposed to Xylene the trapped electrons by chemisorbed oxygen molecules were released and recombined with the holes in the valence band, resulting in a reduced Hole accumulation layer and increased resistance, thus reflecting a better sensing response.

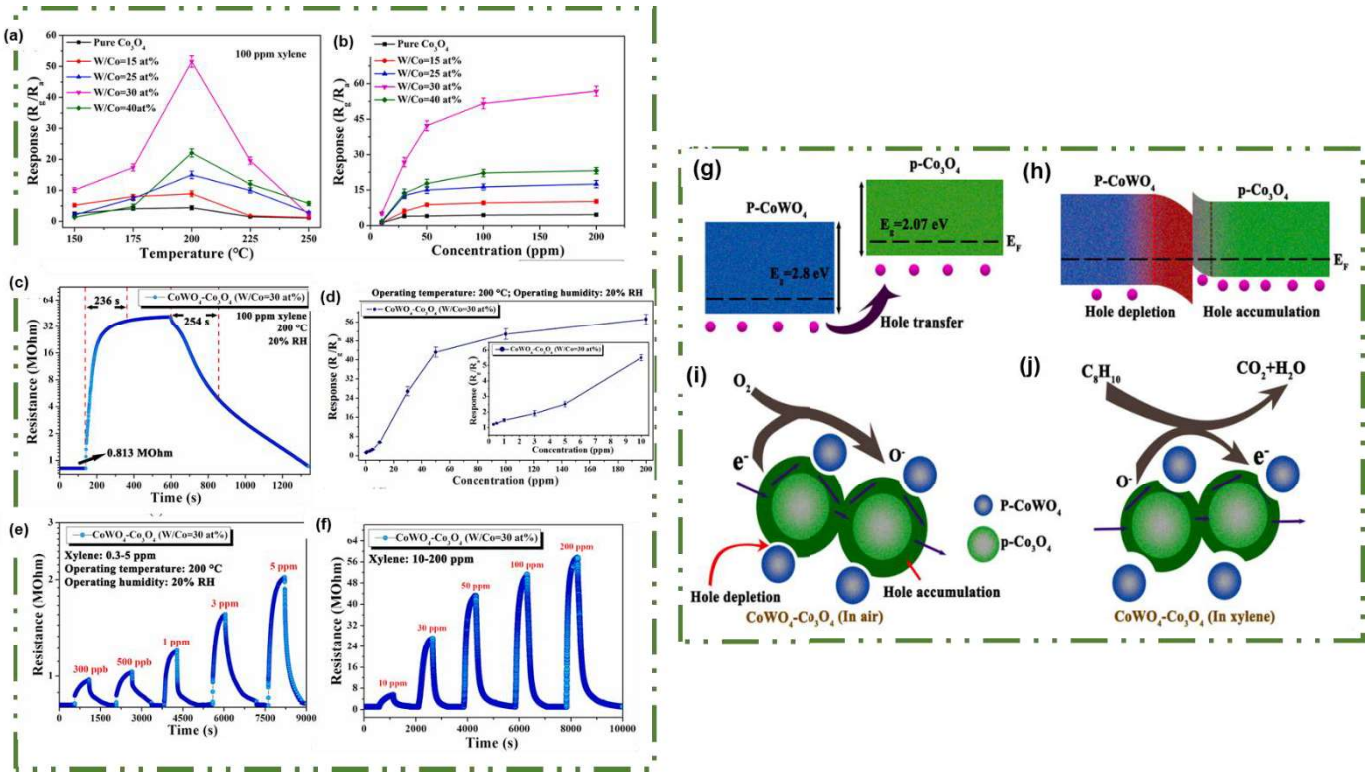

Figure 2. 10: (a) Responses of the Co_3O_4 and $CoWO_4$-Co_3O_4 based gas sensors vs operating temperatures to 100 ppm xylene; (b) The linear relationship between response and concentration of the Co_3O_4 and $CoWO_4$-Co_3O_4 based sensors (c) dynamic resistance change transients of the $CoWO_4$-Co_3O_4 (W/Co = 30 at%) based sensor to 100 ppm xylene (d) gas response of $CoWO_4$-Co_3O_4 (W/Co = 30 at%) to different concentrations of xylene at 200 °C (e, f) Dynamic response of the $CoWO_4$-Co_3O_4 (W/Co = 30 at%) sensor to different concentrations of xylene. (g-h) The energy band structures of p-p $CoWO_4$-Co_3O_4 heterojunctions (g) before and (h) after contacting; (i and j) the carrier transport model of Co_3O_4 and $CoWO_4$-Co_3O_4 sensitive materials in air and xylene [121].

In another work, Zhang et al. [122] fabricated p-p sheet-like nanocomposites by forming a NiO/Co_3O_4 heterojunction through hydrothermal synthesis and subsequent heat treatment at 450 °C. Five samples were carried out, pure NiO, Co_3O_4, 3 wt.% NiO/Co_3O_4, 6 wt.% NiO/Co_3O_4 and 9 wt.% NiO/ Co_3O_4. The response values of these sensors were tested towards 100 ppm xylene. 6 wt. % NiO/Co_3O_4 sensor exhibited a high response value of 12.27 at 140 °C with a response and recovery time of 30/53 s compared to the rest of the sensors including the pure Co_3O_4 sensor (3.25) and NiO sensor which exhibited negligibly low response. The improved gas performance was linked to the creation of a p-p, NiO/Co_3O_4 heterostructure. This occurred because the valence band energies of Co_3O_4 and NiO differ. When the heterostructure formed, holes moved at the interface until reaching equilibrium. Consequently, the p-p heterojunction created numerous grain boundary barriers, reducing hole concentration, and increasing resistance. Previous studies indicated that this heightened baseline resistance enhanced gas sensing

capabilities. Chen et al. [123] synthesized apple-like NiO/Co_3O_4 hetero-nanocomposites through a facile two-step chemical route. The gas sensing performance of the composite was investigated towards 300 ppm of CO at 150 °C. The NiO/Co_3O_4 composite-based gas sensor responded better (approximately 150%) compared to pristine Co_3O_4. The significant response was attributed to better dispersion of NiO/Co_3O_4 nano assemblies as well as the catalytic nature of NiO.

2.7.3 Noble Metals loading

Noble metals, such as gold (Au), silver (Ag), platinum (Pt), and palladium (Pd), are often used to enhance the gas sensing performance of SMO-based sensors as auxiliary materials by improving their catalytic activity, increasing surface area, enhancing selectivity, ensuring stability, enabling operation at lower temperatures, modifying electronic properties, and facilitating electronic sensitization and chemical sensitization known as spillover effect. These factors collectively lead to sensors with higher sensitivity, selectivity, and overall reliability in gas detection applications.

For example, Molavi et al.[124] used the co-precipitation method to synthesize Co_3O_4 nanoparticles for the detection of CO gas, the pristine nanoparticles were tested towards 800 ppm CO gas at a working temperature of 130 °C, and the maximum response value obtained was 60%. To enhance the gas performance of these Co_3O_4 nanoparticle-based sensors, Ag nanoparticles were loaded on the pure Co_3O_4 nanoparticles by using the solution impregnation method. Ag-Co_3O_4 nanoparticles were then exposed to the CO gas under the same conditions as the pristine Co_3O_4 nanoparticles and they exhibited a maximum response value of 85%. This observation was ascribed to the improving effect of Ag on the sensitivity of Co_3O_4 through activation energy evaluation and electronic mechanism in the energy levels of Ag-Co_3O_4 heterocontact.

On the other hand, Koo et al. [125] produced Co_3O_4 hollow nanocages, Co_3O_4 powders, and PdO catalyst functionalized Co_3O_4 hollow nanocages through precipitation and metal–organic framework (MOF) templates. The gas sensing properties of all these sensors were evaluated by exposing them to 5 ppm acetone gas at 350 °C. PdO Co_3O_4 hollow nanocages attained a high response of 2.51 compared to the Co_3O_4 hollow nanocages (1,45) and Co_3O_4 powders (1.96). The enhanced behavior was attributed to the effects of hollow structure and the nanoscale catalyst of Pd nanoparticles loaded on Co_3O_4. Furthermore, Li et al. [126] reported on pure and MOF-derived Au-loaded Co_3O_4 porous hollow nanocages produced by using ZIF-67 as a template. Responses of pure and MOF-derived Au-loaded Co_3O_4 sensors towards 100 ppm acetone at an optimal temperature of 190 °C were observed whereby pure Co_3O_4 sensor reached

a maximum response value of 5.5 while MOF-derived Au/Co_3O_4-sensor reached its maximum response value of 14.5 which was 2.6 times higher than that of pure Co_3O_4 sensor. The performance of improved acetone-sensing was discussed due to the gas accessibility of nanocage structures and the catalytic effect of Au. Moreover, Ma et al. [127] prepared Co_3O_4 nanocubes (NCs) and Pt-supported Co_3O_4 nanocubes using free synthetic conditions, to examine the effect of Pt in gas sensing both sensors were tested towards 500 ppb acetone at 200 °C. The Pt–Co_3O_4 NCs-based sensors showed an enhanced p-type response of 3.1 compared to other Co_3O_4 sensors in the detection of acetone gas. The improved properties of the Pt–Co_3O_4 NCs were attributed to their cubic shape with the exposed {100} planes of Co_3O_4, these crystal facets had distinct surface energies and reactivity compared to other facets. In addition to the loaded Pt nanoparticles, Pt nanoparticles facilitated catalytic reactions, which increased the active sites available for reactions, and enhanced the overall catalytic performance of the nanocomposite material.

Kruefu et al. [128] successfully synthesized Co_3O_4 nanoparticles loaded with 0.25, 0.50, and 1.00 wt.% Ruthenium (Ru) using precipitation and impregnation techniques, gas sensing response was studied by exposing the Ru-Co_3O_4 based gas sensors to 100 ppm of ethanol (C_2H_5OH), 0.25 wt.%Ru/Co_3O_4 sensor obtained maximum sensitivity of 30 at 350°C with a response and recovery time of 4.8/600 s. Ethanol sensing improvement was attributed to the catalytic nature of the Ru noble metal and the effects it has on the surface area. It also acted as a catalyst that tempered with the C_2H_5OH oxidation state resulting in a spillover onto adjacent Co_3O_4 surfaces.

Shin et al. [129] fabricated nano-grained Ag-Co_3O_4 Core-shell-based gas sensors through chemical synthesis techniques. Gas sensing properties of these sensors were investigated towards 50 ppm of xylene at 250 °C. The response curve displayed a response of 2.47 by Ag-Co_3O_4 Core-shell based gas sensors more than that of pristine Co_3O_4 (1.26) with a response and recovery time of 1272/ 5989 s. This behavior was ascribed to the porous nature of THE Co_3O_4 Core-shell and Ag catalytic effect which dissociated the adsorbed oxygen molecules to “O” during the spillover mechanism demonstrated in **Figure 2.14 (a-b)** to the neighboring Co_3O_4 surfaces which then led to increased oxygen gas/surface reaction. The spillover effect is a crucial mechanism in gas sensing facilitated by noble metals with the chemical sensitization part of it involving the migration of adsorbed species to different adjacent surface sites and changes in surface states for improved adsorption and electronic sensitization involving an increment of the depletion layer because of noble metals acting as electron acceptors. This effect is caused by the catalytic ability of noble metals that affects the oxidation of the gases introduced [130].

Yue et al. [131] synthesised Ag-Co_3O_4 nanowires using the nanocasting synthesis method with different amounts of Ag concentration, for toluene gas sensing applications, both loaded and pristine Co_3O_4-based sensors were tested towards 100 ppm of toluene, at 210 °C for pure Co_3O_4-sensor and 190 °C for the loaded sensor. Ag0.166-Co_3O_4 NW gas sensor exhibited a maximum response of 15.32 with a response and recovery time of 141/164 s, then the pure Co_3O_4 sensor reached a maximum response of 5.04 and response/recovery time of 141/170 s. The observed results were due to the spillover effect mechanism as depicted in **Figure 2.14 (c-d)** and high surface area.

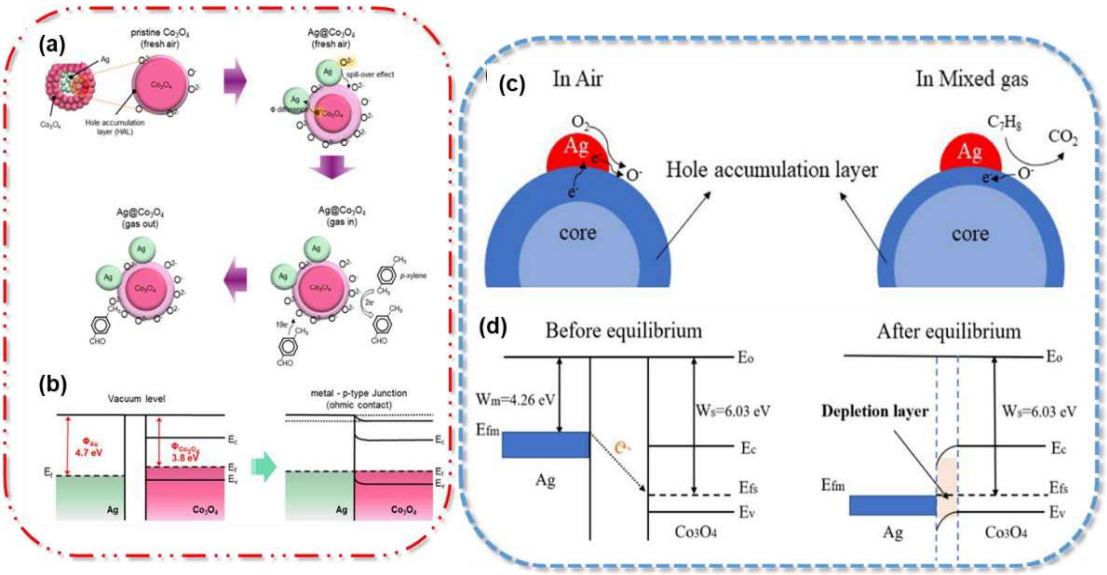

Figure 2. 11: (a) Schematic illustration of the sensing mechanism of nanograined Ag-Co_3O_4 C-S structure gas sensors. (b) Band diagram of Ag and Co_3O_4 before and after contact in the air [129], (a) Surface spillover mechanism of Ag-anchored Co_3O_4 NWs sensors, (b) Energy band diagram and electron transfer in Ag-anchored Co_3O_4 NWs before and after equilibrium [131].

2.8 Density Functional Theory (DFT)

Density Functional Theory (DFT) is a computational quantum modelling complementary method to the experimental studies, used in gas sensing to gain atomic-level information about the gas sensor and its sensing mechanism, this method simulates interactions between the gas molecule and the surface of the sensing material. It can provide details such as atomic geometries and the nature of chemical bonding on the surface-adsorbate interactions by outputting their energies and electronic properties, this highlights its importance in gas sensing applications [132].

2.8.1 Fundamentals of DFT

DFT is derived from the Hohenberg-Kohn theorems [133] and Kohn-Sham equations [134], DFT calculations rely on the electron density rather than wave functions, with the theory being exact for energy and electron density principle, knowing only the exchange-correlation functional. The theorems given by Hohenberg-Kohn are exact, but they are not necessarily useful in real calculations. To help transform DFT into a practical tool; Kohn-Sham equations were used, by simplifying the problem of electrons interacting in an external effective potential (V_{ext}) into non-interacting electrons in V_{ext}, allowing the determination of total energy for a system of interacting electrons in a fixed ground state.

Theorem 1 states that the external potential uniquely depends on the electron density. If two systems with different potentials($V_1(\vec{r})$ and $V_2(\vec{r})$) but the same ground-state density($n(\vec{r})$) are compared, their potential difference must be constant. This implies that the ground-state density uniquely determines the potential and all system properties, including the many-body wave function. The Hohenberg-Kohn functional:

$$F[n] = T[n] + U[n], \quad (2.9)$$

is a universal functional of density, not relying explicitly on external potential.

Theorem 2 asserts that the functional providing the ground state energy yields the lowest energy only when the input density is the true ground state density. For any positive integer **n** and potential $V(\vec{r})$, there exists a density functional F[n] such that the total energy E(v, N) for a given density n and potential can be expressed as the sum of F[N] and the integral of v(r)n(r) over space.

2.8.2 Exchange-correlation approximations

Exchange-correlation approximations are used in DFT to approximate the exchange and correlation energies between electrons in a many-electron system. **Figure 2.15** depicts different exchange-correlation approximations, for a better understanding each one of them is explained in detail below:

The Local Density Approximation (LDA) [135], initiated by Kohn and Sham, states that the exchange-correlation functional anywhere in space depends on spin density location. Even though LDA is the most used, and quite correct for geometries [136], it has its drawbacks such as over-binding atoms and molecules, making it less effective for thermo-chemistry. Another mostly used exchange-correlation approximation is The Generalized Gradient Approximation (GGA) [137] which simply extends the LDA component that includes terms that are dependent on density derivatives. Formation of other GGAs such as the PW86 and PW91functional models [138,139] comes from real-space cutoffs applied by Perdew.

PBE [140] is the most widely used GGA to study materials today, whereas in chemistry BLYP and Lee-Yang-Parr correlation [141,142] are generally employed GGA. A hybrid GGA combines a normal GGA

and a Hartree-Fock component, which uses the kinetic energy density to define the GGA component. The GGA, Hartree-Fock, and kinetic energy density components are all combined in a meta-hybrid [143]. The Density Functional (DF) consists of a part of GGA, LDA, Hartree-Fock exchange or hybrids, and meta-GGA, known as the exchange-and-correlation (XC) functional (meta-GGA or meta-hybrid). Moreover, the addition of an orbital-dependent correlation may also rely on virtual Kohn-Sham orbitals (double-hybrids) [144].

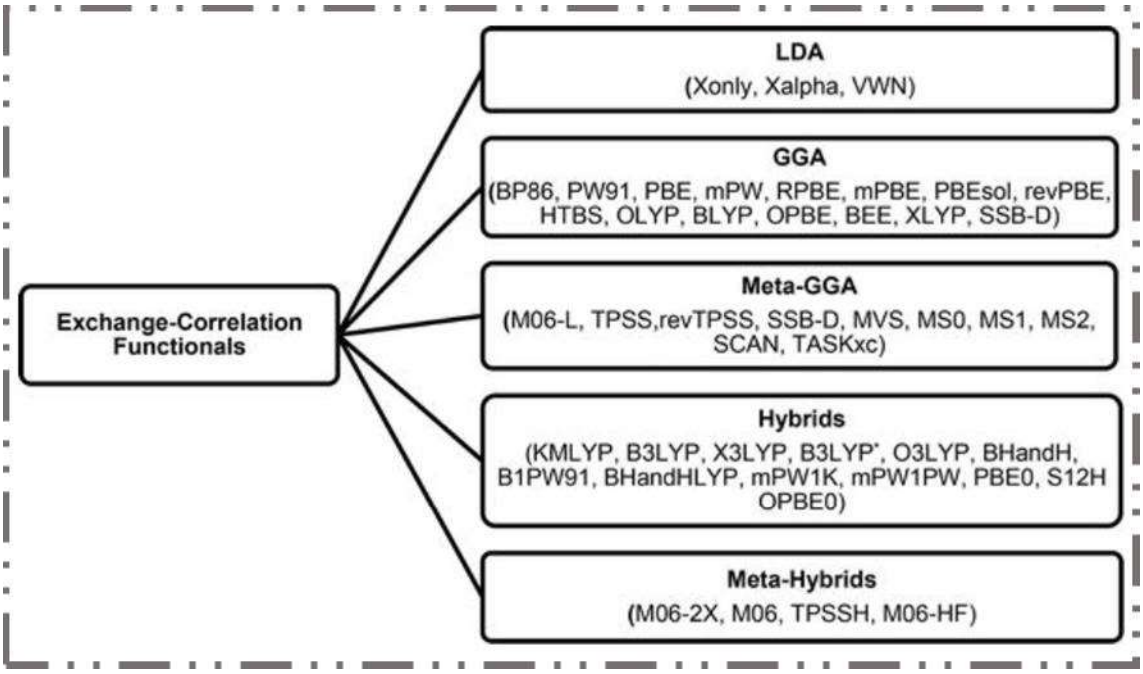

Figure 2. 12: Exchange-Correlation functionals [145]

2.8.3 Gas-Sensing mechanism using DFT

Various processes in gas sensing mechanisms such as adsorption, chemisorption, and surface reactions are important when gas molecules interact with the surface of the sensing materials. DFT is employed to study and understand these processes by calculating adsorption energies, charge transfer, and reaction pathways. adsorption energies indicate the spontaneity of the adsorption process, charge transfer provides information about the electronic interactions during the adsorption process. Furthermore, reaction pathways of gas molecules on the sensor surface, allow for a detailed understanding of the surface reactions involved in gas sensing. These gas-sensing capabilities make DFT a powerful complementary tool for investigating the fundamental mechanisms underlying gas-sensing processes.

Li et al. [146] prepared Co_3O_4 surfaces with (111) and (110) facets exposed using VASP (Vienna Ab initio Simulation Package) to study the adsorption capabilities of ethanol molecules. Co_3O_4 (110) had five adsorption configurations based on the hydroxyl group of ethanol adsorbing between Co^{3+} and O_{2c}, Co^{3+}, and O_{3c} labeled S1-S4, and a methyl group of ethanol molecule adsorbed on top of O_{2c} labeled S5. adsorption energies obtained were − 3.44, -2.91, -2.18, and -2.85 eV for sites S1-S4, and -0.42 eV for S5 respectively, these adsorption energies suggested that the hydroxyl was more adsorbed on the surface than the methyl group, moreover, suggested stable adsorption. The calculated adsorption energy on Co_3O_4 (111) was found to be -0.53 eV, compared to the adsorption energies obtained for Co_3O_4 (110), the ethanol molecule was efficiently and more easily absorbed on the surface of Co_3O_4 (110). Furthermore, the ethanol adsorption displayed a greater charge transfer of -0.11, -0.10, -0.12, -0.10, and 0.006 e for the Co_3O_4 (110) surface of site S1-S5, respectively, compared with that of Co_3O_4 (111) for -0.03 e. This observation was attributed to the chemical adsorption behavior of hydroxyl in ethanol with Co and O_{2c} on the Co_3O_4 (110) surface and the highly sensitive ethanol sensing capabilities.

The overall excellent gas sensing capabilities of Co_3O_4 (110) towards ethanol were ascribed to the synergistic effect of adsorption shown in **Figure 2.16(a)**. Ji et al. [147] employed DFT to investigate the mercury (Hg^0) adsorption mechanism on the Co_3O_4 (11 0) surface. Two different surfaces were prepared, surface I had parameters of **a** = 8.125 Å, **b** = 5.745 Å, and Surface II had parameters of **a** = 8.125 Å and **b** = 11.490 Å, this was performed to observe which model was best suited for research, it was gauged through adsorption energy of Hg on each surface. For surface I adsorption energy was found to be -74.037 kJ/mol and for surface II was found to be -74.179 kJ/mol. This observation suggested surface I to be the most suitable model for research as it is large enough compared to surface II. Different Hg adsorption sites shown in **Figure 2.16(c)** were studied in detail to find the most stable configuration on the Co_3O_4(110) surface. Adsorption energies were found to be -63.037 kJ/mol for the Co^{3+} site and -74.037 kJ/mol for the O^{4f} site, from this results they indicated that the Co^{3+} site is less stable compared to the O^{4f} site, furthermore Hg^0, on the top site of O^{4f}, had the biggest charge transfer of 0.224 electrons after adsorption, which emphasized that Hg has oxidized after adsorption consequently resulted in a very stable state of Hg adsorption. Furthermore, Feng et al. [148] investigated acetone adsorption on the Co_3O_4 (111) surface through DFT. Three adsorption configurations were prepared for acetone, formaldehyde, and butanone, adsorption energies were found to be 1.86, 1.10, and 1.28 respectively, and transferred electrons of 0.16, 0.11, and 0.09 e. All the adsorption energies were positive indicating the exothermic nature of the adsorption processes. with the adsorption energy of acetone being larger than the other two,

it suggested that the acetone molecules were easily adsorbed on the surface. Furthermore, a high number of electrons transferred for acetone adsorption was represented in **Figure 2.16(b)** by O atom and Co atom regions which appeared darker red and blue respectively through Hirshfeld charge analysis. All the observations suggested that acetone molecules were more easily adsorbed on the Co_3O_4 (111) surface.

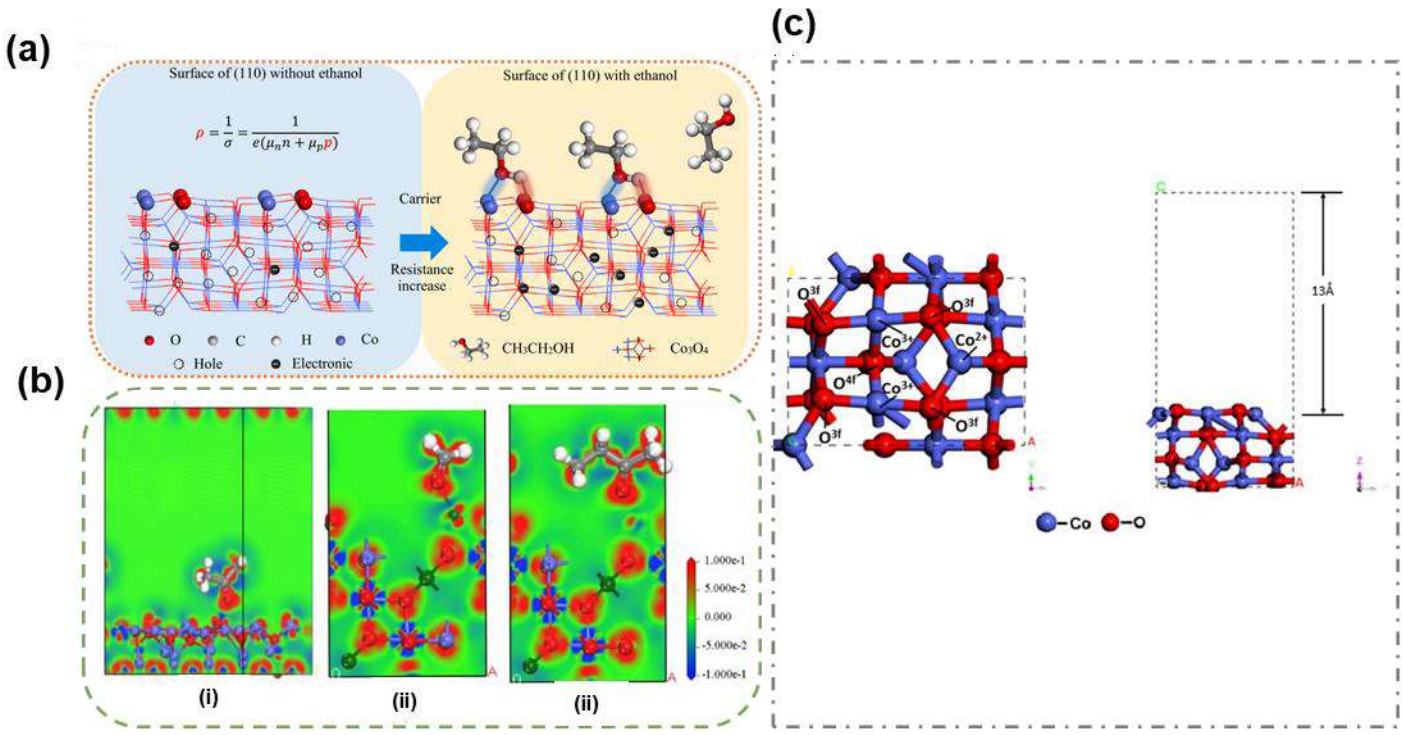

Figure 2. 13: (a) Sensing mechanism of the Co_3O_4 (110) without and with ethanol gas [146], (b) Differential charge diagram of gas adsorption to Co_3O_4 (111) surface: (i) Acetone; (ii) Formaldehyde; (iii) Butanone [148] and (c) Top view and side view of clean Co_3O_4(11 0) surfaces [147].

2.9 References

[1] A. Khorramifar, H. Karami, L. Lvova, A. Kolouri, E. Łazuka, M. Piłat-Rożek, G. Łagód, J. Ramos, J. Lozano, M. Kaveh, Environmental Engineering Applications of Electronic Nose Systems Based on MOX Gas Sensors, Sensors. 23 (2023) 5716.

[2] Y.C. Wong, B.C. Ang, A. Haseeb, A.A. Baharuddin, Y.H. Wong, Conducting polymers as chemiresistive gas sensing materials: A review, J. Electrochem. Soc. 167 (2020) 037503.

[3] A. Husain, S. Ahmad, F. Mohammad, Synthesis, characterisation and ethanol sensing application of polythiophene/graphene nanocomposite, Mater. Chem. Phys. 239 (2020) 122324.

[4] Z. Guo, N. Liao, M. Zhang, A. Feng, Enhanced gas sensing performance of polyaniline incorporated with graphene: A first-principles study, Phys. Lett. A. 383 (2019) 2751-2754.

[5] M. Reddeppa, T. Chandrakalavathi, B. Park, G. Murali, R. Siranjeevi, G. Nagaraju, J.S. Yu, R. Jayalakshmi, S. Kim, M. Kim, UV-light enhanced CO gas sensors based on InGaN nanorods decorated with p-Phenylenediamine-graphene oxide composite, Sensors Actuators B: Chem. 307 (2020) 127649.

[6] K.G. Krishna, S. Parne, N. Pothukanuri, V. Kathirvelu, S. Gandi, D. Joshi, Nanostructured metal oxide semiconductor-based gas sensors: A comprehensive review, Sens. Actuator A Phys. 341 (2022) 113578.

[7] R.S. Ganesh, E. Durgadevi, M. Navaneethan, V.L. Patil, S. Ponnusamy, C. Muthamizhchelvan, S. Kawasaki, P.S. Patil, Y. Hayakawa, Low temperature ammonia gas sensor based on Mn-doped ZnO nanoparticle decorated microspheres, J. Alloys Compounds. 721 (2017) 182-190.

[8] S. Das, V. Jayaraman, SnO_2: A comprehensive review on structures and gas sensors, Prog. Mater. Sci. 66 (2014) 112-255.

[9] J. Yoon, H. Kim, H. Jeong, J. Lee, Gas sensing characteristics of p-type Cr_2O_3 and Co_3O_4 nanofibers depending on inter-particle connectivity, Sensors Actuators B: Chem. 202 (2014) 263-271.

[10] X. San, G. Wang, B. Liang, J. Ma, D. Meng, Y. Shen, Flower-like NiO hierarchical microspheres self-assembled with nanosheets: Surfactant-free solvothermal synthesis and their gas sensing properties, J. Alloys Compounds. 636 (2015) 357-362.

[11] B. Saruhan, R. Lontio Fomekong, S. Nahirniak, Review: influences of semiconductor metal oxide properties on gas sensing characteristics. Front Sens. (2021).

[12] L. Liu, Y. Wang, Y. Liu, S. Wang, T. Li, S. Feng, S. Qin, T. Zhang, Heteronanostructural metal oxide-based gas microsensors, Microsyst. Nanoeng. 8 (2022) 85.

[13] T.P. Mokoena, H.C. Swart, K.T. Hillie, Z.P. Tshabalala, M. Jozela, J. Tshilongo, D.E. Motaung, Enhanced propanol gas sensing performance of p-type NiO gas sensor induced by exceptionally large surface area and crystallinity, Appl. Surf. Sci. 571 (2022) 151121.

[14] X. Yang, Y. Deng, H. Yang, Y. Liao, X. Cheng, Y. Zou, L. Wu, Y. Deng, Functionalization of mesoporous semiconductor metal oxides for gas sensing: Recent advances and emerging challenges, Adv. Sci. 10 (2023) 2204810.

[15] Z. Dou, C. Cao, Y. Chen, W. Song, Fabrication of porous Co_3O_4 nanowires with high CO sensing performance at a low operating temperature, Chem comm. 50 (2014) 14889-14891.

[16] X. Zhang, J. Wang, L. Xuan, Z. Zhu, Q. Pan, K. Shi, G. Zhang, Novel Co_3O_4 nanocrystalline chain material as a high performance gas sensor at room temperature, J. Alloys Compounds. 768 (2018) 190-197.

[17] J. Tan, M. Dun, L. Li, J. Zhao, W. Tan, Z. Lin, X. Huang, Synthesis of hollow and hollowed-out Co_3O_4 microspheres assembled by porous ultrathin nanosheets for ethanol gas sensors: responding and recovering in one second, Sensors Actuators B: Chem. 249 (2017) 44-52.

[18] W. Tan, J. Tan, L. Li, M. Dun, X. Huang, Nanosheets-assembled hollowed-out hierarchical Co_3O_4 microrods for fast response/recovery gas sensor, Sensors Actuators B: Chem. 249 (2017) 66-75.

[19] S.A. Makhlouf, Z.H. Bakr, K.I. Aly, M.S. Moustafa, Structural, electrical and optical properties of Co_3O_4 nanoparticles, Superlattices and Microstructures. 64 (2013) 107-117.

[20] L.J. Cardenas-Flechas, J.J. Barba-Ortega, M.R. Joya, Analysis and evaluation of structural properties of Co_3O_4 microparticles obtained at low temperature, Cerâmica. 68 (2022) 52-59.

[21] P. Cossee, Structure and magnetic properties of Co_3O_4 and $ZnCo_2O_4$, Recl. Trav. Chim. Pays-Bas. 75 (1956) 1089-1096.

[22] L.J. Cardenas-Flechas, A.M. Raba, M. Rincón-Joya, Synthesis and evaluation of nickel doped Co_3O_4 produced through hydrothermal technique, Dyna. 87 (2020) 184-191.

[23] S. Giri, P.N. Anantharamaiah, B. Sahoo, Sensing of oxidizing and reducing gases by sensors prepared using nanoscale Co_3O_4 powders: A study through Cu substitution, Advanced Powder Technology. 33 (2022) 103529.

[24] Y. Yuan, Y. Wang, X. He, M. Chen, J. Liu, B. Liu, H. Zhao, S. Liu, H. Yang, Increasing gas sensitivity of Co_3O_4 octahedra by tuning Co-Co_3O_4 (111) surface structure and sensing mechanism of 3-coordinated Co atom as an active center, J. Mater. Sci. : Mater. Electron. 31 (2020) 8852-8864.

[25] Q. Zhou, W. Zeng, Shape control of Co_3O_4 micro-structures for high-performance gas sensor, Physica E: Low-dimensional Systems and Nanostructures. 95 (2018) 121-124.

[26] T. Waitz, T. Wagner, T. Sauerwald, C. Kohl, M. Tiemann, Ordered mesoporous In_2O_3: synthesis by structure replication and application as a methane gas sensor, Adv. Funct. Mater. 19 (2009) 653-661.

[27] E. Comini, C. Baratto, I. Concina, G. Faglia, M. Falasconi, M. Ferroni, V. Galstyan, E. Gobbi, A. Ponzoni, A. Vomiero, Metal oxide nanoscience and nanotechnology for chemical sensors, Sensors Actuators B: Chem. 179 (2013) 3-20.

[28] J.N. Tiwari, R.N. Tiwari, K.S. Kim, Zero-dimensional, one-dimensional, two-dimensional and three-dimensional nanostructured materials for advanced electrochemical energy devices, Progress in Materials Science. 57 (2012) 724-803.

[29] M. Yoshimura, K. Byrappa, Hydrothermal processing of materials: past, present and future, J. Mater. Sci. 43 (2008) 2085-2103.

[30] K. Choi, H. Kim, K. Kim, D. Liu, G. Cao, J. Lee, C_2H_5OH sensing characteristics of various Co_3O_4 nanostructures prepared by solvothermal reaction, Sensors Actuators B: Chem. 146 (2010) 183-189.

[31] C. Sun, X. Su, F. Xiao, C. Niu, J. Wang, Synthesis of nearly monodisperse Co_3O_4 nanocubes via a microwave-assisted solvothermal process and their gas sensing properties, Sensors Actuators B: Chem. 157 (2011) 681-685.

[32] X. Qiao, C. Ma, X. Chang, X. Li, K. Li, L. Zhu, F. Xia, Q. Xue, 3D radial Co_3O_4 nanorod cluster derived from cobalt-based layered hydroxide metal salt for enhanced trace acetone detection, Sensors Actuators B: Chem. 327 (2021) 128926.

[33] R. Guo, X. Hou, C. Shi, W. Zhang, Y. Zhou, MOF-derived Co_3O_4 hierarchical porous structure for enhanced acetone sensing performance with high sensitivity and low detection limit, Sensors Actuators B: Chem. 376 (2023) 132973.

[34] S. Li, X. Wei, S. Zhu, Q. Zhou, Y. Gui, Low temperature carbon monoxide gas sensor based on Co_3O_4@ TiO_2 nanocomposites: theoretical and experimental analysis, J. Alloys Compounds. 882 (2021) 160710.

[35] L. Guo, F. Chen, N. Xie, C. Wang, X. Kou, Y. Sun, J. Ma, X. Liang, Y. Gao, G. Lu, Metal–organic frameworks derived tin-doped cobalt oxide yolk-shell nanostructures and their gas sensing properties, J. Colloid Interface Sci. 528 (2018) 53-62.

[36] C. Busacca, A. Donato, M.L. Faro, A. Malara, G. Neri, S. Trocino, CO gas sensing performance of electrospun Co_3O_4 nanostructures at low operating temperature, Sensors Actuators B: Chem. 303 (2020) 127193.

[37] J. Deng, R. Zhang, L. Wang, Z. Lou, T. Zhang, Enhanced sensing performance of the Co_3O_4 hierarchical nanorods to NH_3 gas, Sensors Actuators B: Chem. 209 (2015) 449-455.

[38] S. Tyagi, M. Chaudhary, A.K. Ambedkar, K. Sharma, Y.K. Gautam, B.P. Singh, Metal oxide nanomaterial-based sensors for monitoring environmental NO_2 and its impact on the plant ecosystem: A review, Sens. diagn. 1 (2022) 106-129.

[39] N. Goel, K. Kunal, A. Kushwaha, M. Kumar, Metal oxide semiconductors for gas sensing, Eng. Rep. 5 (2023) e12604.

[40] H. Zhang, W. Chen, Y. Li, Z. Song, Gas sensing performances of ZnO hierarchical structures for detecting dissolved gases in transformer oil: A mini review, Frontiers in chemistry. 6 (2018) 508.

[41] K.G. Krishna, S.R. Parne, P. Nagaraju, Low cost ternary metal oxide based nanocomposites as a room temperature formaldehyde sensor, Phys. Scripta. (2023).

[42] R. Pandey, P. Kumar, P. Sharma, R. Punia, Chapter 7 - Challenges and future prospects in bioelectrochemical sensors, in: L. Singh, D. Mahapatra, S. Kumar (Eds.), Multifaceted Bio-Sensing Technology, Academic Press, 2023, pp. 99-110.

[43] V.E. Bochenkov, G.B. Sergeev, Sensitivity, selectivity, and stability of gas-sensitive metal-oxide nanostructures, Metal oxide nanostructures and their applications. 3 (2010) 31-52.

[44] Y. Sun, S. Liu, F. Meng, J. Liu, Z. Jin, L. Kong, J. Liu, Metal oxide nanostructures and their gas sensing properties: a review, Sensors. 12 (2012) 2610-2631.

[45] Y. Shimizu, SnO_2 gas sensor, Encyclopedia of Applied Electrochemistry. (2014) 1974-1982.

[46] J. Cao, S. Wang, X. Zhao, Y. Xing, J. Li, D. Li, Facile synthesis and enhanced toluene gas sensing performances of Co_3O_4 hollow nanosheets, Mater Lett. 263 (2020) 127215.

[47] S. Wang, J. Cao, W. Cui, L. Fan, X. Li, D. Li, T. Zhang, One-dimensional porous Co_3O_4 rectangular rods for enhanced acetone gas sensing properties, Sensors Actuators B: Chem. 297 (2019) 126746.

[48] J. Yoon, J. Choi, J. Lee, Design of a highly sensitive and selective C_2H_5OH sensor using p-type Co_3O_4 nanofibers, Sensors Actuators B: Chem. 161 (2012) 570-577.

[49] F. Qu, C. Feng, C. Li, W. Li, S. Wen, S. Ruan, H. Zhang, Preparation and xylene-sensing properties of Co_3O_4 nanofibers, Int. J. Appl. Ceram. 11 (2014) 619-625.

[50] F. Chen, Y. Zhang, D. Wang, T. Wang, J. Zhang, D. Zhang, High performance ammonia gas sensor based on electrospinned Co_3O_4 nanofibers decorated with hydrothermally synthesized MoTe2 nanoparticles, J. Alloys Compounds. 923 (2022) 166355.

[51] J. Wang, D. Zhang, Y. Gao, F. Chen, T. Wang, H. Xia, X. Sui, Z. Wang, Fast-response hydrogen sulfide gas sensor based on electrospinning Co_3O_4 nanofibers-modified CuO nanoflowers: Experimental and DFT calculation, Sensors Actuators B: Chem. (2023) 134579.

[52] P.H. Phuoc, L.T. Hong, N.T. Thang, N.H. Hanh, C.M. Hung, N.V. Duy, N.V. Hieu, N.D. Hoa, Fabrication of p-Type Co_3O_4 Nanofiber Sensors for Ultra-Low H_2S Gas Detection at Low Temperature, J. Nanosci. Nanotechnol. 21 (2021) 2626-2632.

[53] S. Jamil, X. Jing, J. Wang, J. Liu, M. Zhang, The synthesis of porous Co_3O_4 micro cuboid structures by solvothermal approach and investigation of its gas sensing properties and catalytic activity, Mater. Res. Bull. 48 (2013) 4513-4520.

[54] H. Sun, X. Tang, S. Li, Y. Yao, L. Liu, MOF-derived one-dimensional Ru/Mo co-doped Co_3O_4 hollow microtubes for high-performance triethylamine sensing, Sensors Actuators B: Chem. 383 (2023) 133583.

[55] D. Kong, J. Han, Y. Gao, Y. Gao, W. Zhou, G. Liu, G. Lu, Lower coordination Co_3O_4 mesoporous hierarchical microspheres for comprehensive sensitization of triethylamine vapor sensor, J. Hazard. Mater. 430 (2022) 128469.

[56] N.M. Yusof, S. Rozali, S. Ibrahim, S.Z. Siddick, Synthesis of hybridized fireworks-like go-Co_3O_4 nanorods for acetone gas sensing applications, Mater. Today Commun. 35 (2023) 105516.

[57] J. Zhang, Y. Chen, L. Li, X. Chen, W. An, X. Qian, Y. Tao, $LaMnO_3/Co_3O_4$ nanocomposite for enhanced triethylamine sensing properties, Journal of Rare Earths. (2023).

[58] G. Joshi, J.K. Rajput, L.P. Purohit, SnO_2–Co_3O_4 pores composites for CO_2 gas sensing at low operating temperature, Microporous Mesoporous Mater. 326 (2021) 111343.

[59] T.L. Simonenko, N.P. Simonenko, P.Y. Gorobtsov, A.S. Mokrushin, V.R. Solovey, V.M. Pozharnitskaya, E.P. Simonenko, O.V. Glumov, N.A. Melnikova, A.A. Lizunova, Pen plotter printing of Co_3O_4 thin films: features of the microstructure, optical, electrophysical and gas-sensing properties, J. Alloys Compounds. 832 (2020) 154957.

[60] A. Rawat, S. Panwar, L.P. Purohit, Hollow cylindrical ternary ZnO/Co_3O_4/CuO nanocomposite thick film on inter-digitated electrodes for selective ammonia gas sensing, Surf. Interfaces. 42 (2023) 103404.

[61] H. Liu, S. Jin, K. Zhang, Y. Jiang, Y. Feng, D. Li, P. Tang, Tuning the sensing selectivity of mesoporous hierarchical Ti-doped Co_3O_4 to toluene and xylene via controlling the oxygen defects, Appl. Surf. Sci. 614 (2023) 156079.

[62] D. Patil, P. Patil, V. Subramanian, P.A. Joy, H.S. Potdar, Highly sensitive and fast responding CO sensor based on Co_3O_4 nanorods, Talanta. 81 (2010) 37-43.

[63] M. Tian, J. Miao, P. Cheng, H. Mu, J. Tu, J. Sun, Layer-by-layer nanocomposites consisting of Co_3O_4 and reduced graphene (rGO) nanosheets for high selectivity ethanol gas sensors, Appl. Surf. Sci. 479 (2019) 601-607.

[64] T. Zhou, X. Liu, R. Zhang, Y. Wang, T. Zhang, NiO/$NiCo_2O_4$ truncated nanocages with PdO catalyst functionalization as sensing layers for acetone detection, ACS applied materials & interfaces. 10 (2018) 37242-37250.

[65] W. Yan, Y. Chen, X. Zeng, G. Wu, W. Jiang, D. Wei, M. Ling, K.W. Ng, Y. Qin, Ultrasensitive ethanol sensor based on segregated ZnO-In_2O_3 porous nanosheets, Appl. Surf. Sci. 535 (2021) 147697.

[66] X. Wang, W. Tian, T. Zhai, C. Zhi, Y. Bando, D. Golberg, Cobalt (II, III) oxide hollow structures: fabrication, properties and applications, J. Mater. Chem. 22 (2012) 23310-23326.

[67] L. Man, B. Niu, H. Xu, B. Cao, J. Wang, Microwave hydrothermal synthesis of nanoporous cobalt oxides and their gas sensing properties, Mater. Res. Bull. 46 (2011) 1097-1101.

[68] Y. Lin, H. Ji, Z. Shen, Q. Jia, D. Wang, Enhanced acetone sensing properties of Co_3O_4 nanosheets with highly exposed (111) planes, J. Mater. Sci. : Mater. Electron. 27 (2016) 2086-2095.

[69] M. Hussain, Z.H. Ibupoto, M.A. Abbasi, O. Nur, M. Willander, Effect of anions on the morphology of Co_3O_4 nanostructures grown by hydrothermal method and their pH sensing application, J Electroanal Chem. 717 (2014) 78-82.

[70] Y. Masuda, Recent advances in SnO_2 nanostructure based gas sensors, Sensors Actuators B: Chem. 364 (2022) 131876.

[71] V. Mandić, S. Kurajica, M. Plodinec, I. Panžić, Thermal Stability and Utilization of 1D-Nanostructured Co_3O_4 Rods Derived by Simple Solvothermal Processing, Catalysts. 12 (2022) 1162.

[72] P.X. Gao, Z.L. Wang, Mesoporous polyhedral cages and shells formed by textured self-assembly of ZnO nanocrystals, J. Am. Chem. Soc. 125 (2003) 11299-11305.

[73] A.L. Tiano, C. Koenigsmann, A.C. Santulli, S.S. Wong, Solution-based synthetic strategies for one-dimensional metal-containing nanostructures, ChemComm. 46 (2010) 8093-8130.

[74] W. Shi, S. Song, H. Zhang, Hydrothermal synthetic strategies of inorganic semiconducting nanostructures, Chem. Soc. Rev. 42 (2013) 5714-5743.

[75] H. Che, A. Liu, J. Hou, J. Mu, Y. Bai, S. Zhao, X. Zhang, H. He, Solvothermal synthesis of hierarchical Co_3O_4 flower-like microspheres for superior ethanol gas sensing properties, J. Mater. Sci. : Mater. Electron. 25 (2014) 3209-3218.

[76] M. Alheshibri, N.M. Shaalan, Q. A. Drmosh, A. Al Baroot, S. Akhtar, A. Aljaafari, H.S. Al Qahtani, K. Elsayed, Tailoring the surface morphology of nanostructured cobalt oxide for high-sensitivity CO sensor, J. Mater. Sci. 57 (2022) 12865-12874.

[77] M. Wang, Z. Shen, X. Zhao, F. Duanmu, H. Yu, H. Ji, Rational shape control of porous Co_3O_4 assemblies derived from MOF and their structural effects on n-butanol sensing, J. Hazard. Mater. 371 (2019) 352-361.

[78] T. Thomas, Y. Kumar, J.A. Ramos Ramón, V. Agarwal, S. Sepúlveda Guzmán, R. R, S. Pushpan, S.L. Loredo, K.C. Sanal, Porous silicon/α-MoO_3 nanohybrid based fast and highly sensitive CO_2 gas sensors, Vacuum. 184 (2021) 109983.

[79] J. Wawrzyniak, Advancements in Improving Selectivity of Metal Oxide Semiconductor Gas Sensors Opening New Perspectives for Their Application in Food Industry, Sensors. 23 (2023) 9548.

[80] J. Hu, X. Xiong, W. Guan, H. Long, Controllable fabrication of hierarchical bubble-like Co_3O_4 tubes with enhanced trimethylamine sensing performance, Sensors Actuators B: Chem. 389 (2023) 133886.

[81] Y. Lu, W. Zhan, Y. He, Y. Wang, X. Kong, Q. Kuang, Z. Xie, L. Zheng, MOF-templated synthesis of porous Co_3O_4 concave nanocubes with high specific surface area and their gas sensing properties, ACS applied materials & interfaces. 6 (2014) 4186-4195.

[82] J.M. Xu, J. Zhang, B.B. Wang, F. Liu, Shape-regulated synthesis of cobalt oxide and its gas-sensing property, J. Alloys Compounds. 619 (2015) 361-367.

[83] L. Wang, S.Y. Song, B. Hong, J.C. Xu, Y.B. Han, H.X. Jin, D.F. Jin, J. Li, Y.T. Yang, X.L. Peng, H.L. Ge, X.Q. Wang, Highly improved toluene gas-sensing performance of mesoporous Co_3O_4 nanowires and physical mechanism, Mater. Res. Bull. 140 (2021) 111329.

[84] M. Wang, T. Hou, X. Zhao, H. Yu, H. Ji, Crucial structural effects of porous Co_3O_4 derived from Prussian blue analogue on the enhanced gas sensing performance, Mater Lett. 242 (2019) 83-86.

[85] Y. Qiu, Y. Wang, Controllable synthesis of porous Co_3O_4 nanorods and their ethanol-sensing performance, Ceram. Int. 48 (2022) 29659-29668.

[86] Q. Jiang, X. Guo, C. Wang, L. Jia, Z. Zhao, R. Yang, P. Wang, Q. Deng, Polyvinylpyrrolidone-mediated Co_3O_4 microspheres assembled in size-tunable submicron spheres with porous core-shell structure for high-performance gases sensing, J. Alloys Compounds. 935 (2023) 167976.

[87] B. Zhang, M. Cheng, G. Liu, Y. Gao, L. Zhao, S. Li, Y. Wang, F. Liu, X. Liang, T. Zhang, Room temperature NO_2 gas sensor based on porous Co_3O_4 slices/reduced graphene oxide hybrid, Sensors Actuators B: Chem. 263 (2018) 387-399.

[88] Y. Xu, L. Zheng, C. Yang, W. Zheng, X. Liu, J. Zhang, Oxygen vacancies enabled porous SnO_2 thin films for highly sensitive detection of triethylamine at room temperature, ACS Appl. Mater. Interfaces. 12 (2020) 20704-20713.

[89] Y. Shi, T. Liu, Y. Zhao, J. Su, S. Zeb, Y. Nie, C. Qin, B. Wang, X. Jiang, Tunable oxygen vacancies of cobalt oxides for efficient gas sensing application, Sensors Actuators B: Chem. 350 (2022) 130860.

[90] H. Liu, H. He, L. Chen, Q. Pan, G. Zhang, Flower-like Co_3O_4 sensor with rich oxygen vacancy defects for enhancing room temperature NOx sensing performances, J. Alloys Compounds. 868 (2021) 159180.

[91] L. Cheng, Y. He, M. Gong, X. He, Z. Ning, H. Yu, Z. Jiao, MOF-derived synthesis of Co_3O_4 nanospheres with rich oxygen vacancies for long-term stable and highly selective n-butanol sensing performance, J. Alloys Compounds. 857 (2021) 158205.

[92] J. Fan, C. Yang, X. Zhao, D. Li, F. Xiao, R. Wu, L. Wang, Enhanced gas sensing property of Co_3O_4 matrix nanocomposites with halloysite nanotubes toward triethylamine, J. Mater. Res. Technol. 23 (2023) 2491-2503.

[93] D. Barreca, E. Comini, A.P. Ferrucci, A. Gasparotto, C. Maccato, C. Maragno, G. Sberveglieri, E. Tondello, First example of ZnO− TiO_2 nanocomposites by chemical vapor deposition: structure, morphology, composition, and gas sensing performances, Chemistry of Materials. 19 (2007) 5642-5649.

[94] A. Kusior, M. Radecka, M. Rekas, M. Lubecka, K. Zakrzewska, A. Reszka, B.J. Kowalski, Sensitization of gas sensing properties in TiO_2/SnO_2 nanocomposites, Procedia Engineering. 47 (2012) 1073-1076.

[95] A. Chen, S. Bai, B. Shi, Z. Liu, D. Li, C.C. Liu, Methane gas-sensing and catalytic oxidation activity of SnO_2–In_2O_3 nanocomposites incorporating TiO_2, Sensors Actuators B: Chem. 135 (2008) 7-12.

[96] X. Yu, G. Zhang, H. Cao, X. An, Y. Wang, Z. Shu, X. An, F. Hua, ZnO@ ZnS hollow dumbbells–graphene composites as high-performance photocatalysts and alcohol sensors, New J. Chem. 36 (2012) 2593-2598.

[97] S. Choi, J.Y. Park, S.S. Kim, Synthesis of SnO_2–ZnO core–shell nanofibers via a novel two-step process and their gas sensing properties, Nanotechnology. 20 (2009) 465603.

[98] W. Wang, Z. Li, W. Zheng, H. Huang, C. Wang, J. Sun, Cr_2O_3-sensitized ZnO electrospun nanofibers based ethanol detectors, Sensors Actuators B: Chem. 143 (2010) 754-758.

[99] H. Gu, Z. Wang, Y. Hu, Hydrogen gas sensors based on semiconductor oxide nanostructures, Sensors. 12 (2012) 5517-5550.

[100] M. Rumyantseva, V. Kovalenko, A. Gaskov, E. Makshina, V. Yuschenko, I. Ivanova, A. Ponzoni, G. Faglia, E. Comini, Nanocomposites SnO_2/Fe_2O_3: sensor and catalytic properties, Sensors Actuators B: Chem. 118 (2006) 208-214.

[101] B. de Lacy Costello, R.J. Ewen, N.M. Ratcliffe, P.S. Sivanand, Thick film organic vapour sensors based on binary mixtures of metal oxides, Sensors Actuators B: Chem. 92 (2003) 159-166.

[102] Z. Yi, Y. BING, L. Chang, W. ZHENG, G. ZOU, Self-assembly of hierarchical $ZnSnO_3$-SnO_2 nanoflakes and their gas sensing properties, T NONFERR METAL SOC . 22 (2012) 2451-2458.

[103] D.R. Miller, S.A. Akbar, P.A. Morris, Nanoscale metal oxide-based heterojunctions for gas sensing: A review, Sensors Actuators B: Chem. 204 (2014) 250-272.

[104] D. Barreca, D. Bekermann, E. Comini, A. Devi, R.A. Fischer, A. Gasparotto, M. Gavagnin, C. Maccato, C. Sada, G. Sberveglieri, Plasma enhanced-CVD of undoped and fluorine-doped Co_3O_4 nanosystems for novel gas sensors, Sensors Actuators B: Chem. 160 (2011) 79-86.

[105] H. Jeong, H. Kim, P. Rai, J. Yoon, J. Lee, Cr-doped Co_3O_4 nanorods as chemiresistor for ultraselective monitoring of methyl benzene, Sensors Actuators B: Chem. 201 (2014) 482-489.

[106] N. Zhang, Q. Qin, X. Ma, J. Zhou, L. Sun, C. Chen, S. Wen, Y. Chen, S. Ruan, One-step synthesis and gas sensing properties of hierarchical Fe doped Co_3O_4 nanostructures, J. Alloys Compounds. 723 (2017) 779-786.

[107] R. Jin, Y. Jiang, L. Zhao, T. Wang, X. Liu, F. Liu, X. Yan, P. Sun, G. Lu, High sensitivity and low detection limit of acetone sensor based on Ru-doped Co_3O_4 flower-like hollow microspheres, Sensors Actuators B: Chem. 363 (2022) 131839.

[108] Z.S. Mehrabadi, A. Ahmadpour, N. Shahtahmasebi, M.B. Mohagheghi, Synthesis and characterization of Cu doped cobalt oxide nanocrystals as methane gas sensors, Phys. Scripta. 84 (2011) 015801.

[109] C.S. Jincy, P. Meena, Synthesis of Cu doped cobalt oxide nanoparticles as ammonia gas sensor operating at room temperature, Mater. Today: Proc. 43 (2021) 2459-2463.

[110] W. Yang, B. Fang, Y. Zhang, H. Meng, J. He, S. Liu, MOF-derived Mo-doped stacked Co_3O_4 nanosheets for chemiresistive toluene vapor sensing, Sensors Actuators B: Chem. 396 (2023) 134540.

[111] H. Sun, L. Liu, Metal-Organic frameworks-derived 2D spindle-like Sn-doped Co_3O_4 porous nanosheets as efficient materials for TEA detection, Sensors Actuators B: Chem. 338 (2021) 129825.

[112] P. Cheng, F. Dang, Y. Wang, J. Gao, L. Xu, C. Wang, L. Lv, X. Li, B. Zhang, B. Liu, Gas sensor towards n-butanol at low temperature detection: Hierarchical flower-like Ni-doped Co_3O_4 based on solvent-dependent synthesis, Sensors Actuators B: Chem. 328 (2021) 129028.

[113] S. Fareed, R. Medwal, J.V. Vas, I.A. Khan, R.S. Rawat, M.A. Rafiq, Tailoring oxygen sensing characteristics of Co_3O_4 nanostructures through Gd doping, Ceram. Int. 46 (2020) 9498-9506.

[114] X. Chen, S. Wang, C. Su, Y. Han, C. Zou, M. Zeng, N. Hu, Y. Su, Z. Zhou, Z. Yang, Two-dimensional Cd-doped porous Co_3O_4 nanosheets for enhanced room-temperature NO_2 sensing performance, Sensors Actuators B: Chem. 305 (2020) 127393.

[115] S. Park, S. Kim, H. Kheel, C. Lee, Oxidizing gas sensing properties of the n-ZnO/p-Co_3O_4 composite nanoparticle network sensor, Sensors Actuators B: Chem. 222 (2016) 1193-1200.

[116] F. Qu, J. Liu, Y. Wang, S. Wen, Y. Chen, X. Li, S. Ruan, Hierarchical Fe_3O_4@ Co_3O_4 core–shell microspheres: preparation and acetone sensing properties, Sensors Actuators B: Chem. 199 (2014) 346-353.

[117] S. Shi, F. Zhang, H. Lin, Q. Wang, E. Shi, F. Qu, Enhanced triethylamine-sensing properties of PN heterojunction Co_3O_4/In_2O_3 hollow microtubes derived from metal–organic frameworks, Sensors Actuators B: Chem. 262 (2018) 739-749.

[118] T.J. Theka, B.R. Thamaga, Z.P. Tshabalala, R.G. Motsoeneng, H.C. Swart, D.E. Motaung, Fabrication of metal-organic frameworks derived Co_3O_4 loaded on TiO2: Influence of Fe loading on the Co_3O_4/TiO_2 heterostructure for low-ppm benzene detection, Appl. Surf. Sci. 644 (2024) 158789.

[119] S. Bai, K. Tian, Y. Tian, J. Guo, Y. Feng, R. Luo, D. Li, A. Chen, C.C. Liu, Synthesis of Co_3O_4/TiO_2 composite by pyrolyzing ZIF-67 for detection of xylene, Appl. Surf. Sci. 435 (2018) 384-392.

[120] Y. Ji, N. Zhang, J. Xu, Q. Jin, X. San, X. Wang, Co_3O_4/In_2O_3 p-n heterostructures based gas sensor for efficient structure-driven trimethylamine detection, Ceram. Int. 49 (2023) 17354-17362.

[121] H. Wu, Y. Zhou, J. Guo, L. Zhao, T. Wang, X. Yan, C. Wang, F. Liu, P. Sun, G. Lu, Highly sensitive and selective xylene sensor based on pp heterojunctions composites derived from off-stoichiometric cobalt tungstate, Sensors Actuators B: Chem. 351 (2022) 130973.

[122] J. Zhang, K. Zhang, S. Liu, X. Liang, M. Zhang, Reasonable construction of 2D porous NiO/Co_3O_4 nanosheets for efficient detection of xylene, Sensors Actuators B: Chem. 377 (2023) 133002.

[123] K. Chen, J. Tsai, C. Chen, NiO functionalized Co_3O_4 hetero-nanocomposites with a novel apple-like architecture for CO gas sensing applications, Mater Lett. 255 (2019) 126508.

[124] R. Molavi, M.H. Sheikhi, Low temperature carbon monoxide gas sensor based on Ag-Co_3O_4 thick film nanocomposite, Mater Lett. 233 (2018) 74-77.

[125] W. Koo, S. Yu, S. Choi, J. Jang, J.Y. Cheong, I. Kim, Nanoscale PdO catalyst functionalized Co_3O_4 hollow nanocages using MOF templates for selective detection of acetone molecules in exhaled breath, ACS applied materials & interfaces. 9 (2017) 8201-8210.

[126] Z. Li, Y. Zhang, H. Zhang, J. Yi, MOF-derived Au-loaded Co_3O_4 porous hollow nanocages for acetone detection, Sensors Actuators B: Chem. 344 (2021) 130182.

[127] A. Ma, S.Y. Baek, J.H. Seo, S.A. Abbas, J. Kwon, S.J. Ahn, K.M. Nam, Photodeposition of Pt nanoparticles on Co_3O_4 nanocubes for detection of acetone at part-per-billion levels, ACS Appl. Nano Mater. 4 (2021) 2752-2759.

[128] V. Kruefu, U. Inpan, P. Leangtanom, C. Arkarvipath, P. Kongpark, D. Phokharatkul, A. Wisitsoraat, A. Tuantranont, S. Phanichphant, Enhanced Gas-Sensing Performances of Ru-Loaded p-Type Co_3O_4 Nanoparticles, physica status solidi (a). 215 (2018) 1701015.

[129] K.Y. Shin, A. Mirzaei, H.Y. Lee, J.H. Bang, W. Oum, E.B. Kim, H.M. Kim, S.M. Majhi, S.S. Kim, H.W. Kim, Formation of nanograined Ag-Co_3O_4 core@ shell structure to achieve enhanced xylene sensing characteristics, Sensors Actuators B: Chem. (2023) 134049.

[130] G. Yuan, Y. Zhong, Y. Chen, Q. Zhuo, X. Sun, Highly sensitive and fast-response ethanol sensing of porous Co_3O_4 hollow polyhedra via palladium reined spillover effect, RSC advances. 12 (2022) 6725-6731.

[131] J.H. Yue, L. Wang, J.C. Xu, H.X. Jin, B. Hong, D.F. Jin, J. Gong, X.L. Peng, H.L. Ge, X.Q. Wang, Highly improved toluene gas-sensing performance of mesoporous Ag-anchored cobalt oxides nanowires, Advanced Powder Technology. 33 (2022) 103832.

[132] M. Li, H. Zhu, G. Wei, A. He, Y. Liu, DFT calculation and analysis of the gas sensing mechanism of methoxy propanol on Ag decorated SnO_2 (110) surface, RSC advances. 9 (2019) 35862-35871.

[133] T.L. Gilbert, Hohenberg-Kohn theorem for nonlocal external potentials, Physical Review B. 12 (1975) 2111.

[134] W. Kohn, L.J. Sham, Self-consistent equations including exchange and correlation effects, Physical review. 140 (1965) A1133.

[135] E. Gross, W. Kohn, Local density-functional theory of frequency-dependent linear response, Phys. Rev. Lett. 55 (1985) 2850.

[136] R.O. Jones, O. Gunnarsson, The density functional formalism, its applications and prospects, Reviews of Modern Physics. 61 (1989) 689.

[137] J.P. Perdew, Y. Wang, Accurate and simple analytic representation of the electron-gas correlation energy, Physical review B. 45 (1992) 13244.

[138] J.P. Perdew, W. Yue, Accurate and simple density functional for the electronic exchange energy: Generalized gradient approximation, Physical review B. 33 (1986) 8800.

[139] K. Burke, J.P. Perdew, Y. Wang, Derivation of a generalized gradient approximation: The PW91 density functional, in: Anonymous Electronic Density Functional Theory: Recent Progress and New Directions, Springer, 1998, pp. 81-111.

[140] J.P. Perdew, K. Burke, M. Ernzerhof, Generalized gradient approximation made simple, Phys. Rev. Lett. 77 (1996) 3865.

[141] A.D. Becke, Density-functional exchange-energy approximation with correct asymptotic behavior, Physical review A. 38 (1988) 3098.

[142] C. Lee, W. Yang, R.G. Parr, Development of the Colle-Salvetti correlation-energy formula into a functional of the electron density, Physical review B. 37 (1988) 785.

[143] P. Pulay, S. Saebø, Orbital-invariant formulation and second-order gradient evaluation in Møller-Plesset perturbation theory, Theoretica chimica acta. 69 (1986) 357-368.

[144] L. Goerigk, S. Grimme, Double-hybrid density functionals, Wiley Interdisciplinary Reviews: Computational Molecular Science. 4 (2014) 576-600.

[145] M.A. Iqbal, N. Ashraf, W. Shahid, D. Afzal, F. Idrees, R. Ahmad, Fundamentals of Density Functional Theory: Recent Developments, Challenges and Future Horizons, Density Functional Theory-Recent Advances, New Perspectives and Applications. (2021).

[146] S. Li, C. Wang, Z. Lei, S. Sun, J. Gao, P. Cheng, H. Wang, Synergistic adsorption effect on Co_3O_4 (1 1 0) surface to promote the ethanol sensing properties: Experiment and theory, Appl. Surf. Sci. 612 (2023) 155776.

[147] W. Ji, Z. Shen, Q. Tang, B. Yang, M. Fan, A DFT study of Hg0 adsorption on Co_3O_4 (1 1 0) surface, Chem. Eng. J. 289 (2016) 349-355.

[148] Y. Feng, H. Zhang, P. Lu, X. Jia, Acetone Adsorption to Co_3O_4 (111)Surface: A Density Functional Theory (DFT) Study,.

Chapter 3

Methodology

3.1 Introduction

In this section our aim is to describe in detail the synthesis method and various characterization techniques used to investigate the structural, electronic, and optical properties of Co_3O_4 hierarchical structures. Experimentally, the hydrothermal synthesis method was employed to synthesize the Co_3O_4 nanostructures with subsequent calcination and characterized them using techniques including X-ray Diffraction (XRD), Transmission Electron Microscopy (TEM), Scanning Electron Microscopy (SEM), Brunauer-Emmett Teller (BET), X-ray photoelectron spectroscopy (XPS), Ultraviolet-visible spectroscopy (UV-vis) and Photoluminescence (PL). Computationally, Density Functional Theory calculations were employed using Material Studio of Biovia for enhanced comprehension of the interaction between target gas molecules and the nanostructures. Furthermore, the chapter discusses the experimental setup and procedures used for gas sensing tests, including variations in working temperatures and concentrations of gases.

3.2 Synthesis procedure: Hydrothermal method

Any homogeneous or heterogeneous chemical reaction carried out at high temperatures and pressures inside sealed containers utilizing water, where the reactants can dissolve but the products produced are insoluble, is known as a hydrothermal process [1]. With this method, nanomaterials are formed at various temperatures, from room temperature to very high temperatures. The morphology of the nanomaterials can be modified depending on the vapor pressure of the mixture in the reaction. From the literature, it can be understood that varying the hydrothermal experimental conditions such as temperature and reaction time can alter the properties of the Co_3O_4 nanomaterials. From a gas sensing perspective, these changes in material characteristics such as crystallinity and morphology have a paramount influence on gas sensing performance. In this work, using the hydrothermal method, Co_3O_4 nanosheets were successfully synthesized following the procedure in **Figure 3.1.**

3.2.1 Synthesis of the pristine Co_3O_4 structures

Urea ($CO(NH_2)_2$), and cobalt nitrate hexahydrate ($Co(NO_3)_2$ 6 H_2O) were used as starting materials without further purification. Firstly, 0.84 g of urea was dissolved in 70 ml of distilled water, then 2.037 g of Co ($NO_3)_2$ 6 H_2O, was added under magnetic stirring for 5 minutes. The solution was then transferred into a double-walled Teflon vessel and kept in an oven at 140 °C for 6, 12, and 24 hours. The resultants were collected via centrifugation, washed with distilled water and ethanol, and then dried in the oven at 60 °C for 24 hours. The resulting products were further calcined at 600 °C for 2 hours at a 3°/h heating rate. Black powders were obtained as final products and they were labelled as Co_3O_4_6 hrs, Co_3O_4_12 hrs, and Co_3O_4_24 hrs, for 6-, 12-, and 24-hours oven duration, respectively.

3.2.2 Synthesis of the Zn-/Sn-doped Co_3O_4 structures

Urea ($CO(NH_2)_2$), cobalt nitrate hexahydrate ($Co(NO_3)_2{\cdot}6H_2O$), Zinc nitrate hexahydrate ($Zn(NO3)_2{\cdot}6H_2O$) and tin(II) chloride dihydrate ($SnCl_2{\cdot}2H_2O$) were used as starting materials without further purification. For **Zn- doped Co_3O_4 structures**, 0.84 g of urea was dissolved in 70 ml of distilled water, then 2.037 g of Co ($NO_3)_2{\cdot}6H_2O$ and 0.364, 0.728 and 1.460 g of $Zn(NO3)_2{\cdot}6H_2O$ were sequentially added in 3 different conical flask under magnetic stirring for 5 minutes. The solutions were then transferred into a double-walled Teflon vessel and kept in an oven at 140 °C for 6 hours. The resultants were collected via centrifugation, washed with distilled water and ethanol, and then dried in the vacuum oven at 60 °C for 24 hours. The resulting products were further calcined at 600 °C for 2 hours at a 3°/h heating rate. Black powders were obtained as final products and they were labelled as 0.5Zn-Co_3O_4, 1.0Zn-Co_3O_4 , and 2.0Zn-Co_3O_4, for 0.364, 0.728, and 1.460 g of $Zn(NO3)_2{\cdot}6H_2O$ respectively. For **Sn-doped Co_3O_4 structures**, 0.84 g of urea was dissolved in 70 ml of distilled water, then 2.037 g of $Co(NO_3)_2{\cdot}6H_2O$ and 0.364, 0.728 and 1.460 g of $SnCl_2{\cdot}2H_2O$ were sequentially added in 3 different conical flask under magnetic stirring for 5 minutes. The solutions were then transferred into a double-walled Teflon vessel and kept in an oven at 140 °C for 6 hours. The resultants were collected via centrifugation, washed with distilled water and ethanol, and then dried in the oven at 60 °C for 24 hours. The resulting products were further calcined at 600 °C for 2 hours at a 3°/h heating rate. Black powders were obtained as final products and they were labelled as 0.5Sn-Co_3O_4, 1.0Sn-Co_3O_4, and 2.0Sn-Co_3O_4, for 0.364, 0.728, and 1.460 g of $SnCl_2{\cdot}2H_2O$ respectively.

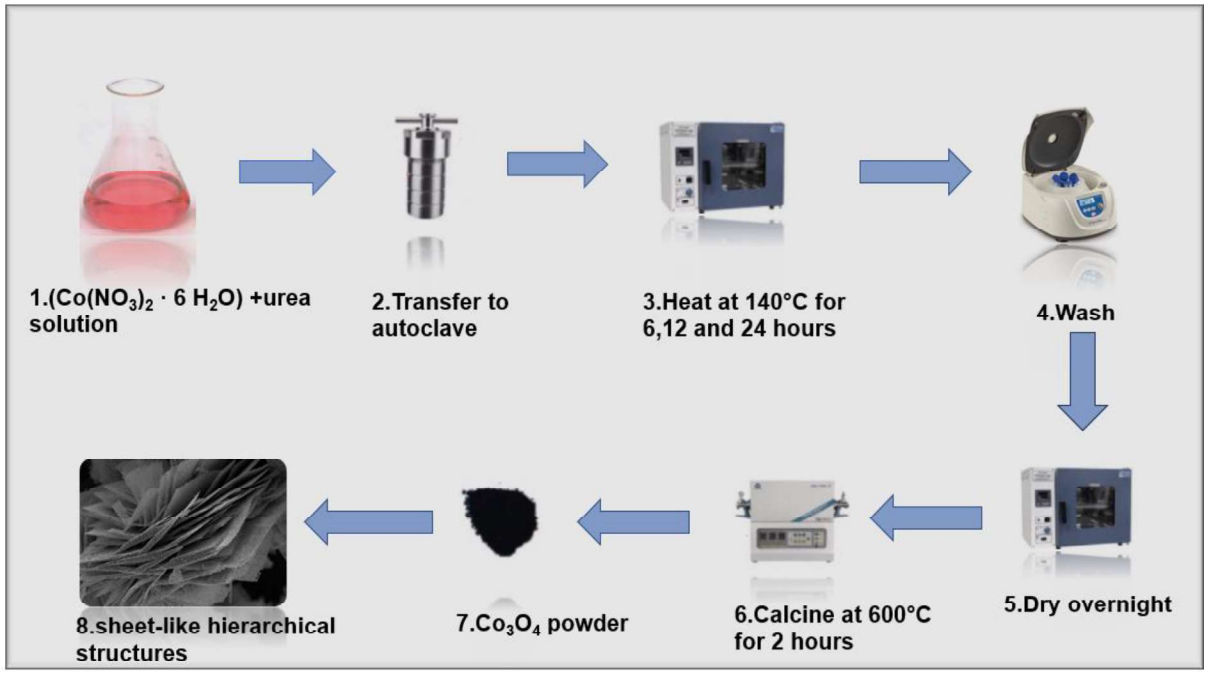

Figure 3. 1: Schematic illustration of the hydrothermal synthesis of Co_3O_4 sheet-like structures.

3.3 Characterization

3.3.1 X-ray diffraction (XRD)

X-ray diffraction is an adaptable characterization technique used to analyse the structure of fabricated materials [2]. The working principle is dependent on the possible interference of monochromatic X-rays of a distinct wavelength with the sample, Cathode ray tubes induce the X-rays as illustrated in **Figure 3.2.** to produce electrons and accelerate them in the direction of the target using a voltage and bombard it to produce characteristic X-ray spectra, including K_α and K_β components. Cu, Fe, Mo, and Cr are examples of the target materials that help control these spectra components. Copper (Cu) target material with CuKα radiation is the one that is mostly used for single-crystal emission. To achieve monochromatic X-rays for diffraction, the use of filters through foils or crystal monochrometers is necessary. The X-rays are then aimed at the sample, and the constructive interference takes place when the sample and detector rotate, and the incident X-ray geometry satisfies the phenomenal law called Bragg's law [3]:

$$n\lambda = 2d\sin\theta \qquad (3.1)$$

where "*n*" is an integer, λ is the x-ray's wavelength, *d* is a vector presenting the displacement that generates the diffraction, and Θ is the angle of diffraction. The importance of this law is to link the electromagnetic radiation wavelength with the angle of diffraction and the displacement in a crystal. The resulting intensity peaks are then detected by a detector and turned into a count rate as results to a computer monitor. In this work, powder X-ray diffraction (XRD) Panalytical X'pert PRO PW3040/60 X-ray diffractometer was used with a Cu-Kα1 (λ=1.5406 Å) radiation.

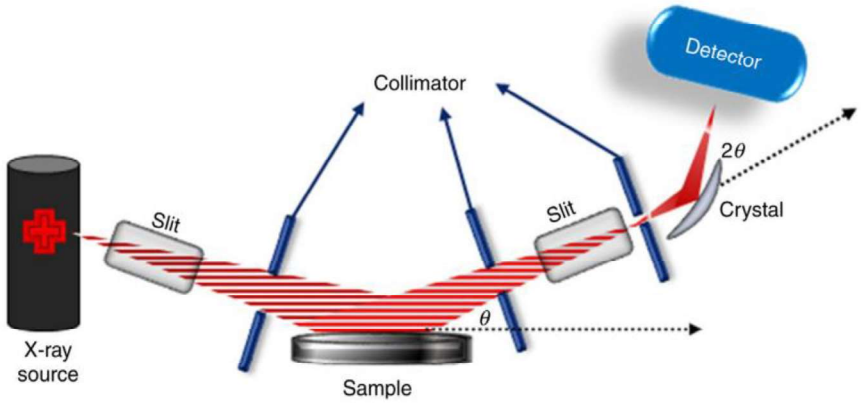

Figure 3. 2: Schematic illustration of X-ray diffraction [4].

3.3.2 Scanning electron microscopy (SEM)

The scanning electron microscope is a non-toxic instrument used as a characterization technique by simply scanning the surface of the material to determine the morphology and the chemical mixture properties of the sample analyzed [5]. The instrument uses an electron beam to scan the sample, electrons are produced by the electron gun, and then accelerated and attracted by the anode. This electron gun is sealed with a special chamber to maintain the vacuum and protect it from any destruction or contamination. The importance of the vacuum is that it offers the privilege of obtaining high-resolution images to the user, it also results in an increment efficiency collection of electrons through the detectors control the movement and direction of the electrons, electromagnetic lenses are in used Electromagnetic lenses are used to control the direction of electrons, together with apertures to dictate the size of the beam. The manner in which these electrons interact inside the sample generates different types of electrons such as backscattered and secondary electrons.

Both of the electrons result from inelastic and elastic interactions of the beam and the sample respectively and they convey different information on the display of the images and also detailed facts about the surface of the material detectors are used to detect BSEs and SEs [6], which then output the 3D image of

the sample on the computer depicted in **Figure 3.3.** In this work, the morphology of the products were characterized by a ZEIS-AURIGA field emission scanning electron microscopy (FESEM) at an accelerating voltage of 3kV.

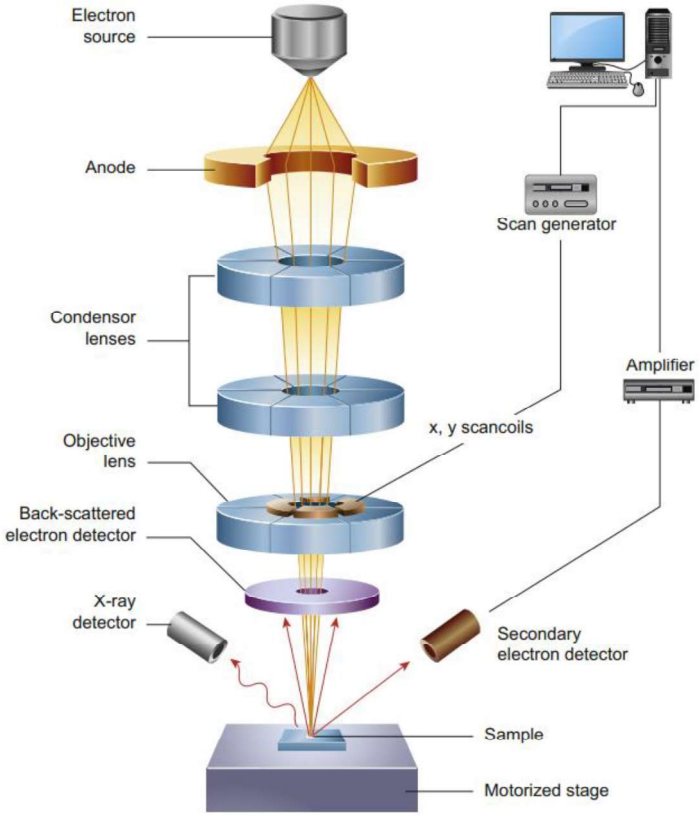

Figure 3. 3: Schematic illustration of Scanning Electron Microscopy [5].

3.3.3 Transmission electron microscopy (TEM)

Transmission electron microscopy (TEM) is a powerful characterization instrument used to investigate the internal structure of the sample providing important information such as the materials's composition, imperfections, and growth layers at the nanoscale through the transmission of a high-voltage beam of electrons [7]. **Figure 3.4** shows the schematic illustration on TEM. The working concept of TEM is that an electron gun (source) produces electrons that travel through the vacuum tube. Just like SEM electromagnetic lenses control the movement of these electrons into a thin beam transmitted through the specimen. Rotating the sample and capturing images at each rotation allows the creation of a 3D representation (tomography).

For crystalline materials, electron diffraction helps analyse the crystal structure, through the interaction of electrons within the sample, X-ray emission can be detected through an energy-dispersive spectrometer that is embedded within TEM. The spectra obtained help identify the constituent elements [7]. JEOL TEM-2100 high-resolution transmission electron microscopy (HR-TEM) with an accelerating voltage of 200 kV was used in this work.

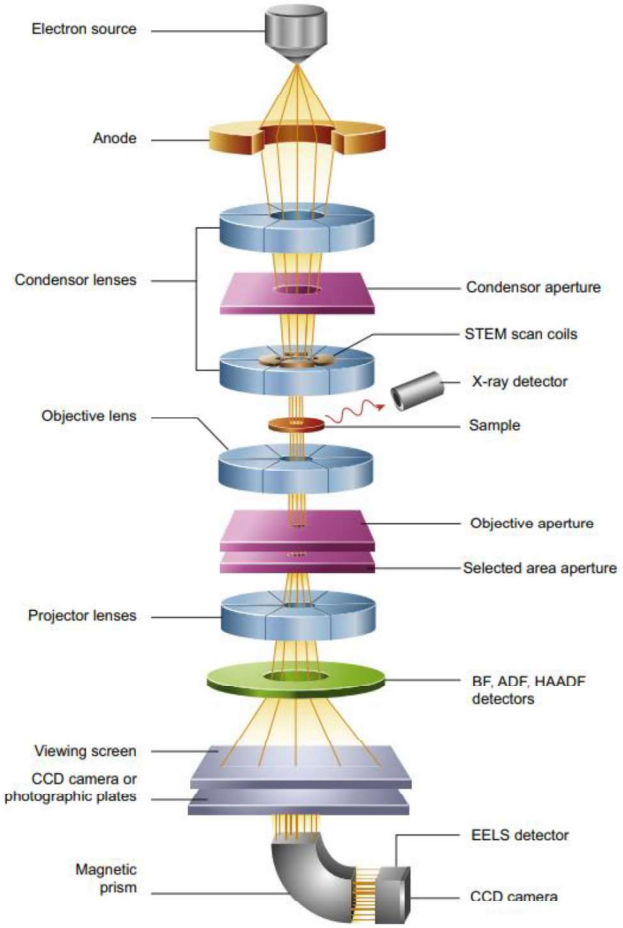

Figure 3. 4: Schematic illustration of Transmission Electron Microscopy [5].

3.3.4 Brunauer-Emmett Teller (BET)

Brunauer-Emmett-Teller (BET) is a characterization tool used for measuring the surface area of the sample [8]. The working principle of this technique is based on the physical surface assimilation of the inert gas molecules on the material. **Figure 3.5 (a)** shows the BET apparatus and **Figure 3.5 (b)** shows the volumetric method apparatus which illustrate the determination of surface area. Out of all inert gases, nitrogen (N_2) is mostly used due to its excessive purity and vigorous interaction with solid materials.

Since gaseous and solid phase interactions are weak, liquid N_2 is used to cool down the surface to achieve exposable proportions of the interactions of gas molecules onto the surface of the material. Amounts of N_2 gas are released into the materials cells, relative pressures are then fabricated by forming a conditional partial vacuum which is less than atmospheric pressure, when the pressure is balanced adsorptions do not further occur. Transducers are used to control the pressure fluctuations caused by adsorption, after the adsorption layers are formed, the sample is transferred out of the N_2 environment followed by heating treatment for the adsorbed N_2 to liberate from the material and gauged. The data collected is displayed in the form of a BET isotherm [9]. In this work, N_2 adsorption-desorption isotherms were acquired at 77 K using a Micrometirics TRISTAR 300 surface area analyser.

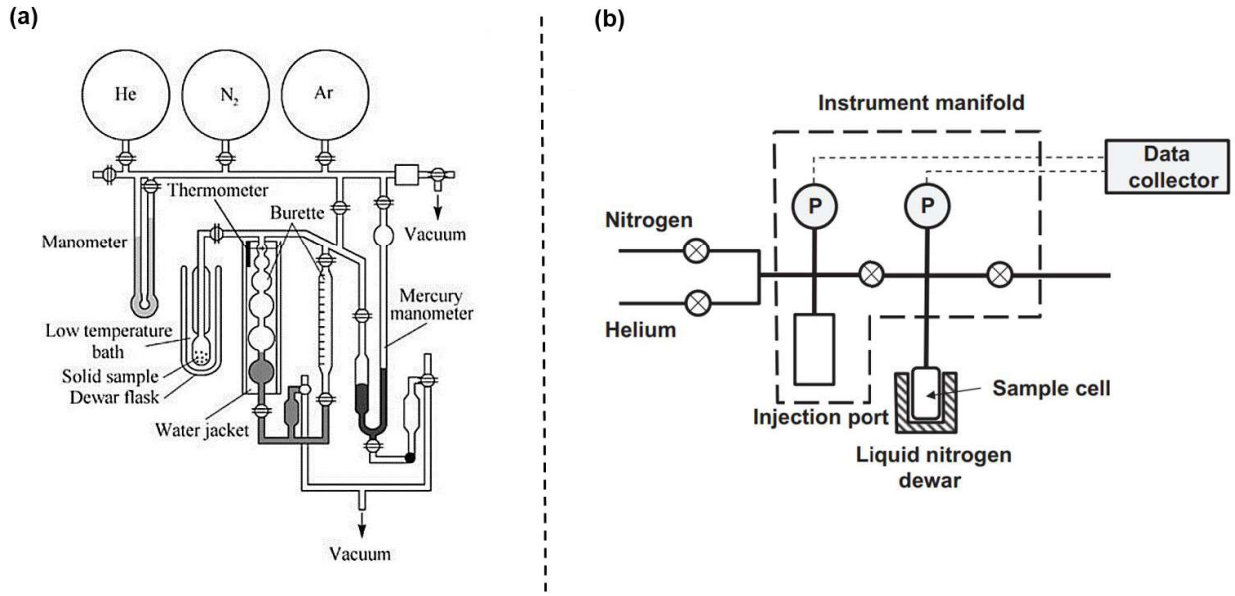

Figure 3. 5: (a) Schematic illustration of BET apparatus for specific surface area determination [10] and (b) schematic illustration of volumetric method apparatus [9].

3.3.5 UV-visible spectroscopy (UV-Vis)

UV-visible spectroscopy (UV-Vis) is a versatile characterization technique that helps probe the visual properties of the materials by gauging the amount of visible and UV light absorbed by the sample [11]. On the electromagnetic spectrum, the wavelength of the UV and Visible regions falls in the range of 200 – 900 nm. This basic working principle involves the emission of light source mostly provided by deuterium lamps and halogen lamps. The light output is then directed to the diffraction grating and goes through the entrance slit as a one-color beam, it is transmitted through a sample and then the remaining light is detected by a detector such as a photodetector. The detector is used to gauge the strength of the

transmitted light and turn the light into a current signal that is interpreted by a computer as illustrated in **Figure 3.6.** The absorbance spectrum is obtained when the intensity of the transmitted light is compared with the reference by the instrument. The law that satisfies this observation is Beer-Lambert Law [10]:

$$A = \varepsilon l c m \tag{3.2}$$

where A is absorbance, ε is the molar absorptivity, l is the light path length, and c is the concentration.

In this work, optical properties were analyzed using a Varian Cary 500 UV-Vis NIR spectrophotometer equipped with a Praying Mantis Diffuse Reflectance Accessory from Harrick Scientific Products.

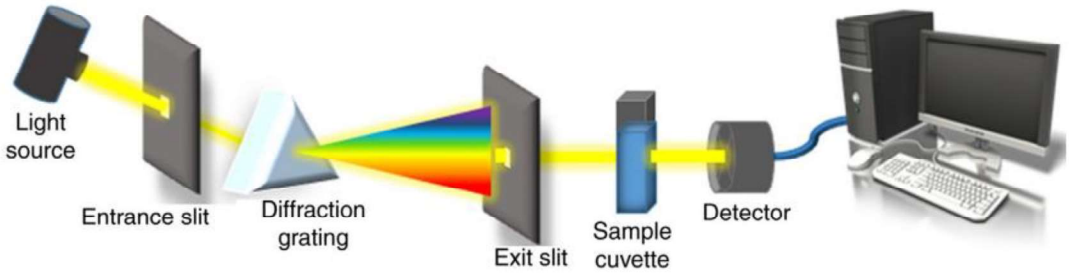

Figure 3. 6: Schematic illustration of UV-vis spectrophotometer [4].

3.3.6 Photoluminescence (PL)

Photoluminescence (PL) is a characterization technique used to measure the purity and crystalline quality of materials, and also to determine the band gap, exciton lifetime, exciton energy, bi-exciton, etc [12].**Figure 3.7 (a)** illustrate the bloc diagram of how the PL instrument works, just like UV-vis, the working principle requires an external light source, in this case, lasers with high- energy are used, and the light output gets absorbed through the impartation of the energy that is excess to the sample through a phenomenon called photo-excitation. The sample releases the excess energy through light emission, during photo-excitation the electrons of the material occupy the excited states and then return to their equilibrium state (ground states) by dissipation of extra energy through radiative and non-radiative processes shown in **Figure 3.7 (b).** The produced light is connected to the energy between excited and ground states. In the form of spectra of wavelengths generated, they are then utilized to help identify various atoms and molecules and to discover chemical structures. In this work, Horiba QuantaMaster QM8000 spectrofluorometer with a Xenon (Xe) source and a 325 nm fast pulsed laser source were used to determine PL characteristics.

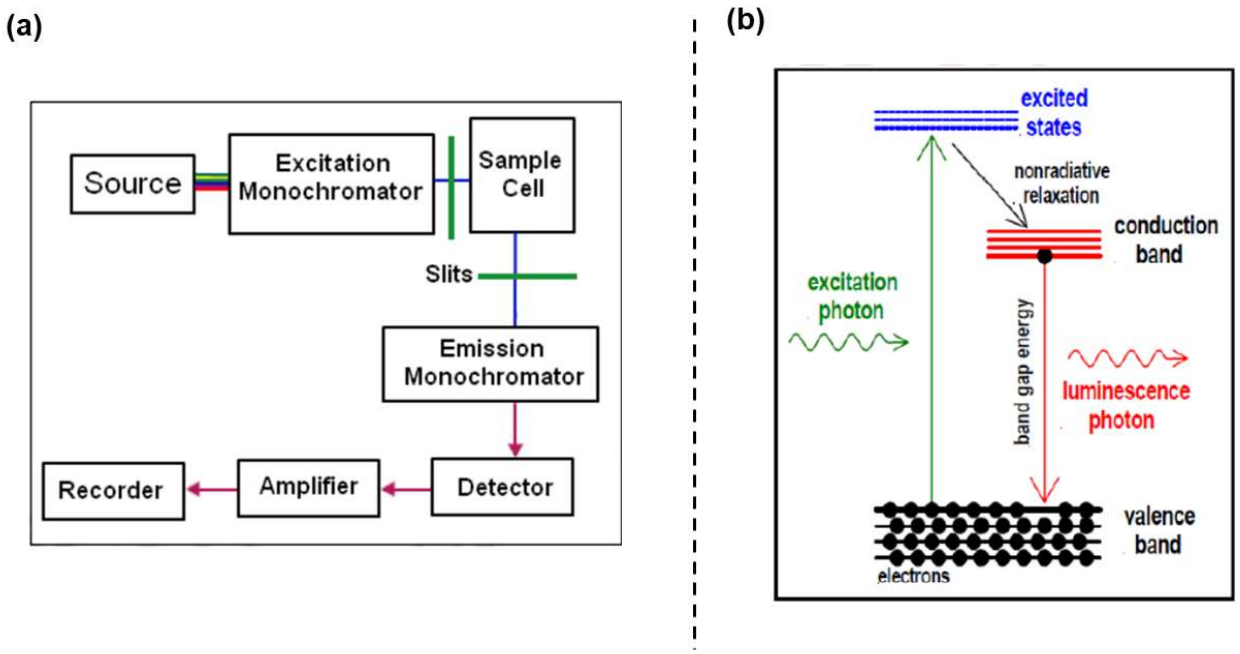

Figure 3. 7: (a) Schematic illustration of **photoluminescence (PL)** spectrometer block diagram [13] and (b) principle of PL [13].

3.3.7 X-ray photoelectron spectroscopy (XPS)

X-ray photoelectron spectroscopy (XPS) is a very powerful characterization technique, suitable to characterize the contributing elemental compositions together with the chemical states within a material [14]. **Figure 3.8** describes the instrument's working principle that is based on the photoelectric effect phenomenon. Using the photon source, the electrons are generated in a vacuum environment onto the sample, penetrating only about 1-10 nm. The electrons are then ejected from the sample then collected by the detectors. The variance between the energy of the photon, kinetic energy, and the work function describes the electron binding energy which is then translated into understandable information. The electron binding energy is characteristic of the elements, it is also affected by factors such as the oxidation state, identification of the neighbouring atoms, and hybridization of the atoms. In this work, X-ray photoelectron spectra (XPS) were obtained with a PHI 5000 Versaprobe X-ray photoelectron with monochromatic Al-Kα radiation ($h\nu$ =1486.6 eV).

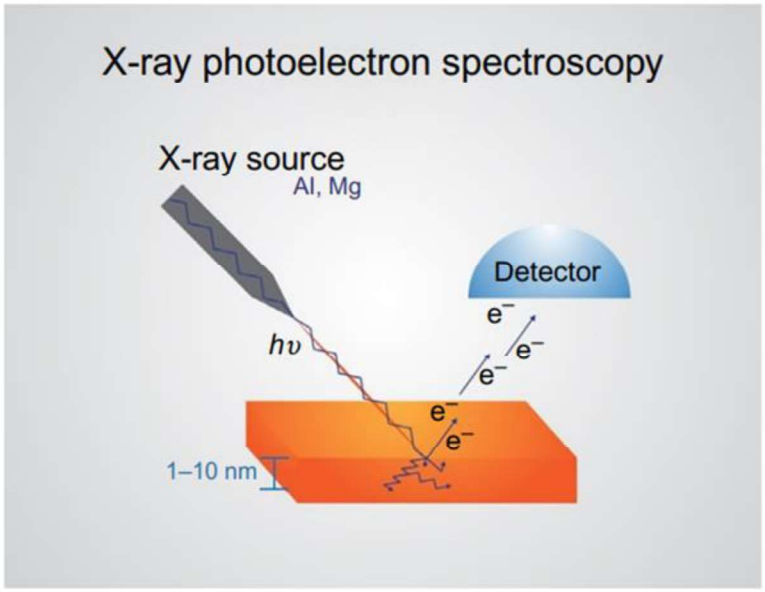

Figure 3. 8: Schematic illustration of X-ray photoelectron spectrometer [14].

3.4 Gas sensing measurements

3.4.1 Sensor fabrication and measurements

Figure 3.9 depicts the Co_3O_4 sensors fabrication process. Ethyl cellulose in turpineol solution was added to the Co_3O_4 powders to form thixotropic pastes, which were then pasted onto substrates made up of alumina with interdigitated platinum (Pt) electrodes on the sensor part and a heater to control the working temperature.

Computer-controlled KSGGAS 6S (Kenosistec) testing station was used to obtain the sensing measurements. To have control over the working temperatures of the sensors the heating voltage was modified, and a thermocouple was used to measure the resulting temperature to match with the temperatures from room temperature to 200 °C. Specific concentrations of various test gases were diversified at the flow rate ratios of methane (CH_4), carbon monoxide (CO), ethylene (C_2H_4), ethanol (C_2H_5OH), acetone (C_3H_6O), and benzene (C_6H_6). Sensing measurements in the humid environment were measured by introducing the desired concentration of the target gas balanced with wet air (30-90% relative humidity (RH) set at 50°C) at the set operating temperature. The electrical resistance of the sensor was measured in air (Ra) and the presence of the target gas (Rg) using a Keithley 6487 Picoammeter/voltage source meter. The response was determined as:

$$R = \frac{Rg}{Ra} \tag{3.3}$$

whereby R_g is the resistance of the sensor in gas, and R_a is the resistance of the sensor in air [15].

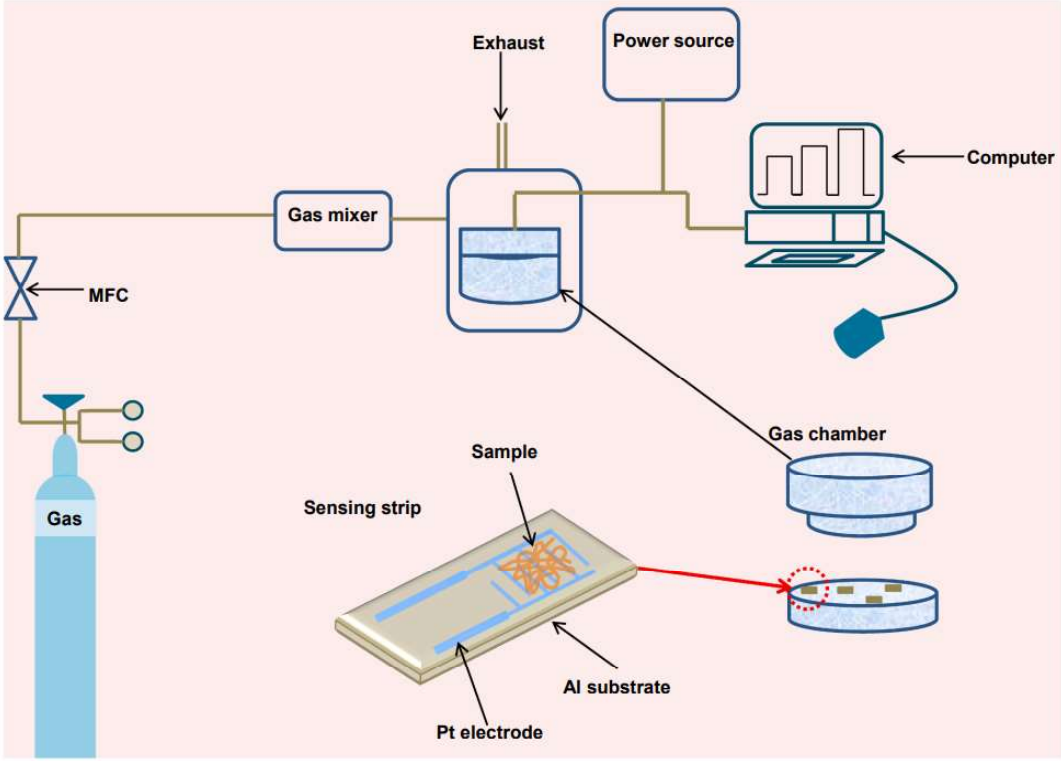

Figure 3. 9: Schematic illustration of the setup for the sensing measurement [16].

3.5 Computational method

Density functional theory (DFT) is a well-established research tool that relates and connects theory and experiments that result in important interpretations of various properties being studied [17]. Using the application Material Studio of Biovia, DFT simulations were ran with the Cambridge Serial Total Energy Package (CASTEP) code as illustrated in **Figure 3.10.** In the calculation, the exchange-correlation effects were described by the ultra-soft pseudopotential of the on-the fly-generated (OTFG) and the generalized gradient approximation (GGA) together with formation suggested by Perdew–Burke–Ernzerhof (PBE) for optimized calculations [18]. For optimizations of the bulk and surface geometry, Monkhorst-Pack k point mesh of 2× 7 × 2 and cut-off energy for the expansion of the plane waves of 550 eV were used [19]. The surface model with the $Co_{34}O_{36}$ cell formulation was created from the optimized bulk structure of the Co_3O_4 crystal with a group space of F-43m and lattice parameters of a = b = c =8.065000 Å (α = β =γ =90°) and modeled as p (2×2x1) slab. To describe the reaction of gas molecules with the surface,

the gas molecule was placed at position 1.990 Å above the surface. To find the adsorption energy the following expression was used [20]:

$$E_{ads} = E_{mol-surf} - E_{surf} - E_{mol} \quad (3.4)$$

Where $E_{mol\text{-}surf}$ is the total energy of the gas molecule being adsorbed on the surface of the material, E_{surf}, and E_{mol} are the energy of the material surface and the gas molecule, respectively.

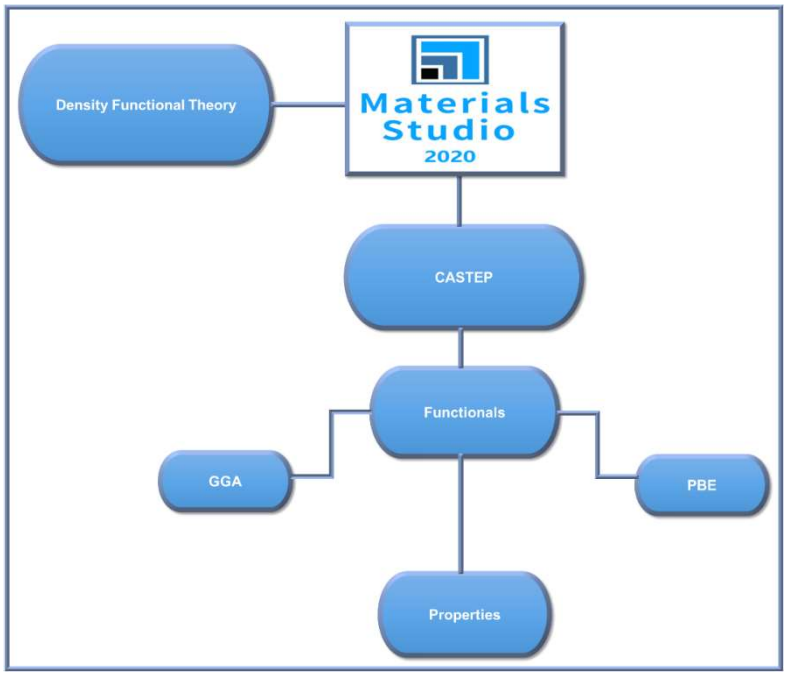

Figure 3. 10: Schematic illustration of the computational method.

3.6 References

[1] M. Yoshimura, K. Byrappa, Hydrothermal processing of materials: past, present and future, J. Mater. Sci. 43 (2008) 2085-2103.

[2] M. Ermrich, D. Opper, XRD for the analyst, Getting acquainted with the principles. Second. Panalytical. (2013).

[3] A.A. Bunaciu, E.G. UdriŞTioiu, H.Y. Aboul-Enein, X-ray diffraction: instrumentation and applications, Crit. Rev. Anal. Chem. 45 (2015) 289-299.

[4] M. Gumustas, C.T. Sengel-Turk, A. Gumustas, S.A. Ozkan, B. Uslu, Effect of polymer-based nanoparticles on the assay of antimicrobial drug delivery systems, in: Anonymous Multifunctional Systems for Combined Delivery, Biosensing and Diagnostics, Elsevier, 2017, pp. 67-108.

[5] B.J. Inkson, Scanning electron microscopy (SEM) and transmission electron microscopy (TEM) for materials characterization, in: Anonymous Materials Characterization using Nondestructive Evaluation (NDE) Methods, Elsevier, 2016, pp. 17-43.

[6] W. Zhou, R. Apkarian, Z.L. Wang, D. Joy, Fundamentals of scanning electron microscopy (SEM), Scanning Microscopy for Nanotechnology: Techniques and Applications. (2007) 1-40.

[7] F. Mokobi, Scanning Electron Microscope (SEM)—definition, principle, parts, images, Microbe Notes. (2021).

[8] N. Hwang, A.R. Barron, BET surface area analysis of nanoparticles, The connexions project. (2011) 1-11.

[9] S. Yurdakal, C. Garlisi, L. Özcan, M. Bellardita, G. Palmisano, (Photo) catalyst characterization techniques: adsorption isotherms and BET, SEM, FTIR, UV–Vis, photoluminescence, and electrochemical characterizations, in: Anonymous Heterogeneous Photocatalysis, Elsevier, 2019, pp. 87-152.

[10] O.D. Neikov, D.V. Lotsko, V.G. Gopienko, Powder characterization and testing, Handbook of non-ferrous metal powders. (2009) 3-62.

[11] M. Picollo, M. Aceto, T. Vitorino, UV-Vis spectroscopy, Physical sciences reviews. 4 (2018) 20180008.

[12] S. Konde, J. Ornik, J.A. Prume, J. Taiber, M. Koch, Exploring the potential of photoluminescence spectroscopy in combination with Nile Red staining for microplastic detection, Mar. Pollut. Bull. 159 (2020) 111475.

[13] I. Zafirovska, M.K. Juhl, J.W. Weber, O. Kunz, T. Trupke, Module inspection using line scanning photoluminescence imaging, (2016) 1826-1829.

[14] Y. L'H, L.K. Mireles, X-ray photoelectron spectroscopy (XPS) and time-of-flight secondary ion mass spectrometry (ToF SIMS), in: Anonymous Characterization of Polymeric Biomaterials, Elsevier, 2017, pp. 83-97.

[15] K. Shingange, H.C. Swart, G.H. Mhlongo, Enhanced ethanol sensing abilities of fiber-like $La_{1-x}Ce_xCoO_3(0 \leq x \leq 0.2)$ perovskites based-sensors at low operating temperatures, Sensors Actuators B: Chem. 377 (2023) 133012.

[16] K. Shingange, H.C. Swart, G.H. Mhlongo, $LaBO_3$ (B= Fe, Co) nanofibers and their structural, luminescence and gas sensing characteristics, Physica B Condens. 578 (2020) 411883.

[17] M. Orio, D.A. Pantazis, F. Neese, Density functional theory, Photosynthesis Res. 102 (2009) 443-453.

[18] J.P. Perdew, K. Burke, M. Ernzerhof, Generalized gradient approximation made simple, Phys. Rev. Lett. 77 (1996) 3865.

[19] H.J. Monkhorst, J.D. Pack, Special points for Brillouin-zone integrations, Phys. Rev. B. 13 (1976) 5188.

[20] Y. Qin, Z. Ye, DFT study on interaction of NO_2 with the vacancy-defected WO_3 nanowires for gas-sensing, Sensors Actuators B: Chem. 222 (2016) 499-507.

Chapter 4

Fabrication, characterization, and gas detection performance of Co_3O_4 sheet-like hierarchical structures

4.1 Introduction

Herein the fabrication of three samples consisting of Co_3O_4 sheet-like hierarchical structures using the hydrothermal method detailed in Chapter 3, section 3.2.1 is reported. The microstructural properties of the Co_3O_4 sheet-like hierarchical structures such as crystallinity, surface area, and defects are studied in relation to the gas sensing performance of the individual sensors towards C_2H_4.

4.2 Results

4.2.1 Structural analysis

The phase purity and crystal structure of the obtained Co_3O_4 products were examined using XRD and the resulting patterns are shown in **Figure 4.1(a).** The patterns revealed the Bragg reflections which can be indexed to Co_3O_4 (JCPDS card no. 42-1467) [1], respectively. Sharp peaks in the XRD pattern were observed indicating that the obtained products are highly crystalline. Other peaks due to crystallographic impurities were not observed. A noticeable shift in the position of the diffraction peaks was noticed and this shift can be demonstrated in **Figure 4.1(b)** using the (311) diffraction peak. This shift in peak position could be due to several factors such as changes in the lattice parameters, lattice strain, or defects within the crystal structure [2,3].

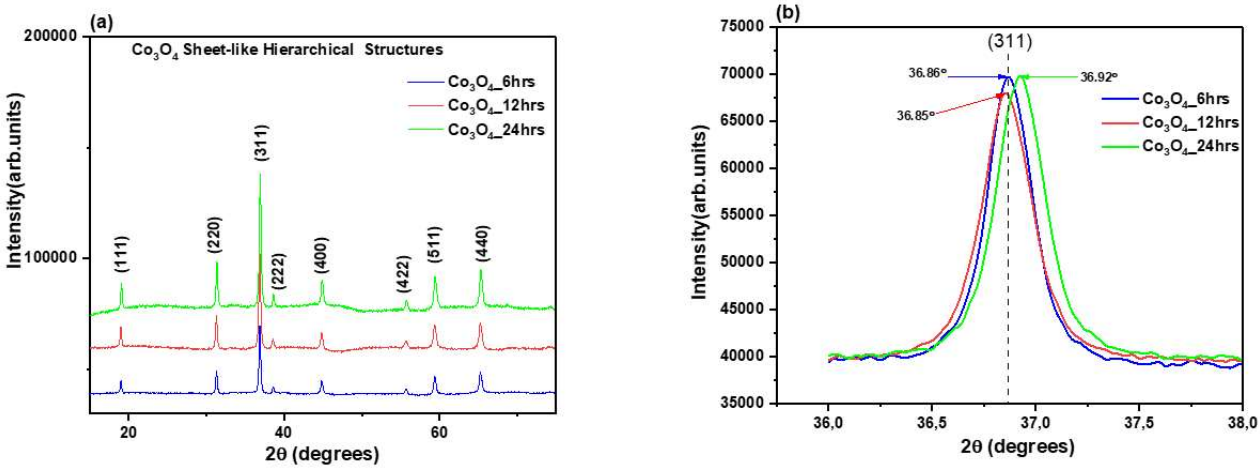

Figure 4. 1: (a) XRD patterns and (b) enlarged (311) diffraction peak of the Co_3O_4 sheet-like structures.

The crystallite size (D) of the products was determined using the Debye-Scherrer formula [4] and the values were found to be 33, 31, and 31 nm for Co_3O_4_6 hrs, Co_3O_4_12 hrs, and Co_3O_4_24 hrs, respectively. It was observed that crystallite size decreased with increasing oven duration. These results indicate that the mechanism for nucleation and small crystal growth is governed by organizing Co_3O_4 clusters composing the Co_3O_4 crystalline structure. Once formed, the crystallites grow to a range appropriate for the formation of a small Co_3O_4 single crystal. Thereafter, these small single crystals undergo a process of aggregation to form a polycrystalline particle. The longer oven durations might lead to increased aggregation of particles, causing the appearance of smaller crystallite sizes. This can be due to particle interactions, such as coalescence or aggregation, which might result in larger apparent particle sizes.

4.2.2 Morphological analysis (SEM and TEM)

Figure 4.2 (a-c) depicts the SEM images of the Co_3O_4_6 hrs, Co_3O_4_12 hrs, and Co_3O_4_24 hrs products. The products exhibited a sheet-like morphology assembling to form a hierarchical structure. A closer look at the structures (see **Figure 4.2 (d-f))** revealed particles with an average size of 82, 109, and 115 nm for Co_3O_4_6hrs, Co_3O_4_12 hrs, and Co_3O_4_24 hrs joining together to form these sheet-like structures. The joining of the particles leaves pores in between the particles thus making the sheet-like structures porous. The porous nature of the hierarchical structure is advantageous for gas sensing as it provides gas diffusion channels which allows for more access to active sites during the gas sensing process**. Figure 4.2 (g-i)** depicts the TEM images confirming the sheet-like structures, with interlinked particles forming

the porous sheets. Further, HR-TEM images depicted in **Figure 4.2 (j-l)** revealed lattice fringes with d-spacing of 0.24, 0.28, and 0.46 nm corresponding to (311), (220), and (111) planes of Co_3O_4, respectively confirming the XRD results.

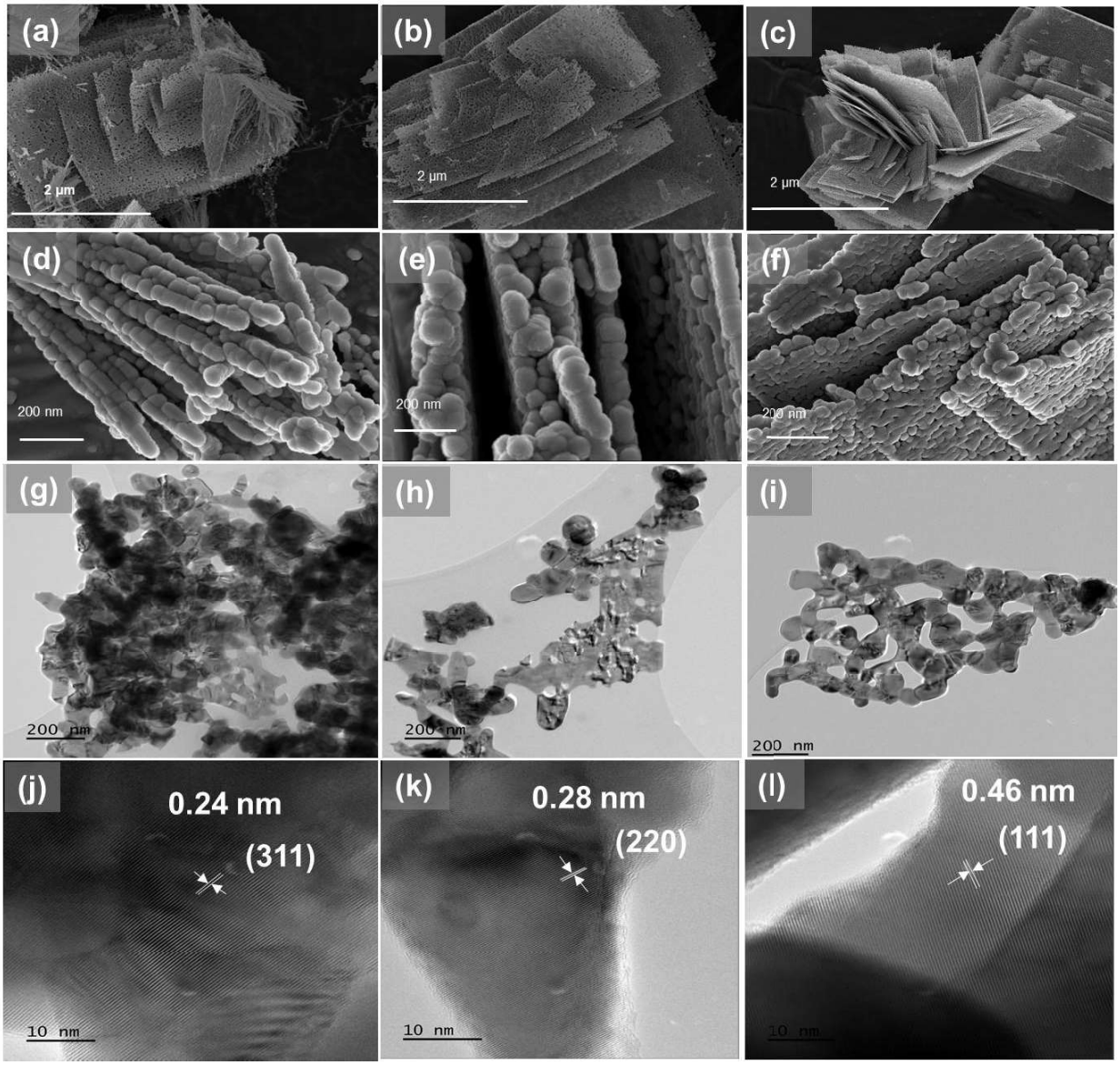

Figure 4. 2: SEM, TEM, and HR-TEM images of the Co_3O_4 sheet-like structures obtained at (a, d, g, and j) 6 hours, (b, e, h, and k) 12 hours, and (c, f, I and l) 24 hours.

4.2.3 Surface area analysis

Gas sensing is a surface phenomenon, and that makes the surface area of the material an important aspect of gas sensing. Surface area helps facilitate gas diffusion and increase the sensitivity of the material to different gases by providing active sites for gas adsorption [5]. To establish the surface area of the Co_3O_4 nanostructures BET measurements were performed and the resulting isotherms are provided in **Figure**

4.3(a-c). The N2 isotherms are type IV with an H3 hysteresis loop at high pressures (P/Po > 1), which is indicative of the presence of a mesoporous structure [6]. The surface area of the sheet-like hierarchical structures decreased with increasing reaction time with values of 10.5967, 8.0869, and 7.4215 m^2/g for Co_3O_4_6hrs, Co_3O_4_12hrs and Co_3O_4_24hrs, respectively. This observation could be due to agglomeration resulting from extended reaction times. The closer packing arrangement of agglomerated particles tends to result in a lower exposed surface area because of the effective surface sharing amongst aggregates of particles [7]. The possible reactions involved in the growth of the Co_3O_4 sheet-like structures can be summarized as:

$$CoNO_3 \rightarrow Co^{2+} + 2NO^{-1} \quad (4.1)$$

$$(H_2N)_2CO + H_2O \rightarrow 2NH_3 + CO_2 \quad (4.2)$$

$$NH_3 + H_2O \rightarrow NH_4^+ + OH^- \quad (4.3)$$

$$Co^{2+} + 2OH^- \rightarrow Co(OH)_2 \quad (4.4)$$

cobalt hydroxide ($Co(OH)_2$) was then calcined in air at 600 °C to form Co_3O_4 through the reaction between air oxygen and ($Co(OH)_2$) during the calcining process. Eq. (4.3) plays an important role in the growth process, which can be influenced by the reaction time [8]. It might be expected that applying more reaction time evolves the sheet-like morphology, but the morphology was maintained at an even longer reaction time. However, the size of the interlinked particles that form the sheet-like structures revealed an increasing trend with increasing reaction time, which can be attributed to Oswald ripening [9]. Small particles have a larger surface area-to-volume ratio, which makes them more soluble than larger particles. As a result, small particles dissolve and redeposit onto larger particles, resulting in a size increase of the larger particles. Ostwald ripening can have a significant impact on the properties of materials, in this instance, Oswald ripening has led to the formation of larger particles that reduced the surface area of the sheet-like structures. This signifies that the hydrothermal reaction time plays an important role in the effective growth of nanostructures.

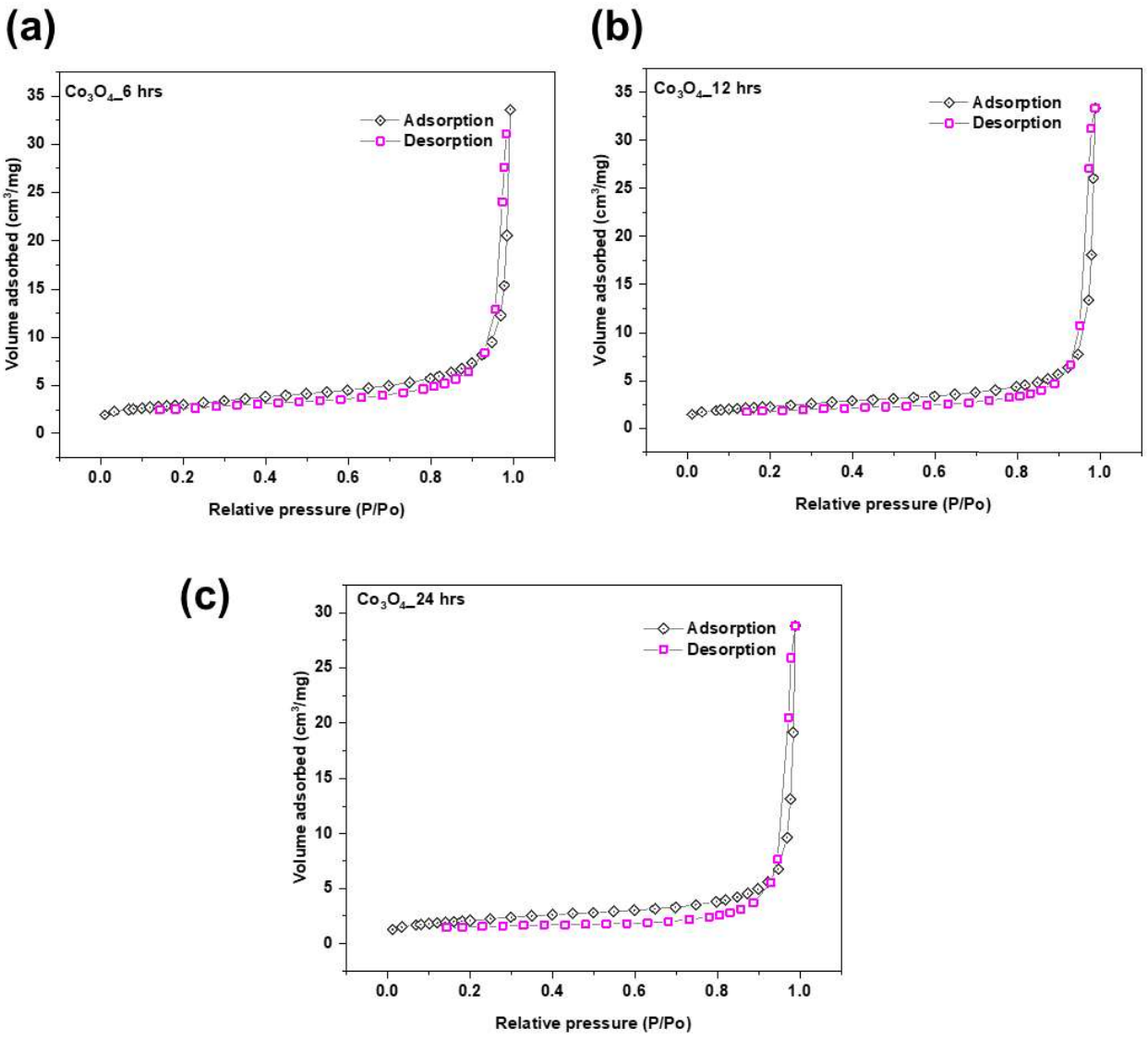

Figure 4. 3: Nitrogen adsorption-desorption isotherms for the (a) Co_3O_4_6 hr, (b) Co_3O_4_12 hr, and (c) Co_3O_4_24 hr sheet-like structures.

4.2.4 Optical properties (UV-Vis and PL)

4.2.4.1 UV-Vis

Absorption spectral analysis is the most common technique used to confirm the nanoparticles formation. The absorption spectra of Co_3O_4 Sheets-like structures obtained at 6,12 and 24 hours are shown in **Figure 4.4.** The optical properties of nanomaterials are dependent on the quantum confinement, which in turn is controlled by the grain size and the defects present in them. In a typical UV–Vis spectrum of Co_3O_4, the

transitions are present as per the ligand field theory, and the peak positions are often affected by the morphology, size, and defects [10], There are two absorption bands in the Visible-light region, approximately at 410-450 nm and 600-660 nm. This is because of the ligand-to-metal charge transfer O→Co events [11].

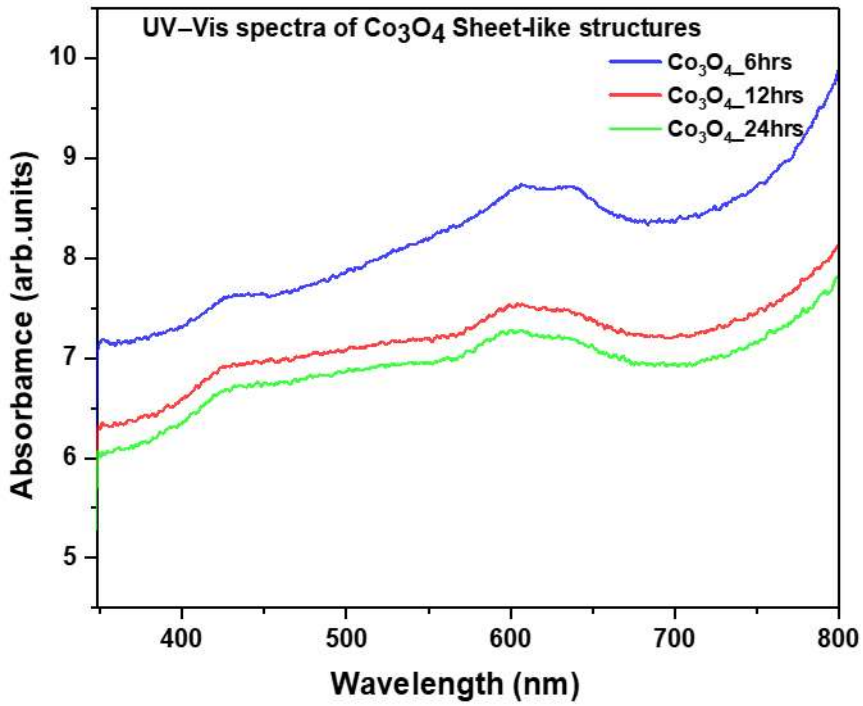

Figure 4. 4: UV–Vis spectra of Co_3O_4 sheet-like structures obtained at different reaction times.

Meanwhile, the band gaps (E_g) of the samples, calculated by using the Tauc plot method [12], are depicted in **Figure 4.5.** Co_3O_4 sheet-like structures at 6, 12, and 24 hours exhibit band gaps of 1.67, 1.53, and 1.65 eV, which correspond to O^2 (2p)→Co^{3+} and O^{2-}(2p)→Co^{2+} transitions, respectively [12,13].

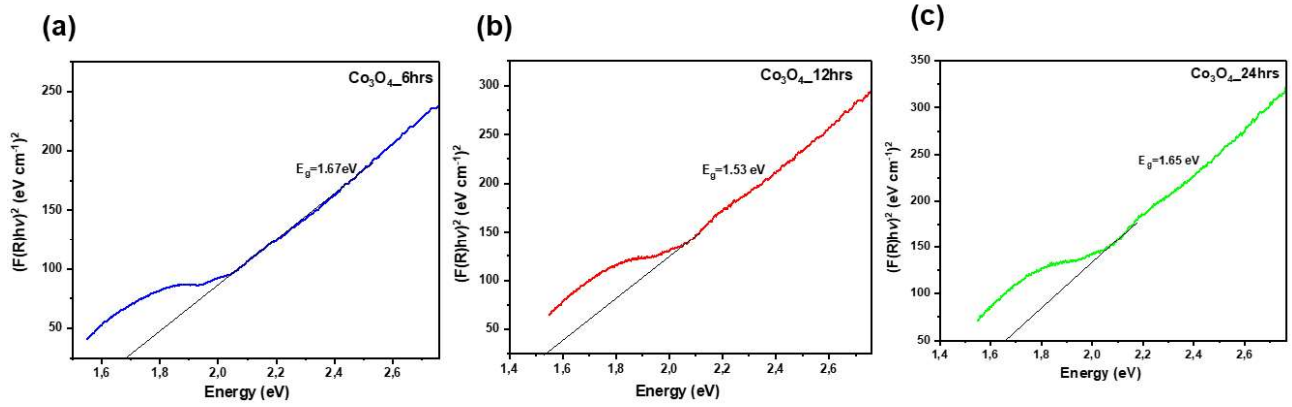

Figure 4. 5: Plots of $(\alpha h\nu)^2$ versus hν demonstrating the band energy of Co_3O_4_6 hr, Co_3O_4_12 hrand Co_3O_4_24 hr nanostructures.

4.2.4.2 Photoluminescence

The presence, type, and density of defects in Co_3O_4 hierarchical structures can be manipulated through synthesis conditions and post-processing treatments. Understanding the influence of defects on the gas sensing behavior of Co_3O_4 is crucial for engineering materials with optimal gas detection capabilities. To examine the properties of the defects for the Co_3O_4 sheet-like hierarchical structures, PL studies were performed at room temperature using an excitation wavelength of 325 nm, and the resulting spectra are shown in **Figure 4.6(a).** As observed from the spectra, a broad emission band in the visible region depicted between 380-600 nm was observed. The presence of defects in the material can create meta-stable energy levels in the band gap, leading to a broadening of the emission spectrum [14]. The intensity of the emission band was observed to be higher for Co_3O_4_6hrs and decreased with a further increase in reaction time (Co_3O_4_12 hrs and Co_3O_4_ 24hrs). The decline in the emission intensity is an indication of the reduction in the recombination rate of electron-hole pairs. The determination of PL spectra is thought to be sensitive to the surface morphology and state of the synthesized nanostructures [15]. It should be noted that in this case, the reaction time during the synthesis process has a prominent effect on the intensity of the emission band. Further, the difference in emission intensity can be attributed to the size distribution of the particles and the presence of defects (metal and/or oxygen vacancies and/or interstitials) [4]. To gain a detailed understanding of the origin of the broad emission, the deconvoluted PL spectra are displayed in **Figure 4.6(b).** Six peaks have been fitted at 3.2 eV (387 nm), 3.00 eV (413 nm), 2.8 eV (437 nm), 2.7 eV (460 nm), 2.5 eV (496 nm) and 2.3 eV (539 nm). The near ultraviolet region peak centered at 387 nm (3.2 eV) is assigned to electrons and holes recombination in the edge conduction and valence bands [16]. The violet emission at 413 nm (3.00 eV) can be attributed to the transition of trapped electrons at the cobalt interstitial valence band [17]. The blue emissions at 437and 460 nm (2.84 and 2.70 eV) are assigned transition from the Co_i to cobalt vacancy (V_{Co}) or from Co_i to the top of the valence band or from the extended Co_i to the top of the valence band [18]. The green emission at 496 and 539 nm (2.50 and 2.30 eV) are associated with the recombination of oxygen vacancy V_O to V_{Co} or the recombination of the electrons in the singly ionized oxygen vacancy V_{O^+} in the photo-excited holes in the valence band [18]. Since the intensity of Co_3O_4_6 hrs sheet-like hierarchical structures is higher than the Co_3O_4_12 hrs and Co_3O_4_ 24hrs, this suggests that Co_3O_4_6 hrs sheet-like hierarchical structures have the highest defects, particularly more oxygen vacancies which are advantageous to the adsorption of more oxygen molecules on the surface of the material, so gas sensing performance will be improved [19]. The reduction in the quantity of defects with increasing reaction time can be attributed to the reduction of surface area with increasing reaction time, as a larger surface area has been reported to result in an enhanced density of defects [20]. Therefore, Co_3O_4_12hrs and Co_3O_4_24hrs have reduced

quantity of defects due to their lower surface area as compared to Co_3O_4_6hrs. These results justify that by varying the reaction time during the synthesis of Co_3O_4 nanostructures, the defects properties can be tuned [32][21].

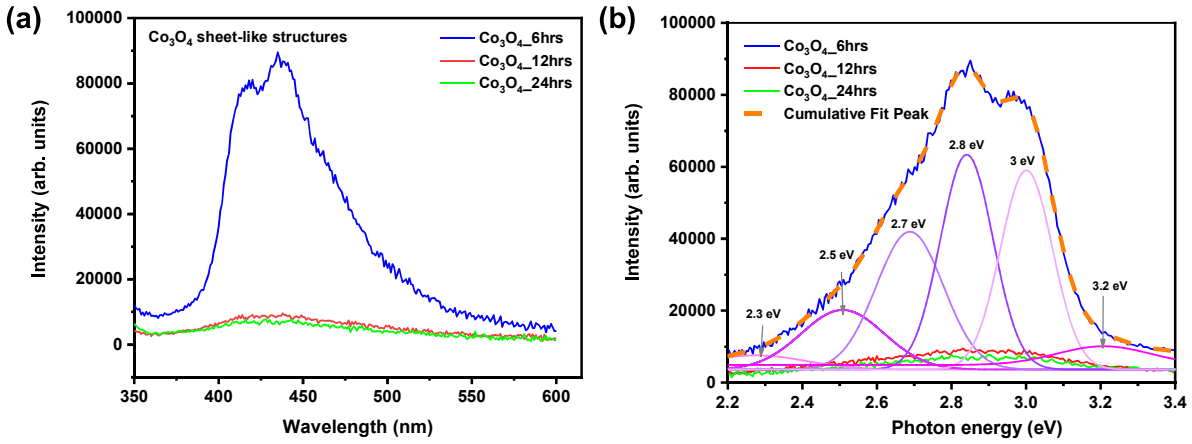

Figure 4. 6: (a) PL spectra and (b) deconvoluted PL spectra of the Co_3O_4 sheet-like hierarchical structures.

4.2.5 Gas sensing performance

The sensor operating temperature is a fundamental factor that significantly impacts the practicality of gas sensors in real-world applications as it influences the sensitivity, selectivity, and the processes of gas adsorption and desorption on the surface of the material. Operating the sensor at the appropriate temperature ensures that these processes are happening optimally, leading to accurate and reliable gas detection [21]. Therefore, to determine the temperature dependence behaviour of the Co_3O_4 sheet-like based sensors, the sensors were exposed to 100 ppm of C_2H_4 at various temperatures ranging from RT to 200 °C. **Figure 4.7** displays the response of the Co_3O_4 sheet-like sensors as a function of temperature. The response of the sensors is observed to be low at RT and then increased with increasing temperature until a maximum response was reached. Further increase in temperature resulted in the decline of the response for all sensors. SMO based sensors normally need thermal activation energy to operate, so the sensors have a low response at low operating temperatures due to the limited thermal activation energy available, nevertheless, at higher temperatures, the response is decreased due to reduced target gas molecule adsorption [22,23]. Co_3O_4_6 hrs reached a maximum response of response 49.6 at 100 °C, and Co_3O_4_12 hrs and Co_3O_4_24 hrs-based sensors reached a maximum response of 21.6 and 16 at 120 °C, respectively. The Co_3O_4_6 hrs-based sensor revealed the highest response at all the temperatures as compared to Co_3O_4_12 hrs and Co_3O_4_24-based sensors, with the highest response at 100 °C. As a result, all gas sensing measurements were performed at an optimal operating temperature of 100 °C.

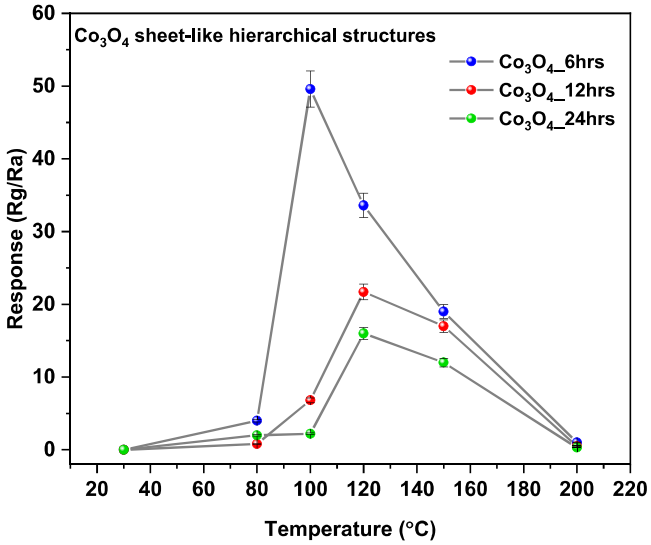

Figure 4. 7: Operating temperature determination for the Co_3O_4 sheet-like hierarchical structures-based sensors using 100 ppm C_2H_4.

Figure 4.8(a, c, and e) displays the transient resistance response curves of the Co_3O_4 sheet-like hierarchical structures-based sensors towards 5 to 100 ppm gas concentration of C_2H_4 at an optimal operating temperature of 100 °C. The sensor resistance increased quickly upon the introduction of C_2H_4 and then gradually saturated until C_2H_4 was withdrawn and proceeded slowly to recovery/baseline, demonstrating reversibility characteristics. It was also noticed that the sensor resistance increased with increasing C_2H_4 concentration. This can be because the more gas molecules exposed on the surface of the sensors, the more adsorption sites are covered, thus increasing the responsiveness of the sensors. Further notice, the resistance of the sensors suffered from baseline drift with the Co_3O_4_24hrs-based sensor showing greater drift in comparison to sensors based on Co_3O_4_6hrs and Co_3O_4_12hrs. Normally for gas sensors, the baseline drift could be attributed to several factors such as a slowly changing environment and other instability factors (structure transformation, phase transformation, poisoning, degradation of contacts and heaters, bulk diffusion, errors in design, change of humidity, fluctuations of temperature in the surrounding atmosphere, and interference effect) and prolonged high-temperature operation [24-26]. In this study, we can base the contributing effect on the materials characteristics to be able to interact with C_2H_4 at the specific conditions which are highly dependent on the reaction time.

Apart from sensitivity or response, the performance evaluation of gas sensors also considers response-recovery time. Response time refers to the duration it takes for the sensor to reach 90% of its equilibrium

resistance value after being exposed to the target gas. Conversely, recovery time is the time it takes for the sensor's resistance to return to 10% below its initial resistance after the gas has been removed. These factors play a vital role in assessing the sensor's capability to detect and quantify specific gases promptly and accurately. The response-recovery characteristics of the sensors towards 100 ppm of C_2H_4 are shown in **Figure 4.8(b, d, and f).** The estimated response time was found to be 27, 142, and 147 s, whereas the recovery time was estimated as 42, 210, and 197 s for Co_3O_4_6hrs, Co_3O_4_12hrs, and Co_3O_4_24hrs, respectively. Noticeably, the analysis revealed that the Co_3O_4_12hrs and Co_3O_4_24hrs sheet-like hierarchical structures-based sensors exhibited longer response and recovery times compared to the Co_3O_4_6hrs based sensor which demonstrated swift response and recovery.

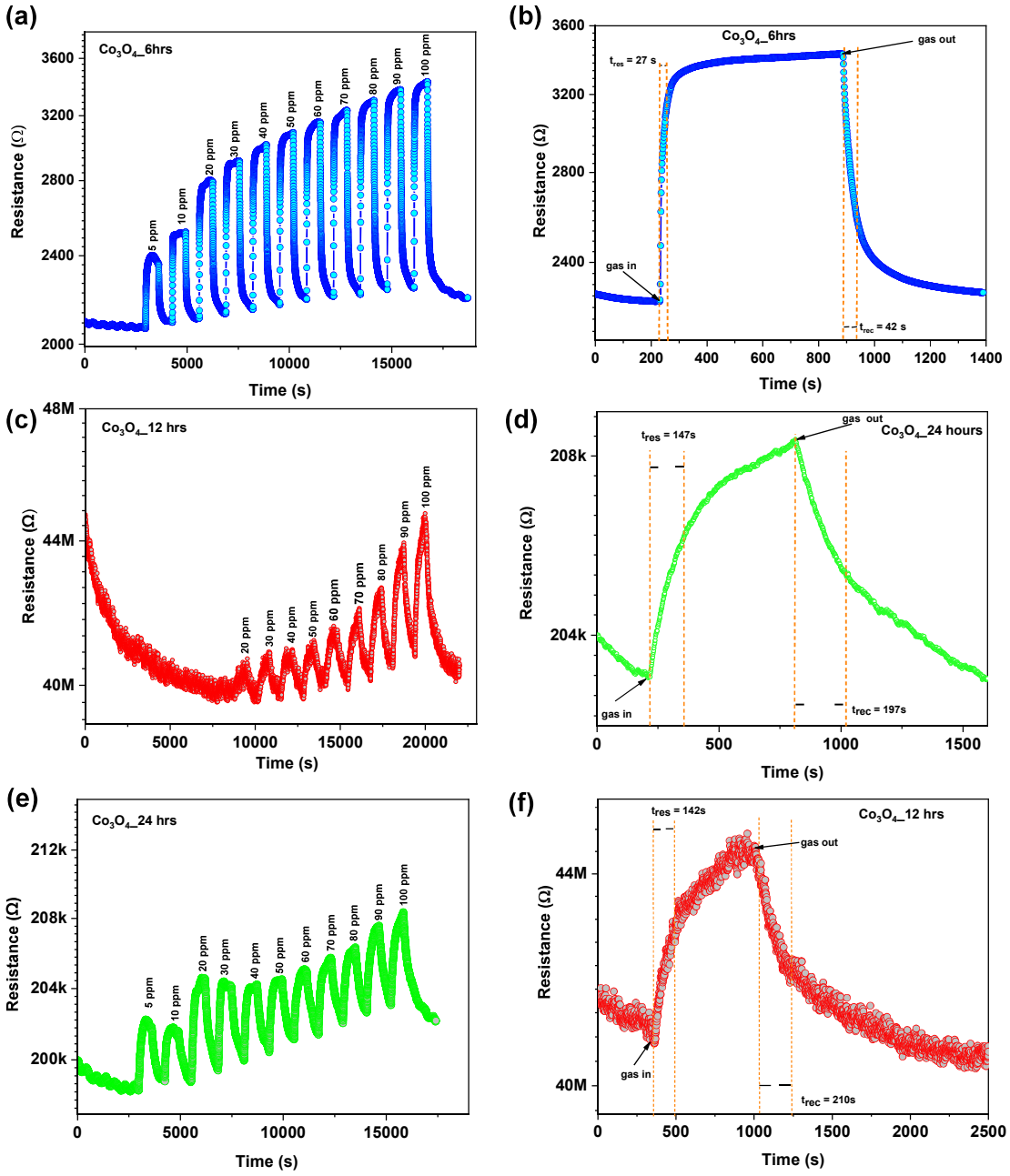

Figure 4. 8: (a, c, e) Transient resistance response and (b, d, f) response-recovery time at 100 ppm C_2H_4 of the Co_3O_4 sheet-like structures-based sensors at 100 °C.

The chemical makeup of the material, dimensions, growth direction, operating temperature, and reactivity of the sensing gas all influence how selective a sensor is. So, to determine the selectivity of the Co_3O_4 sheet-like hierarchical structures, a selectivity study at 100 °C with 100 ppm of several gases namely CH_4, CO, C_3H_6O, C_2H_5OH and C_6H_6 was conducted as shown in **Figure 4.9.** Interestingly, the Co_3O_4_6hrs based sensor revealed high selectivity to C_2H_4, the Co_3O_4_12 hrs-based sensor showed high

response to C_2H_5OH and Co_3O_4_24 hrs demonstrated high response towards C_6H_6 at 100 °C, respectively. The observed selectivity to various gases per sensor may be due to the sensing material's surface activation energy matching the target gas's lowest unoccupied molecular orbital energy level, low dipole moment, and low activation energy. Also, the varying selectivity of the sensors could have to do with the operating temperature, indicating that the sensor's surface strongly reacts with the target gas they are responding high to in comparison to the other gases [27]. Nonetheless, the highest response was obtained by the Co_3O_4_6hrs based sensor towards 100 ppm C_2H_4 gas with the highest response of 49.6.

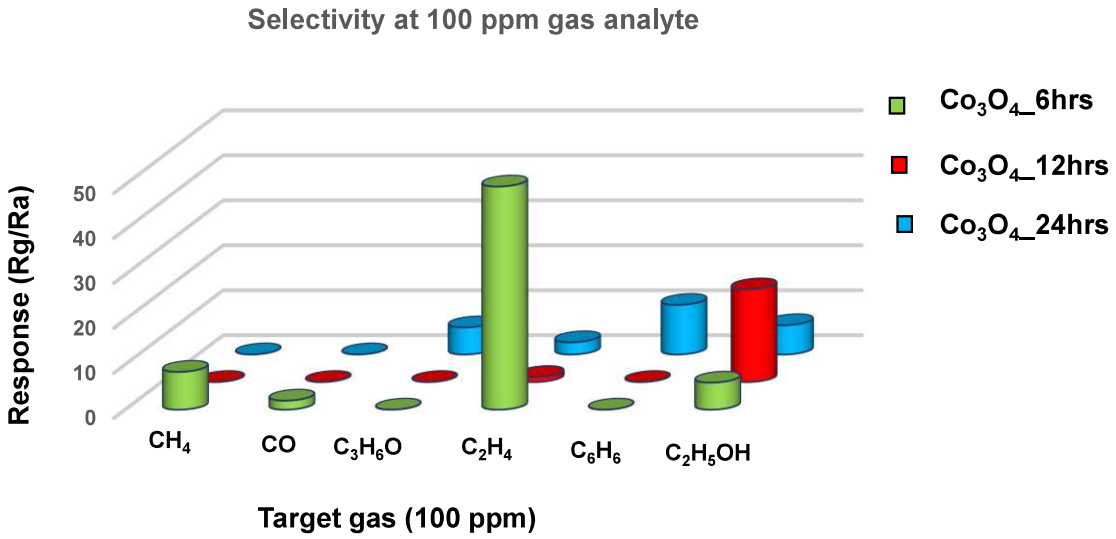

Figure 4. 9: Responses towards 100 ppm of different gases of Co_3O_4 sheet-like hierarchical structures at 100 °C.

It is also important for the sensor to be able to produce the same output readings when the same gas is detected multiple times under identical conditions, this property is called repeatability. The sensor's repeatability was evaluated by subjecting the Co_3O_4_6hrs-based sensor to five cycles of 10 ppm C_2H_4 gas at 100 °C and the resulting cycles are shown in **Figure 4.10(a).** Excellent resistance consistency of the Co_3O_4_6hrs-based sensor towards 10 ppm C_2H_4 was observed, demonstrating the reliability of the Co_3O_4_6hrs-based gas sensor. The first cycle of the sensor has a slightly different appearance from the subsequent cycles; this may be due to the conditioning/stabilization process, which involves exposing the Co_3O_4_6hrs-based sensor to a C_2H_4 to stabilize. This can affect the sensor's sensitivity, resulting in a different response cycle from the following cycles [28].

Further, humidity continues to be one of the most important factors in determining the full detection capability of the sensor. Therefore, the relative humidity (RH) of the Co_3O_4_6hrs-based gas sensor varied from 30%, 60%, and 90% at an operating temperature of 100 °C. As shown in **Figure 4.10(b),** the

response declines with increasing RH, which is due to water molecules occupying the adsorption sites of C_2H_4 on the surface of the Co_3O_4, thus the response of the sensors decreases [29].

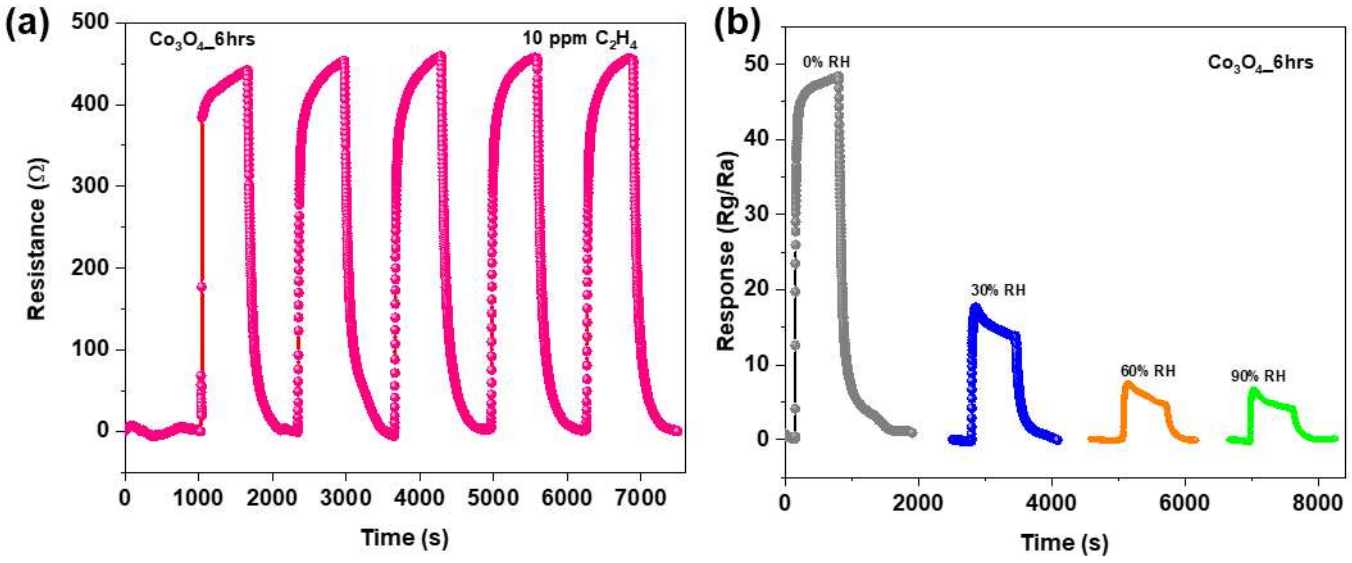

Figure 4. 10: (a) Response repeatability of the Co_3O_4_6hrs-based sensor towards 10 ppm and (b) Relative humidity influence on the response of Co_3O_4_6hrs based-sensor towards 100 ppm C_4H_4 at 100 ºC.

4.3 Gas sensing mechanism

Gas sensing is a surface phenomenon that depends on many factors, such as morphology, surface area, quantity of defects, etc. Generally, large surface area and abundant defects particularly oxygen vacancies are beneficial to gas sensing properties. By comparison of the morphology of Co_3O_4_6hrs, Co_3O_4_12hrs, and Co_3O_4_24hrs, it was established that all three products exhibited a sheet-like morphology assembling to form a hierarchical structure with interconnected particles. However, gas sensing performance towards C_2H_4 still varied despite the similar morphology. This indicates that the morphology does not play a key role in the gas sensing performance in this study.

In this study, it was observed from the BET N_2 isotherms that the surface area of Co_3O_4_6hrs is larger than that of Co_3O_4_12hrs and Co_3O_4_24hrs. The surface areas were measured to be 10.5967, 8.0869, and 7.4215 m^2/g, for Co_3O_4_6hrs, Co_3O_4_12hrs, and Co_3O_4_24hrs, respectively. The surface area of Co_3O_4_6hrs is larger than Co_3O_4_12hrs and Co_3O_4_24hrs. Consequently, gas performance for C_2H_4 gas

of the Co_3O_4_6hrs based sensor is higher than that of Co_3O_4_12hrs and Co_3O_4_24hrs based sensors. This indicates that the specific surface area plays a key role in the gas performance in this study.

Further, it was observed from the PL spectra that the PL intensity of the Co_3O_4_6hrs is higher than that of Co_3O_4_12hrs and Co_3O_4_24hrs. PL intensity and defect concentration in a material can be related, but this relationship is complex and depends on several factors. The density of defects is one of the factors that can influence PL intensity, but other material properties, reaction time, and the specific type of defects involved can also play a role. Deconvolution of the PL spectra revealed the origin of the defects which included Co_i, V_{Co} and V_O. The sensor based on Co_3O_4_6hrs showed better C_2H_4 performance in comparison to sensors based on Co_3O_4_12hrs and Co_3O_4_24hrs. This indicates that the gas sensing performance in this study is influenced by the number of structural defects.

The gas sensing mechanism of SMO based sensors takes place on the surface of the material, which involves the interaction between the target gas and the surface of the material. For a typical p-type Co_3O_4 with holes as major charge carriers. when Co_3O_4 is exposed to the air environment **(Figure4.11(A)),** the electrons from Co_3O_4 are captured by the adsorbed oxygen molecules to form oxygen ions which are temperature dependent such as O_2^- generated below 100 °C, O^- formed between 100 to 300 °C and O^{2-} above 300 °C [30]. Herein O^- is the stable and dominant oxygen species since 100 °C was used as an optimum operating temperature. A hole-accumulating layer (HAL) is then formed on the surface of Co_3O_4 following equation (4.5).

$$\frac{1}{2}O_2 \leftrightarrow O_{2_{(ads)}}^- + h^+ \qquad (4.5)$$

The thickness of the HAL directly influences the resistance of the Co_3O_4 based sensor. Based on the sensing performance observed, Co_3O_4_6hrs showed better sensing performance, indicating that the oxygen ions chemisorbed on the surface of Co_3O_4_6hrs were higher in quantity than that of Co_3O_4_12hrs and Co_3O_4_24hrs, thus the HAL was thicker for Co_3O_4_6hrs.

Upon Co_3O_4 contact with C_2H_4 environment **(Figure 4.11(B)),** the C_2H_4 molecules get oxidized by the oxygen ions into CO_2 and H_2O and at the same time electrons are released back into the Co_3O_4 as per reactions (4.6), and decrease the concentration of holes, therefore, increasing the sensor resistance as per reaction (4.7).

$$C_2H_4 + 3O_2^- \rightarrow 2CO_2 + 2H_2O + 3e^- \qquad (4.6)$$

$$h^+ + e^- = null \qquad (4.7)$$

The amount of chemisorbed oxygen significantly affects the gas sensing reaction, the greater the amount of chemisorbed oxygen, the greater the response. From the sensing performance results, Co_3O_4_6hrs showed a higher response in comparison to Co_3O_4_12hrs and Co_3O_4_24hrs, indicating that the reaction time influences how the Co_3O_4 based sensors convert oxygen to oxygen ions and the quantity of the chemisorbed oxygen, thus influencing the overall performance of the Co_3O_4 based sensors.

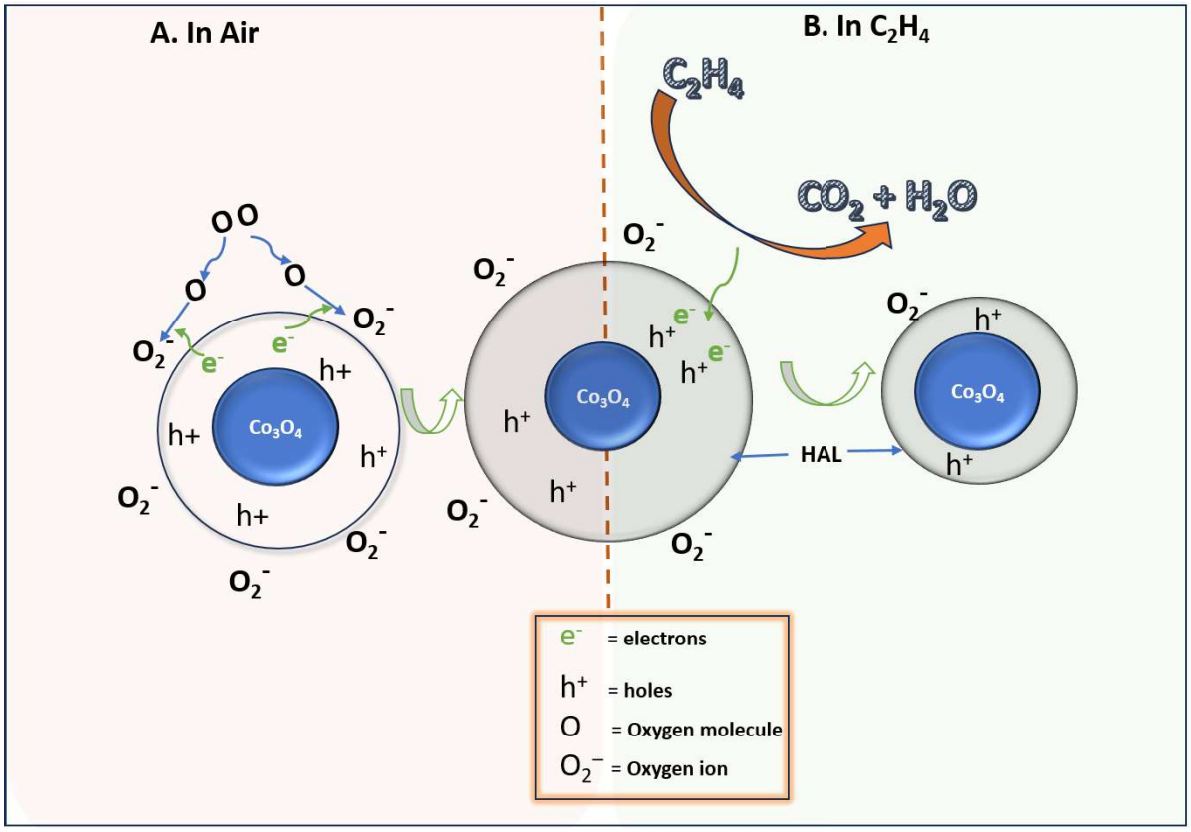

Figure 4. 11: Proposed gas sensing mechanism between Co_3O_4 and C_2H_4.

The gas sensing performance of SMO can be influenced by many factors including morphology, surface area, porosity, defects, and working temperature. In this case, a better response by Co_3O_4_6hrs based sensor towards C_2H_4 at 100 °C in comparison to Co_3O_4_12hrs and Co_3O_4_24hrs based sensors can be attributed to a few factors including the surface area and defects. Despite the sensors being comprised of similar morphology, their properties still differed. BET revealed that the surface area of the Co_3O_4

products reduced with increasing reaction time, indicating that adsorption sites for Co_3O_4_12hrs and Co_3O_4_24hrs based sensors were less in comparison to that of Co_3O_4_6hrs based gas sensor. Further, PL studies demonstrated that the Co_3O_4_6hrs sample had more oxygen vacancies than the rest of the samples, this contributed greatly to the better sensing performance of the Co_3O_4_6hrs based sensor, as oxygen vacancies provide adsorption sites for gas adsorption, thus enhancing the gas sensing performance of the material.

4.4 References

[1] J. Sun, H. Wang, Y. Li, M. Zhao, Porous Co_3O_4 column as a high-performance lithium anode material, J. Porous Mater. 28 (2021) 889-894.

[2] G. Arandhara, J. Bora, P.K. Saikia, Effect of pH on the crystallite size, elastic properties and morphology of nanostructured ZnS thin films prepared by chemical bath deposition technique, Mater. Chem. Phys. 241 (2020) 122277.

[3] K. Shingange, G.H. Mhlongo, D.E. Motaung, O.M. Ntwaeaborwa, Tailoring the sensing properties of microwave-assisted grown ZnO nanorods: Effect of irradiation time on luminescence and magnetic behaviour, J. Alloys Compounds. 657 (2016) 917-926.

[4] M.A. Gondal, Q.A. Drmosh, Z.H. Yamani, T.A. Saleh, Synthesis of ZnO_2 nanoparticles by laser ablation in liquid and their annealing transformation into ZnO nanoparticles, Appl. Surf. Sci. 256 (2009) 298-304.

[5] Y. Kang, F. Yu, L. Zhang, W. Wang, L. Chen, Y. Li, Review of ZnO-based nanomaterials in gas sensors, Solid State Ion. 360 (2021) 115544.

[6] K. Shingange, H.C. Swart, G.H. Mhlongo, Design of porous p-type $LaCoO_3$ nanofibers with remarkable response and selectivity to ethanol at low operating temperature, Sensors Actuators B: Chem. 308 (2020) 127670.

[7] B.M. Matin, Y. Mortazavi, A.A. Khodadadi, A. Abbasi, A.A. Firooz, Alkaline-and template-free hydrothermal synthesis of stable SnO_2 nanoparticles and nanorods for CO and ethanol gas sensing, Sensors Actuators B: Chem. 151 (2010) 140-145.

[8] Z.H. Ibupoto, S. Elhag, M.S. AlSalhi, O. Nur, M. Willander, Effect of urea on the morphology of Co_3O_4 nanostructures and their application for potentiometric glucose biosensor, Electroanalysis. 26 (2014) 1773-1781.

[9] R. Ouyang, J. Liu, W. Li, Atomistic theory of Ostwald ripening and disintegration of supported metal particles under reaction conditions, J. Am. Chem. Soc. 135 (2013) 1760-1771.

[10] N.A. Barakat, M.S. Khil, F.A. Sheikh, H.Y. Kim, Synthesis and optical properties of two cobalt oxides (CoO and Co_3O_4) nanofibers produced by electrospinning process, J. Phys. Chem. C. 112 (2008) 12225-12233.

[11] C.S. Jincy, P. Meena, Synthesis, characterization, and NH_3 gas sensing application of Zn doped cobalt oxide nanoparticles, Inorg. Chem. Commun. 120 (2020) 108145.

[12] G. George, S. Anandhan, Tuning characteristics of Co_3O_4 nanofiber mats developed for electrochemical sensing of glucose and H_2O_2, Thin Solid Films. 610 (2016) 48-57.

[13] Y. Zhang, Y. Chen, T. Wang, J. Zhou, Y. Zhao, Synthesis and magnetic properties of nanoporous Co_3O_4 nanoflowers, Microporous Mesoporous Mater. 114 (2008) 257-261.

[14] N. Poolton, A. Bos, P. Dorenbos, Luminescence emission from metastable Sm_2 defects in Y PO_4: Ce, Sm, J. Condens. Matter Phys. 24 (2012) 225502.

[15] R. Al-Tuwirqi, A.A. Al-Ghamdi, N.A. Aal, A. Umar, W.E. Mahmoud, Facile synthesis and optical properties of Co_3O_4 nanostructures by the microwave route, Superlattices Microstruct. 49 (2011) 416-421.

[16] R.B. Chrisma, A.V. Avani, E.I. Anila, Effect of pH on the structural and optical properties of cobalt oxide nanoparticles synthesized by hydrothermal method, Mater. Today: Proc. 80 (2023) 942-946.

[17] T.P. Mokoena, Z.P. Tshabalala, K.T. Hillie, H.C. Swart, D.E. Motaung, The blue luminescence of p-type NiO nanostructured material induced by defects: H_2S gas sensing characteristics at a relatively low operating temperature, Appl. Surf. Sci. 525 (2020) 146002.

[18] A.M. Abdallah, R. Awad, Sm and Er partial alternatives of Co in Co_3O_4 nanoparticles: probing the physical properties, Phys. B: Condens. 608 (2021) 412898.

[19] H. Sun, X. Tang, J. Zhang, S. Li, L. Liu, MOF-derived bow-like Ga-doped Co_3O_4 hierarchical architectures for enhanced triethylamine sensing performance, Sensors Actuators B: Chem. 346 (2021) 130546.

[20] G.H. Mhlongo, K. Shingange, Z.P. Tshabalala, B.P. Dhonge, F.A. Mahmoud, B.W. Mwakikunga, D.E. Motaung, Room temperature ferromagnetism and gas sensing in ZnO nanostructures: Influence of intrinsic defects and Mn, Co, Cu doping, Appl. Surf. Sci. 390 (2016) 804-815.

[21] K. Zhang, S. Qin, P. Tang, Y. Feng, D. Li, Ultra-sensitive ethanol gas sensors based on nanosheet-assembled hierarchical ZnO-In_2O_3 heterostructures, J. Hazard. Mater. 391 (2020) 122191.

[22] U.T. Nakate, P. Bhuyan, Y.T. Yu, S. Park, Synthesis and characterizations of highly responsive H_2S sensor using p-type Co_3O_4 nanoparticles/nanorods mixed nanostructures, Int J Hydrogen Energy. 47 (2022) 8145-8154.

[23] N. Zhang, S. Ruan, Y. Yin, F. Li, S. Wen, Y. Chen, Self-sacrificial template-driven $LaFeO_3$/α-Fe_2O_3 porous nano-octahedrons for acetone sensing, ACS Appl. Nano Mater. 1 (2018) 4671-4681.

[24] C. Zhang, W. Wang, Y. Pan, L. Cheng, S. Zhai, X. Gao, A two-stage method for real-time baseline drift compensation in gas sensors, Meas. Sci. Technol. 33 (2022) 045108.

[25] A. Helwig, G. Müller, W. Wassner, M. Eickhoff, G. Sberveglieri, G. Fagila, Analysis of the baseline drift phenomenon in nano-crystalline SnO_2 gas sensing layers, (2006) 16-19.

[26] G. Korotcenkov, B.K. Cho, Instability of metal oxide-based conductometric gas sensors and approaches to stability improvement (short survey), Sensors Actuators B: Chem. 156 (2011) 527-538.

[27] K. Shingange, H.C. Swart, G.H. Mhlongo, Enhanced ethanol sensing abilities of fiber-like $La_{1-x}Ce_xCoO_3(0 \leq x \leq 0.2)$ perovskites based-sensors at low operating temperatures, Sensors Actuators B: Chem. 377 (2023) 133012.

[28] A. Maity, A.K. Raychaudhuri, B. Ghosh, High sensitivity NH_3 gas sensor with electrical readout made on paper with perovskite halide as sensor material, Scientific reports. 9 (2019) 7777.

[29] Z. Zhang, C. Yue, D. Dastan, D. Zhang, X. Zhang, X. Yin, X. Ma, High response and selectivity of bimetallic MOFs-derived metal oxides Co_3O_4/In_2O_3 nanoparticles to TEA, Sensors Actuators B: Chem. (2023) 134727.

[30] H. Liu, S.P. Gong, Y.X. Hu, J.Q. Liu, D.X. Zhou, Properties and mechanism study of SnO_2 nanocrystals for H_2S thick-film sensors, Sensors Actuators B: Chem. 140 (2009) 190-195.

CHAPTER 5

Sn- and Zn- doped Co_3O_4: Synthesis, characterization, and gas sensing performance through DFT

5.1 Introduction

This chapter reports the analysis of Sn-doped and Zn-doped Co_3O_4 sheet-like hierarchical structures. The fabrication of the structures is well explained previously in Section 3.2.2 of Chapter 3. Properties of these structures such as crystal structure, morphology, surface area, and defects are studied to observe the effect of doping. The changes in adsorption energies of C_2H_4 on the surface of Co_3O_4 are further explored by employing density functional theory (DFT) calculations.

5.2 Results

5.2.1 Structural analysis

The crystalline structure and phase purity of the obtained products were analysed through XRD, and the resulting patterns are displayed in **Figure 5.1**. The XRD pattern for the pristine Co_3O_4 revealed diffraction peaks located at 2θ values of 19.05°, 31.36°, 36.94°, 38.63°, 44.82°, 55.75°, 59.42° and 65.30° corresponding to (111), (220), (311), (222), (400), (422), (511) and (440) planes of the cubic structure of Co_3O_4 (JCPDS card number 14-0673) with a space group number Fd-3m [1]. Upon addition of Sn dopant **(Figure 5.1(a))**, extra peaks started appearing at 2θ values of 26.65°, 33.95°, 51.85°, 57.88°, 61.93°, and 71.35° for all doping levels (0.5-2wt%) which can be indexed to (110), (101), (211), (002), (310), and (202) planes of tetragonal SnO_2 (JCPDS card number 41-1445) [2,3], moreover, splitting of the (222), (422) and (440) planes of Co_3O_4 into doublets were observed, which can be attributed to the formation of an additional (200), (220), and (112) planes [3] due to the presence of Sn dopant.

On the other hand, doping with Zn **(Figure 5.1(c))**, the cubic Co_3O_4 pattern was maintained up to doping level of 2 wt%, whereby extra diffraction peaks at 2θ values of 31.89°, 34.49°, 47.57°, 56.67°, and 62.93° started appearing which belong to (220), (300), (340), (142) and (450) planes of the ZnO wurtzite structure (JCPDS card number 89-0511). The appearance of these diffraction peaks indicates that the Co_3O_4 lattice exhibited its maximum solubility limit without the presence of the Zn, as the dopant concentration increased the percentage of the Co_3O_4 phase in the products decreased, hence the formation of extra peaks. Furthermore, splitting of the (311) plane into a doublet was observed at higher doping of

2 wt% Zn, suggesting the formation of an additional (101) plane [4] due to the presence of Zn dopant. Compared to Zn the emergence of Sn peaks at a concentration of 0.5wt%, suggests incorporation of Sn into the Co_3O_4 lattice has a more significant impact on the crystal structure even at lower concentrations. For Zn-doped Co_3O_4, the delay in the appearance of new peaks until 2wt% suggests that a higher concentration of Zn is needed to induce similar structural changes [5]. It was noticed that the intensities of the diffraction peaks belonging to Co_3O_4 deteriorated following the addition of the dopants, indicating deterioration of the crystallinity of Co_3O_4. Contrary to this, the intensity of the extra peaks belonging to the SnO_2 increased with increasing Sn concentration.

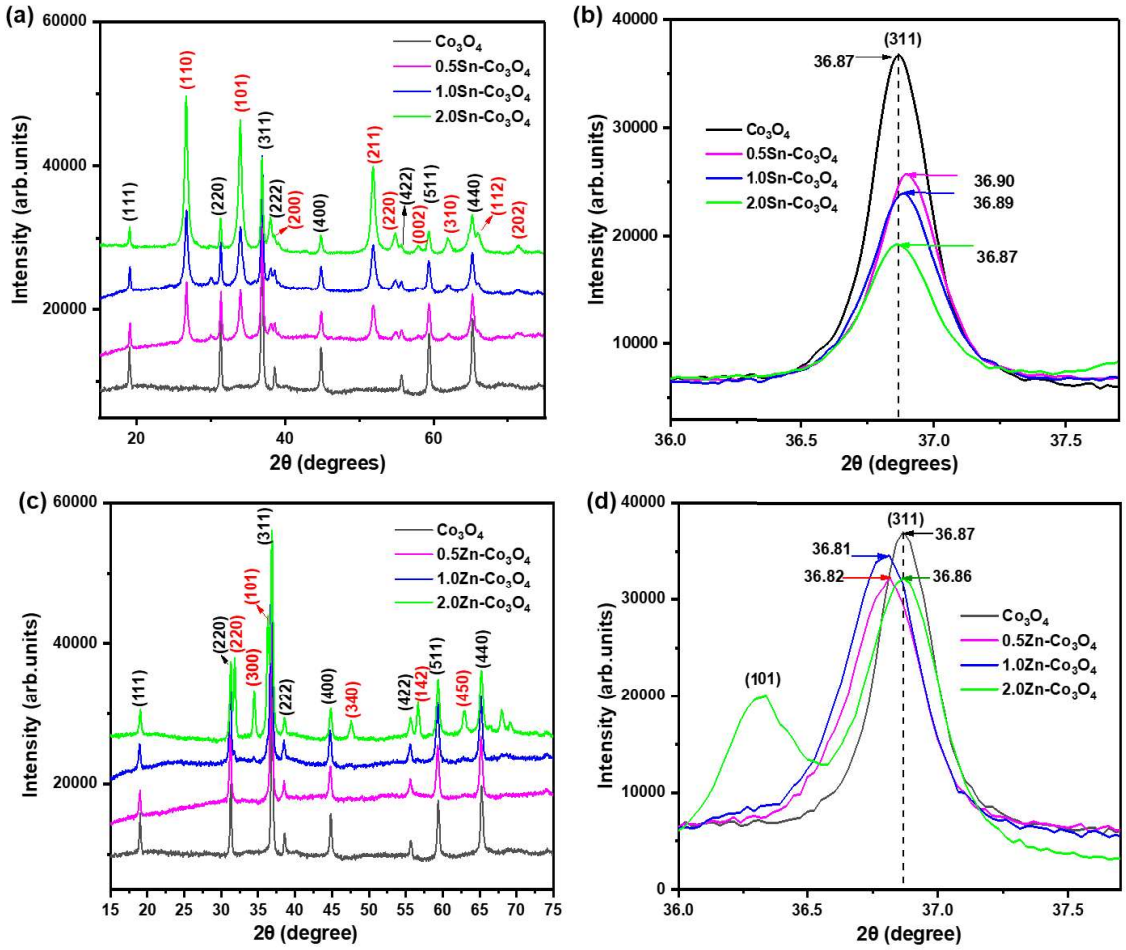

Figure 5. 1: (a and c) XRD patterns and (b and d) enlarged (311) diffraction peaks of the (a, b) Sn-doped and (c, d) Zn-doped Co_3O_4 structures.

Figure 5.1(b and d) illustrate the magnified diffraction peak corresponding to the (311) plane for the Co_3O_4, respectively. The peak shifted to a higher 2θ angle for the Sn-doped Co_3O_4 products **(Figure 5.1(b))**, whereas the peak shifted to a lower angle for the Zn-doped Co_3O_4 products **(Figure 5.1(d))**. Peak

shift to higher and lower angles indicates the shortening and elongation of the interplanar spacing (*d*), which in turn leads to compression and expansion of the Co_3O_4 lattice through the doping of larger ionic radii of Sn^{4+} (0.69 Å) and Zn^{2+} (0.74 Å) to the small ionic radii of Co (0.63 Å), respectively. The observed shifts agree well with previous reports of doped Co_3O_4, thereby confirming that these shifts strongly depend on the dopant concentration [6,7]. This behavior also suggests that the incorporation of Sn and Zn ions induces lattice strain in the Co_3O_4 lattice.

Peak broadening was also observed, suggesting a reduction in the crystallite size (*D*) which was confirmed by using the Debye-Scherrer equation [8]:

$$D = \frac{k\lambda}{\beta cos\,\theta} \tag{5.1}$$

Where *D* is the crystalline size, *k* is the shape factor (1), λ is the wavelength, β is the full width at half maximum, and θ is the reflection angle. The obtained values are listed in **Table 5.1**. The crystallite size of the Co_3O_4 structures was shown to decrease with increasing Sn and Zn concentration. This can be attributed to the unmatched incorporation of Sn and Zn cations onto the Co_3O_4 crystal structures reducing the concentration of Co, which results in suppressed grain growth of the doped Co_3O_4 structures [9]. A similar trend was observed by Wang et al. [10] for Sn-doped Co_3O_4, respectively. Further, the presence of strain inside the Co_3O_4 lattice is considered one of the important parameters contributing to the observed shift in diffraction peak positions as highlighted above, so the micro-strain (ε) has been estimated using the equation [11]:

$$\varepsilon = \frac{\beta}{4(tan\theta)} \tag{5.2}$$

Where ε is the micro-strain, β is the full width at half maximum, and θ is the reflection angle. The micro-strain values were found to increase with increasing doping concentration for both dopants as shown in **Table 5.1**. The increase in micro-strain for doped Co_3O_4 is accounted for the distortion of the Co_3O_4 lattice created by the dopant ions due to the incompatibility or mismatch between the ionic radii of Sn^{4+}, Zn^{2+}, Co^{2+}/Co^{3+}. Moreover, peak shifts tempers with the lattice interplanar spacing estimated from Bragg's law [12]:

$$n\lambda = 2\,dsin\ \theta \tag{5.3}$$

Where *n* is the order of diffraction (*n = 1*), λ is the Cu-Kα wavelength (1.540598) and θ is half the position of the peaks. In this case, the lattice d-spacing varied with the different levels of both dopants as displayed in **Table 5.1**. All changes in the host structure such as peak shifts, broadening, crystallinity change, and

the formation of new peaks can be attributed to the lattice parameter variations. The lattice parameter variations are linked to the dopant ions concentration, atomic radii, defects, and generated strains, the lattice parameter for the pristine cubic structure of Co_3O_4 was found to be a = b = c = 8.078 Å using the equation [13]:

$$a = d\sqrt{k^2 + h^2 + l^2} \quad (5.4)$$

Where, *a* is the lattice parameter, *h*, *k*, and *l* are Miller indices and *d* is the interplanar distance. The lattice parameters obtained because of Sn and Zn doping are listed in **Table 5.1**, where it is obvious that the lattice parameter ***a*** varied upon dopant concentration.

Table 5.1: XRD properties of the Sn and Zn doped Co_3O_4 products.

Product	**2θ (deg.)**	**d-spacing (nm)**	**D (nm)**	**a (Å)**	**Microstrain (Ɛ)**
Co_3O_4	36.872	0.243	33.314	8.078	0.0004062
0.5Zn-Co_3O_4	26.940	0.244	26.932	8.094	0.0005013
1.0Zn-Co_3O_4	25.986	0.244	25.979	8.097	0.0005195
2.0Zn-Co_3O_4	10.653	0.244	10.648	8.112	0.0012645
0.5Sn-Co_3O_4	36.902	0.243	31.095	8.072	0.0004234
1.0Sn-Co_3O_4	36.885	0.243	29.290	8.076	0.0004622
2.0wt%Sn-Co_3O_4	36.867	0.243	30.380	8.079	0.0004454

5.2.2 Morphological analysis (SEM and TEM)

The morphology and microstructure of the as-prepared pure and Sn and Zn-doped Co_3O_4 samples in **Figure 5.2** were investigated through Scanning Electron Microscopy (SEM). In **Figure 5.2(a)** the as-prepared pure Co_3O_4 sample exhibited 2D uniform porous nanosheets morphology, the presence of pores is important for gas diffusion processes resulting in enhanced gas sensing performance [14]. Upon addition of Sn dopant, (see **Figure 5.2(b-d))** the samples displayed hierarchical flower-like morphology consisting of many small nanosheets, as the Sn doping concentration increased the more the flower-like structures became denser. It is apparent that addition of the Sn dopant resulted in the sheet-like structures to assemble in flower-like structure. The change in morphology observed was attributed to the difference in Sn and Co ions, which altered with the surface energy of the Co_3O_4 surface leading to the formation of hot spots that acted as nucleation sites for second growth of Co_3O_4, hence the formation of the special

Co_3O_4 nanostructures [15]. Addition of Zn dopant in **Figure 5.2(e-g)** revealed the flower-like shape morphology form doping level of 1wt% but displayed aggregation due to altered conditions for the nucleation and growth of Zn-doped Co_3O_4 [16,17], as well as the combined effect of van der Waals forces and electrostatic interactions between the particles encouraging self-aggregation of nanoparticles to form nanoplates like morphology [18].

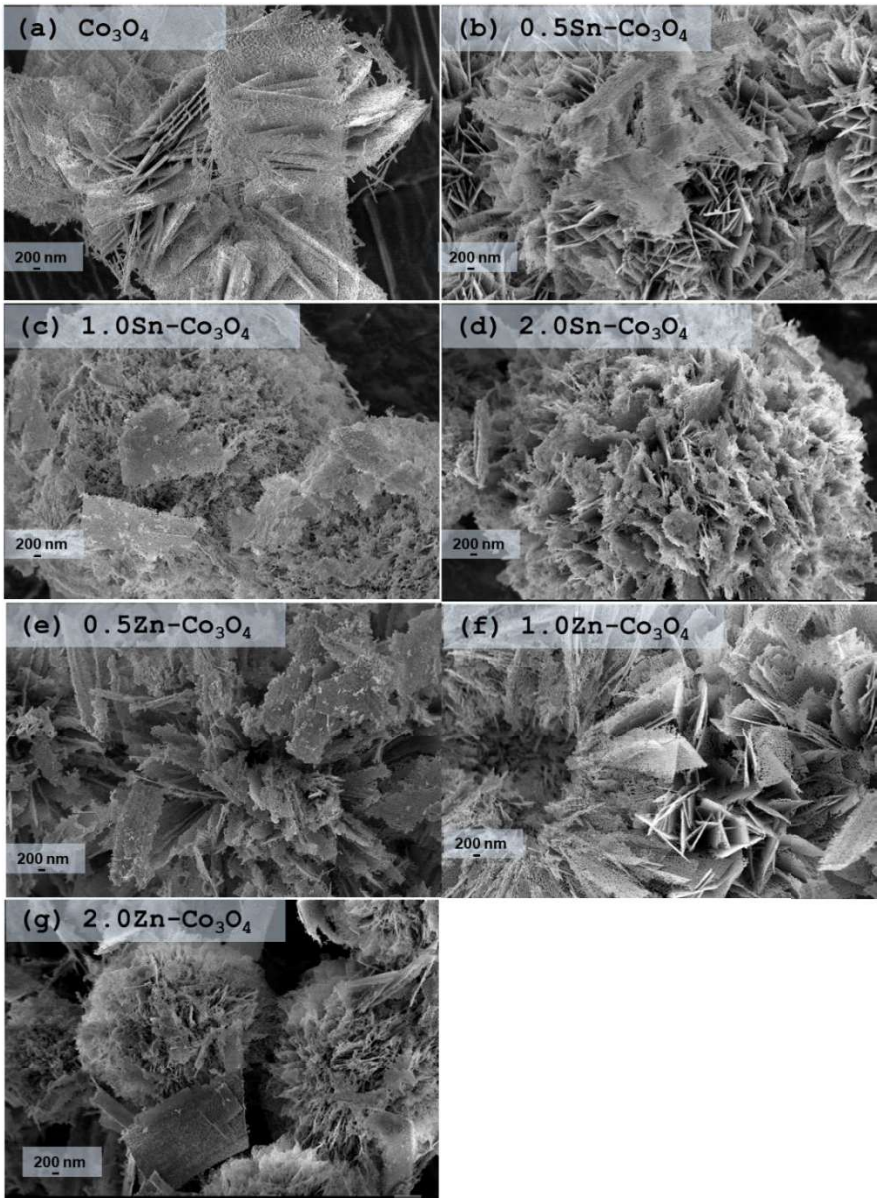

Figure 5. 2: SEM images of the (a) pristine and (b-d) Sn- and (e-g) Zn-doped Co_3O_4 nanostructures.

For an in-depth analysis of the microstructural characteristics of Co_3O_4 nanostructures doped with Sn and Zn, Transmission Electron Microscopy (TEM), High-Resolution TEM (HR-TEM), and Energy Dispersive X-ray Spectroscopy (EDS) were employed. Specifically, the investigation focused on the

pristine Co_3O_4 and the doped variants, namely 2.0Sn-Co_3O_4 and 2.0Zn-Co_3O_4. The TEM micrographs presented in **Figure 5.3(a, b, and c)** depict the sheet-like structural morphology of Co_3O_4, 2.0Sn-Co_3O_4, and 2Zn-Co_3O_4 nanostructures, respectively. The HR-TEM micrographs, displayed in **Figure 5.3(d, e, and f),** further illustrate the microstructural details of Co_3O_4, 2.0Sn-Co_3O_4, and 2.0Zn-Co_3O_4 nanostructures. Examination of these micrographs revealed distinct lattice fringes with d-spacing values of 0.24 and 0.29 nm for the pristine Co_3O_4, corresponding to the (311) and (220) planes of Co_3O_4, respectively. In the case of 2.0Sn-Co_3O_4, lattice fringes with d-spacing of 0.28, 0.33, and 0.34 nm, correspond to (220) and (110) planes of SnO_2 and Co_3O_4, respectively. Meanwhile, lattice fringes observed for 2.0Zn-Co_3O_4 nanostructures were 0.29 and 0.47 nm, corresponding to (220) and (111) planes of Co_3O_4, respectively. These findings are consistent with the XRD results. To validate the presence and distribution of Sn and Zn in the Co_3O_4 nanostructures, EDS elemental maps were acquired and are presented in **Figure 5.3(g, h, and i).** The EDS maps confirm the existence of Co and O in the pristine product, while Co, O, and Sn are observed in the 2.0Sn-Co_3O_4 nanostructures, and Co, O, and Zn are evident in the 2.0Zn-Co_3O_4 nanostructures.

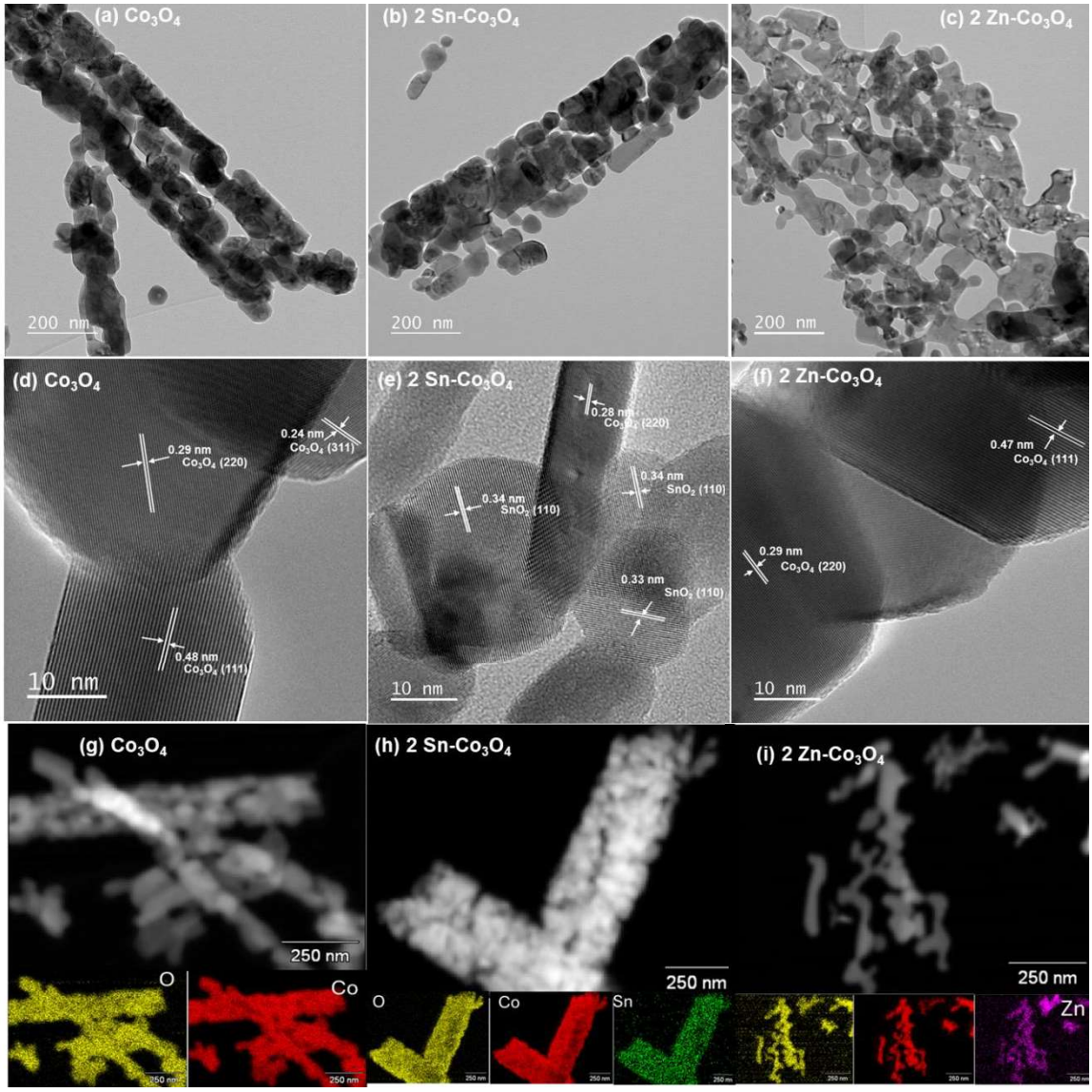

Figure 5. 3: (a-c) TEM, (d-f) HR-TEM images and (g-i) EDS elemental maps of the pristine, Co_3O_4, 2.0Sn-Co_3O_4 and 2.0Zn- Co_3O_4 structures.

5.2.3 Surface area analysis

Previous studies have shown that doping reduces crystal size which may enhance the surface area of the nanostructures [20], so to establish the relationship between the crystal size and the surface characteristics of the pristine and the Sn and Zn doped Co_3O_4 nanostructures, BET measurements were performed. **Figure 5.4(a-g)** illustrates the nitrogen (N_2) adsorption-desorption isotherms for both pristine Co_3O_4 nanostructures and those doped with Sn and Zn. All presented isotherms exhibit characteristics consistent with the type IV isotherm, as defined by the International Union of Pristine and Applied Chemistry (IUPAC) [21]**.** Notably, each sample displays a discernible H3 hysteresis loop at relatively elevated

pressures across all isotherms, indicative of the capillary condensation-driven filling and emptying of mesopores within the 2-50 nm diameter range [22,23]. Furthermore, the observed hysteresis loop for all products approaches $P / Po = 1$ suggesting the presence of macro-pores exceeding 50 nm [24]. The pristine Co_3O_4 nanostructures exhibited a specific surface area value of 10.5967 m^2/g. Upon Sn doping at levels of 0.5, 1, and 2 wt%, the specific surface area values demonstrated an increase, reaching 11.1365, 13.1787, and 15.0528 m^2/g for 0.5Sn-Co_3O_4, 1.0Sn-Co_3O_4 and 2.0Sn-Co_3O_4, respectively. Similarly, the Zn-doped Co_3O_4 nanostructures exhibit an enhanced surface area, with values of 17.7512, 19.2681, and 18.5647 m^2/g for 0.5Zn-Co_3O_4, 1.0Zn-Co_3O_4 and 2.0Zn-Co_3O_4 nanostructures, respectively. The enlarged surface area resulting from Sn and Zn doping implies the development of more active sites. This increase in surface area in the Sn and Zn-doped Co_3O_4 nanostructures holds significant promise for gas sensing applications, as a larger surface area provides more active sites, ultimately improving sensitivity.

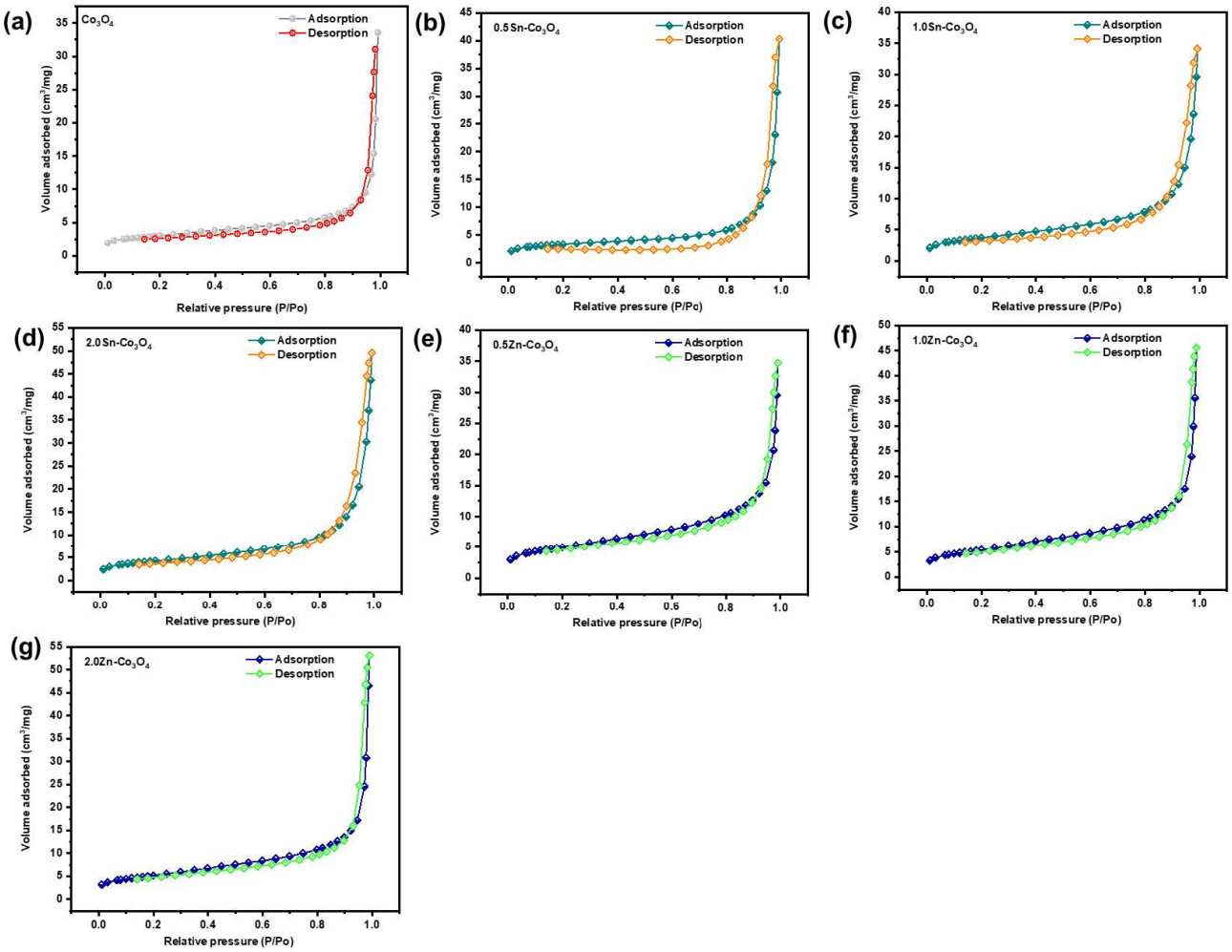

Figure 5. 4: Nitrogen adsorption-desorption isotherms for the pristine (a), (b, c, d) Sn-doped, and (e, f, g) Zn-doped Co_3O_4 nanostructures.

5.2.4 Chemical analysis (XPS)

XPS analyses were performed to validate the pristine, Zn-, and Sn-doped Co_3O_4 formation. Additionally, to investigate the oxidation states of the elements in both pristine and doped Co_3O_4, and to confirm the impact of chemisorbed oxygen species on the sensors' detecting capabilities. **Figure 5.5(a-c)** displays the XPS survey spectra of Co_3O_4, 2.0 Sn-Co_3O_4, and 2.0 Zn-Co_3O_4. The photoelectron signals of Co, O, and C were identified in all the products, indicating their existence in Co_3O_4 and Sn and Zn doped Co_3O_4. Furthermore, the photoelectron signals of Sn and Zn were identified respectively in 2.0 Sn-Co_3O_4 and 2.0 Zn-Co_3O_4, indicating their existence, respectively, **(Figure 5.5(b and c)).** The notable C 1s signal detected may have originated from the adsorbed carbon on the surface of the products or from the carbon-based strip employed in the analysis. The Co 2p XPS spectra, as seen in **Figure 5.5(d-f),** exhibit Co $2p_{3/2}$ peak at approximately 780 eV binding energy and a Co $2p_{1/2}$ peak at approximately 796 eV binding energy. The existence of Co_3O_4 in every product is verified by these peaks along with the Co $2p_{3/2}$ satellite

peak located at around 787 eV binding energy and Co $2p_{1/2}$ satellite peak located at around 804 eV binding energy. Subsequently, the Co $2p_{3/2}$ peak and Co $2p_{1/2}$ peak were further fitted to provide a thorough examination of Co's oxidation state. The Co $2p_{3/2}$ peak was split into peaks corresponding to Co^{3+} and Co^{2+} oxidation states, respectively located approximately at 779 eV and 782 eV. Moreover, peaks located at approximately 794 eV binding energy and 797 eV binding energy, which correspond to Co^{3+} and Co^{2+} oxidation states, respectively, were found in Co $2p_{1/2}$ peak.

Figure 5.5(g) depicts the XPS Sn 3d spectrum. It is clear that some of the Sn metals oxidized to Sn^{4+}. The peaks at approximately 485 eV and 487 eV confirm respectively the presence of Sn metals and SnO_2 in 2.0 Sn-Co_3O_4. On the other hand, the peaks located approximately at 1021 eV and 1022 eV binding energies designate the presence of Zn metal and ZnO respectively in 2.0 Zn-Co_3O_4, **(Figure 5.5(h)).**

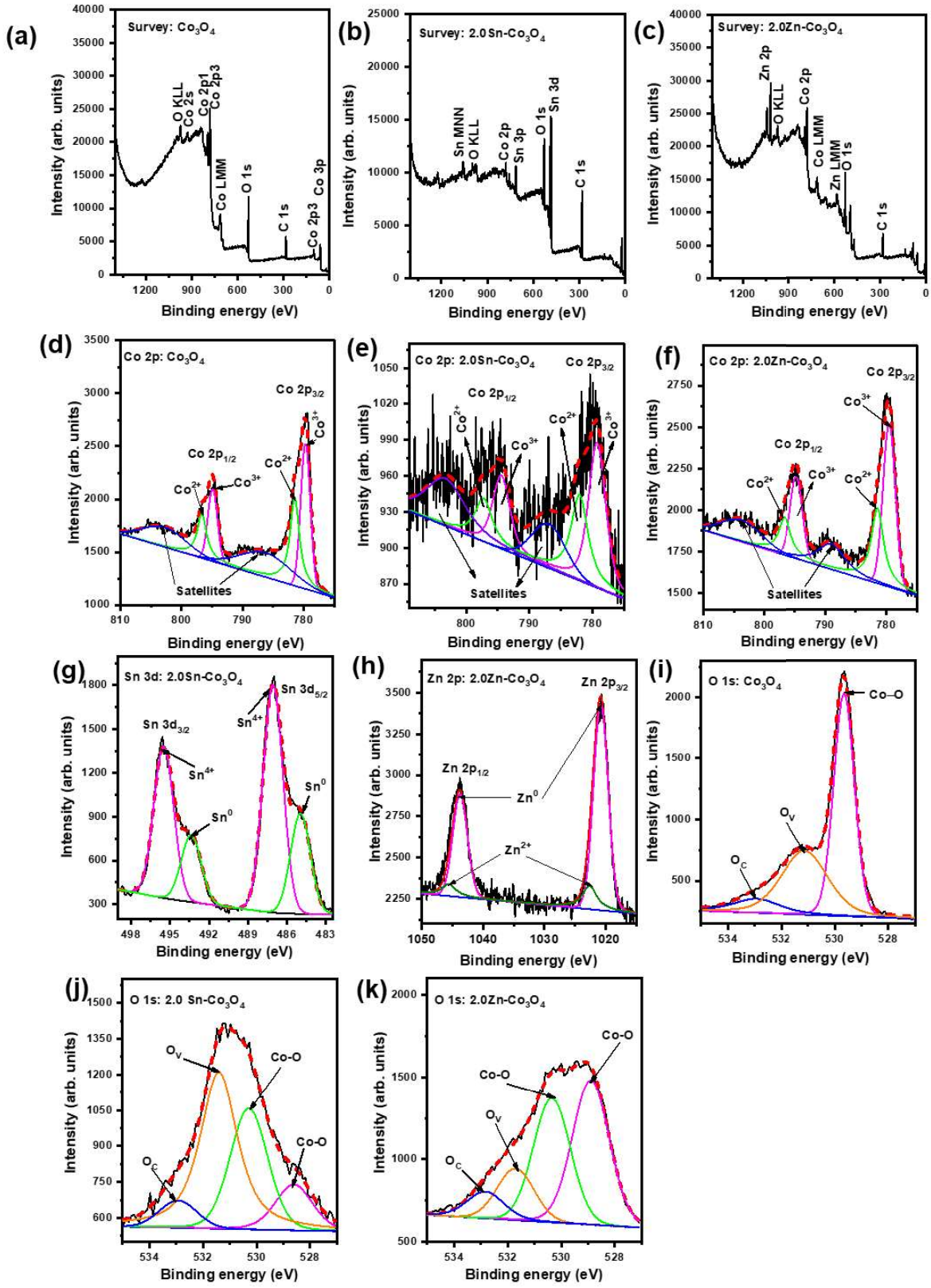

Figure 5. 5: XPS survey spectra for (a) pristine, (b) Sn- doped, and (c) Zn- doped Co_3O_4. HR XPS Co 2p spectra for (d) pristine, (e) Sn- doped, and (f) Zn- doped Co_3O_4, HR XPS spectra for (g) Sn 3d and (h) Zn 2p and HR XPS O 1s spectra for (i) pristine, (j) 2.0 Sn-Co_3O_4, and (k) 2.0 Zn-Co_3O_4.

Furthermore, the status of the oxygen species in the products was verified by the HR XPS O 1s spectra shown in **Figure 5.5(i-k)**, which were de-convoluted into fitted peaks. For the pristine Co_3O_4, three peaks were fitted and were located at 529.6, 530.9, and 531.1 eV, respectively. As for the 2.0 Sn-Co_3O_4, the fitted peaks were observed at 528.6, 530.3, 531.4, and 532.9 eV, respectively. On the other hand, fitted O 1s for 2.0 Zn-Co_3O_4 revealed peaks at 528.9, 530.4, 531.7, and 532.8 eV, respectively. The peaks in the lowest binding energy (529.6, 528.6, and 528.9 eV) correspond to a Co-O bond and the second peak at 530.3 and 530.4 eV shows a Co-O bond with a higher oxidation state [25,26]. The peaks at 530.9, 531.4, and 531.7 eV correspond to bonds between carbon and oxygen, e.g. C-O or O=C-O components [26,27]. The peaks at the highest binding energy are due to the water adsorbed onto the surface [27,28]. **Table 5.2** lists the content percentages that correspond to the various oxygen species. The binding energy increases respectively for Co-O, O_V, and O_C i.e., the binding energy of $O_L < O_V < O_C$, this was previously seen in other reports [29-31].

Table 5.2: A summary of the Co-O, O_V, and O_C content percentage (%) for Co_3O_4, 2.0 Sn-Co_3O_4, and 2.0 Zn-Co_3O_4.

Products	Co-O (%)	O_V (%)	O_C (%)	Ov/Co-O
Co_3O_4	52.8	37.8	9.4	0.71
2.0 Sn-Co_3O_4	42.9	50.4	6.7	1.17
2.0 Zn-Co_3O_4	77.2	14.5	8.3	0.18

The incorporation of Sn in Co_3O_4 prompted the ascent of O_V consequently prompting a descent in Co-O and O_C. On the other hand, Zn doping prompted a descent in O_V and O_C contents while increased Co-O was observed (see **Table 5.2)**. The sensing mechanism of a gas sensor depends on O_V, as such, the higher the O_V the better the sensing properties. As a result, a gas sensor based on 2.0 Sn-Co_3O_4 stands as a promising gas sensor contrasted to its counterparts.

5.3 Gas sensing performance: Computational calculations

This section investigates and analyses the in-depth gas adsorption phenomena between the C_2H_4 gas and Co_3O_4 (311) surface, as well as the doping effect of Sn and Zn, by employing the DFT calculations from the material studio of Biovia. This helps gain deeper insights into the atomic scale that is challenging to observe experimentally. The computational method used in this study is explained in detail in Chapter 3 section 3.5.

5.3.1 Electronic properties

The classification of materials into metals, semiconductors, and insulators is based on their electronic properties, particularly the width of the energy band gap between the conduction band (CB) and the valence band (VB) [32]. This gap is small enough that, at higher temperatures or with the application of external energy, valence electrons can gain sufficient energy to jump into the conduction band, allowing for the conduction of electricity of the material, this is valid for semiconductor materials only. **Figure 5.6** illustrates the density of states indicating the elemental contribution towards the formation of the band gap of 0.3 eV of the (a) bulk structure (b) Pristine Co_3O_4 (311) surface and of Chemisorbed (c) C_2H_4/ Co_3O_4 (311) surface, (g) C_2H_4/Sn-Co_3O_4 (311) surface, (h) C_2H_4/Zn-Co_3O_4 (311) surface. and of Physisorbed (d) C_2H_4/Co_3O_4 (311) surface, (e) C_2H_4/Sn-Co_3O_4 (311) surface, (f) C_2H_4/Zn-Co_3O_4 (311) surface. Compared to the experimental value of 1.6 eV obtained from the UV-Vis in Chapter 4 (Figure 4.5) the computational band gap is severely underestimated due to the GGA/PBE function used [33,34]. A noticeable broadening in the density of states is related to covalent bonding and a change is due to the energy levels corresponding to ionic bonding [35].

In both the DOS analysis for physisorption and chemisorption in **Figure 5.6(c,d)**, it was observed that new states appeared near the lower end of the conduction band, effectively overlapping with the Fermi energy in the direction of the valence band. This phenomenon leads to the transformation of the semiconducting material into a semi metallic material. The density of states (DOS) showed additional peaks in the lower part of the valence band (VB) between -8 and -17 eV, like those obtained when the states of C_2H_4 molecules were found in the VB.

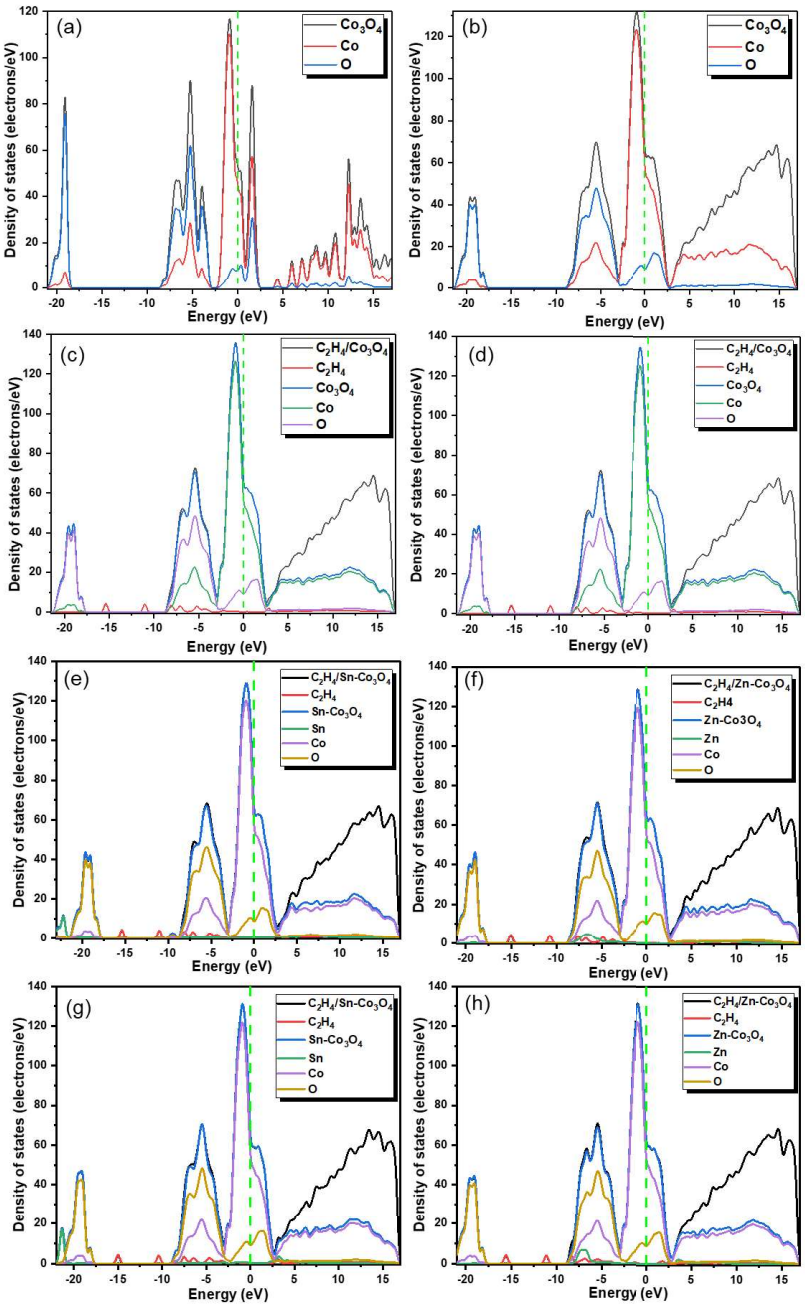

Figure 5. 6: Density of States of the (a) bulk structure (b) pristine Co_3O_4 (311) surface and of Chemisorbed (c) C_2H_4/ Co_3O_4 (311) surface, (g) C_2H_4/Sn-Co_3O_4 (311) surface, (h) C_2H_4/Zn-Co_3O_4 (311) surface. and of Physisorbed (d) C_2H_4/Co_3O_4 (311) surface, (e) C_2H_4/Sn-Co_3O_4 (311) surface, (f) C_2H_4/Zn-Co_3O_4 (311) surface.

Upon introduction of Sn and Zn, a change in the electronic behavior of the doped systems due to the impurity states introduced by Sn and Zn dopants is observed as illustrated. During the physisorption approach **(Figure 5.6(e-f))**, the Sn peak appeared between -21 eV and -20 eV and re-appeared again around -10 eV in the valence band region, during chemisorption **(Figure 5.6 (g-h))** it reappeared around 4 eV in the conduction band region. Zn peaks appeared at around -6 eV near the fermi level in both the

adsorption approaches. The considerable overlaps of the dopant's peaks suggest orbital hybridization [36].

5.3.2 Adsorption properties

The adsorption process and the way the gaseous molecule C_2H_4 is exposed to the surface were studied by determining the adsorption energy. The calculated E_{ads} of the C_2H_4/Co_3O_4 (311) system and the equilibrium surface-molecule distance values (d, defined as the shortest atom-to-atom distance) are shown in **Table 5.3.** The adsorption approaches used are physisorption and chemisorption. Physisorption is an adsorption without forming a bond between the molecule and the surface, and chemisorption is the opposite of physisorption. The observed negative values of the adsorption energy (E_{ads}) indicate strong thermodynamic stability and the exothermic nature of the system [32], and also indicate that the Co site is energetically favourable for the adsorption of C_2H_4, which means that the C_2H_4 molecules are spontaneously adsorbed at all sites without additional energy, highlighting the applicability of Co_3O_4 sheet-like structures to detect C_2H_4. Transitional metals such as Sn and Zn can enhance gas adsorption by creating chemically active sites on the surface which results in a change of adsorption energy and charge transfer between the molecule and the surface [37,38].

The adsorption energies for both physisorption and chemisorption of the Sn-doped system increased more than the pristine system, however, the adsorption energies of the Zn-doped system decreased more than the pristine system **(Table 5.3).** C_2H_4/Sn-Co_3O_4(311) system displays strong and stable adsorption capacity towards C_2H_4. Compared to Zn, Sn doping can improve Co_3O_4 gas sensing capabilities when introduced as a dopant onto the pristine surface to explore the gas adsorption behaviour of C_2H_4 more significantly. The smaller E_{ads} value due to Zn doping results in the possibility of self-desorption of C_2H_4 on the surface, suggesting that C_2H_4 is more likely to detach from the surface on its own. This increased self-desorption improves the sensor's response to changes in the gas environment [39].

Table 5.3: The adsorption energy (E_{ads}) of the C_2H_4/Co_3O_4 (311) system and the equilibrium surface-molecule distance (d, defined as the shortest atom-to-atom distance).

System	Adsorption techniques	
	Physisorption	**Chemisorption**
C_2H_4/Co_3O_4 (311)	**d_{C-Co} = 1.990 Å**	**d_{C-Co} = 2.000 Å**
	E_{ads} = -1.440 eV	**E_{ads} = -1.428 eV**
C_2H_4/Sn-Co_3O_4 (311)	**d_{C-Co} = 1.973 Å**	**d_{C-Sn} = 3.198 Å**
	E_{ads} = -1.526 eV	**E_{ads} = -1.457 eV**
C_2H_4/Zn-Co_3O_4 (311)	**d_{C-Co} = 2.826 Å**	**d_{C-Zn} = 2.611 Å**
	E_{ads} = -1.407 eV	**E_{ads} = -0.689 eV**

Full geometry optimisation was performed to investigate the effects of exposure to C_2H_4 on the surface of Co_3O_4 (311), as it helps to minimise the total energy of the system by adjusting the positions of the atoms to find the most stable configuration. **Figure 5.7** depict Physisorption technique on (a) pristine Co_3O_4 (311) surface, (c) C_2H_4/Sn-Co_3O_4 (311) surface, and (d) C_2H_4/Zn-Co_3O_4 (311) surface, Chemisorption technique on (b) pristine Co_3O_4(311) surface, (e) C_2H_4/Sn-Co_3O_4 (311) surface, and (f) C_2H_4/Zn-Co_3O_4 (311) surface. The adsorption interaction configuration of the Co_3O_4 (311) is led by the bonding of C atoms. A potential adsorption configuration is that in this work, the carbon atom of C_2H_4 can form a coordinate bond with a surface cobalt atom, resulting in the formation of a Co-C bond of 1.990 Å and 2.000 Å. The double bond of the C_2H_4 molecule can break, and one carbon atom interacts with the surface while the other carbon atom retains its original bonding. Similarly, the C_2H_4 molecule can also interact with oxygen atoms on the surface of Co_3O_4 (311) through weak van der Waals forces. These interactions may involve the π-electron cloud of the C_2H_4 molecule and oxygen atoms on the surface [32]. In addition, optimised doped systems with chemisorption approach, forms C-Zn and C-Sn bonds.

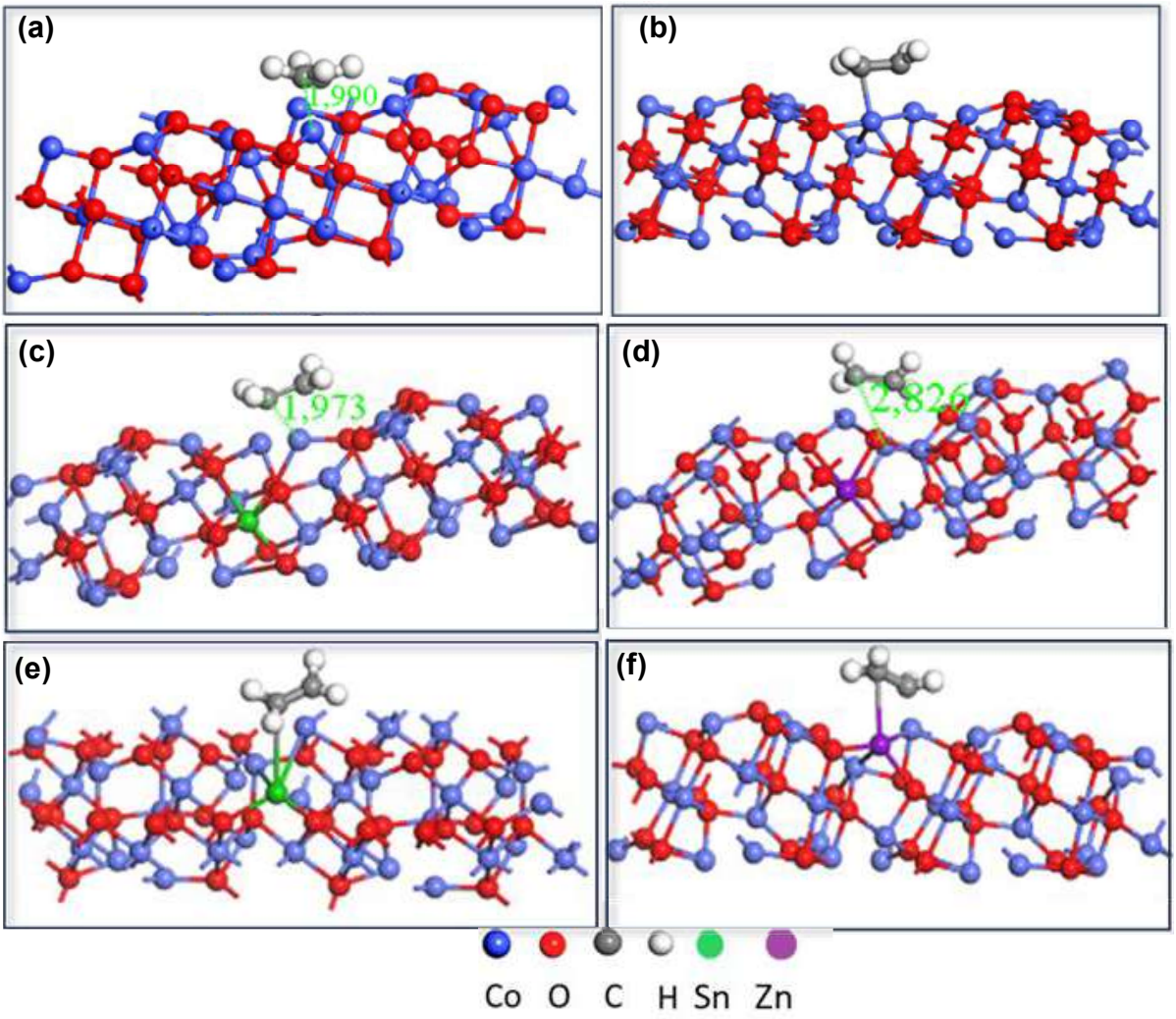

Figure 5. 7: Physisorption technique on (a) pristine Co_3O_4 (311) surface, (c) C_2H_4/Sn-Co_3O_4 (311) surface, and (d) C_2H_4/Zn-Co_3O_4 (311) surface, Chemisorption technique on (b) pristine Co_3O_4 (311) surface,(e) C_2H_4/Sn-Co_3O_4 (311) surface, and (f) C_2H_4/Zn-Co_3O_4 (311) surface.

5.4 Gas sensing mechanism

Metal oxide semiconductors-based gas sensors operate based on the change in electrical properties due to the presence of gases. Their primary chemiresistive property is associated with adsorption and desorption interactions between the gas molecules and the surface of the sensing materials. The detailed gas sensing mechanism below helps understand why the introduction of C_2H_4 gas changes the electrical properties of a Co_3O_4-based gas sensor [35].

When the Co_3O_4 sensor is introduced to the air environment as depicted in **Figure 5.8(a)** oxygen molecules are adsorbed on the Co_3O_4 surface, and the electrons found in the material are captured by these oxygen molecules to form oxygen ions species (O_2^-,$O^-$and O^{2-}), resulting in the formation of a

hole accumulation layer on the surface. The formation of these oxygen ions depends on the working temperature used, below the working temperature of 100 °C, O_2^- forms because of low activation energy, when the temperature is between 100 and 300 °C, O^- ions dominate. In this study, the working temperature was set to 100 °C therefore O^- ion species is the one formed after extraction of electrons by oxygen molecules, which acts as active sites for efficient gas adsorption The processes of how these oxygen molecules adsorb on the Co_3O_4 surface are defined by formulas (5.6) - (5.8).

$$O_2(gas) \rightarrow O_2(ads) \tag{5.6}$$

$$O_2(ads) + e^- \rightarrow O_2^-(ads) \tag{5.7}$$

$$O_2^-(ads) + e^- \rightarrow 2O^-(ads) \tag{5.8}$$

When the sensor is introduced to the C_2H_4 environment as depicted in **Figure 5.8(b)** C_2H_4 molecules react with oxygen ions, which makes the electrons trapped to be released back into the Co_3O_4 material, because of this reaction the hole accumulating layer becomes smaller as the electron concentration increases, and the processes of the reactions between the C_2H_4 molecules and oxygen ions are given by equation (5.9)

$$C_2H_4(gas) + 6O^-(ads) \rightarrow 2CO_2(ga) + 2H_2O(gas) + 6e^- \tag{5.9}$$

Doping is one of the techniques used to enhance the sensitivity and selectivity of gas sensors, the effect of doping depends on the type of dopants used and the sensing material [40]. In this work, transitional metals are used as dopants, and distinct behaviours were observed through DFT calculations. Computationally doping significantly improved the adsorption energies for each dopant. The Zn and Sn doping atoms have been turned into ZnO and SnO_2 respectively in the Co_3O_4 lattice, which was confirmed by XRD and XPS data hence the surface of the sensor contains ZnO-Co_3O_4 and SnO_2-Co_3O_4 p-n junctions. Both experimental and computation data point out Sn dopant to improve Co_3O_4 gas sensing capabilities, as such **Figure 5.8(c,d)** delves into the SnO_2-Co_3O_4 p-n Heterojunction mechanism, which constructs an electronic junction at the interface between n-(Zn/Sn) and p-(Co_3O_4). The difference in fermi level causes electrons from SnO_2 with a big band gap of 3.6 eV and holes from Co_3O_4 with a low band gap of 1.6 eV to flow in opposite directions to equilibrate the fermi level, when the sensor is exposed to air the reaction processes of equation (5.6)-(5.8) takes place on the SnO_2-Co_3O_4 hierarchical structures. The flow of electrons from SnO_2 decreases, resulting in a decrease of the hole-depletion layer on the Co_3O_4 side. When the sensor is introduced to the C_2H_4 environment, process reactions following equation

(5.9) take place on the SnO_2-Co_3O_4 material, leading to an increase of the hole-depleting layer, which results in resistance change.

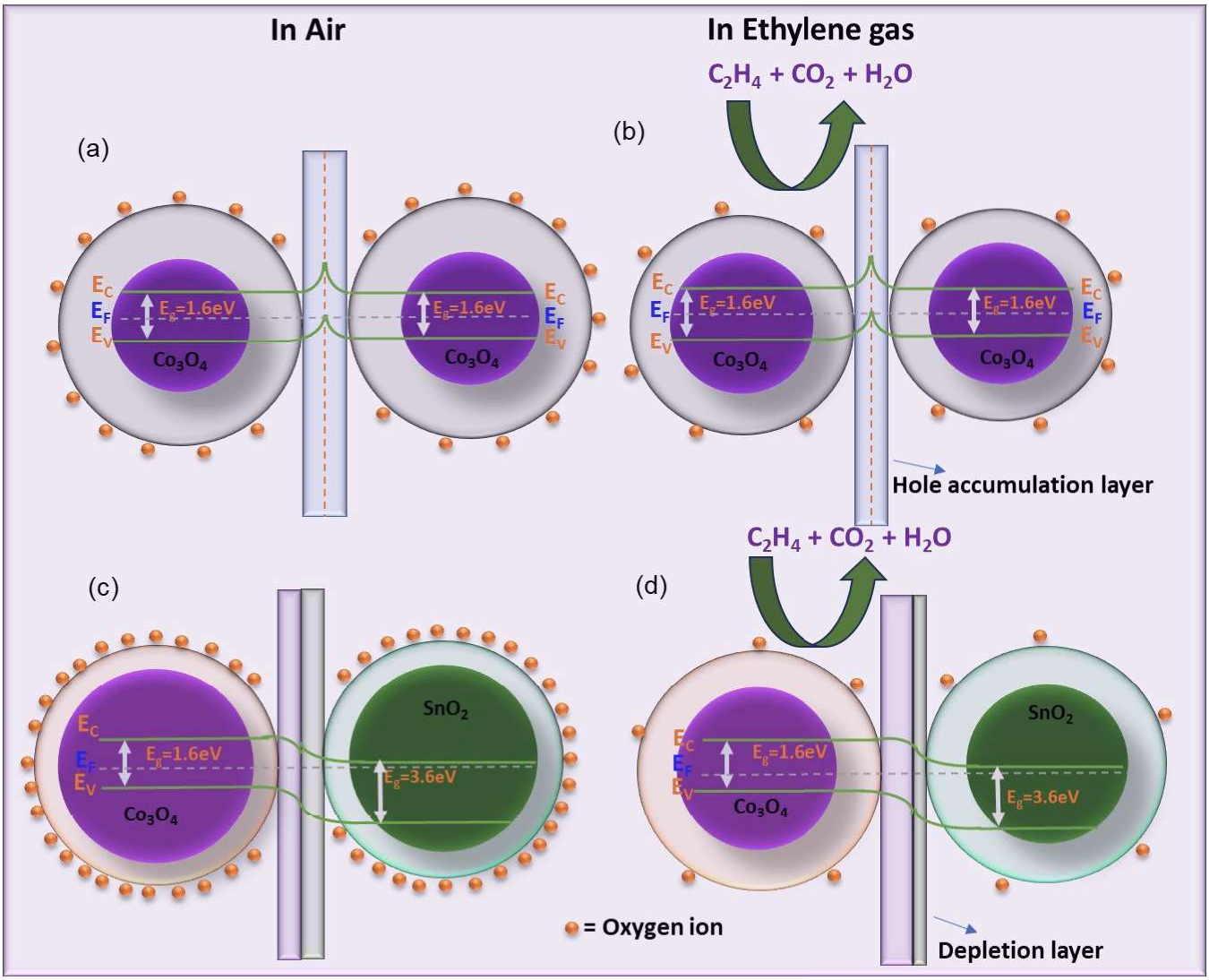

Figure 5. 8: Schematic diagram of the gas sensing mechanism and band energies of Co_3O_4 exposed to (a) air environment, (b) C_2H_4 environment, and (c) SnO_2-Co_3O_4 in air environment and (d) SnO_2-Co_3O_4 in C_2H_4 environment.

5.5 References

[1] A.K. Sinha, R.K. Gupta, S.K. Deb, A correlation between structural and optical properties of cobalt oxide nanoparticles for various annealing conditions, Applied Physics A. 108 (2012) 607-613.

[2] Y. Zhou, Y. Wang, J. Wang, L. Lin, X. Wu, D. He, Controlled synthesis and characterization of hybrid Sn-doped Co_3O_4 nanowires for supercapacitors, Mater Lett. 216 (2018) 248-251.

[3] A. Din, K.S. Karimov, K. Akhtar, M.I. Khan, M.T.S. Chani, M.A. Khan, A.M. Asiri, S.B. Khan, Impedimetric humidity sensor based on the use of SnO_2–Co_3O_4 spheres, J. Mater. Sci. : Mater. Electron. 28 (2017) 4260-4266.

[4] S. Nie, D. Dastan, J. Li, W. Zhou, S. Wu, Y. Zhou, X. Yin, Gas-sensing selectivity of n-ZnO/p-Co_3O_4 sensors for homogeneous reducing gas, Journal of Physics and Chemistry of Solids. 150 (2021) 109864.

[5] A.V. Koroleva, A.S. Ilin, V.V. Smirnova, M.N. Martyshov, V.B. Platonov, M.N. Rumyantseva, P.A. Forsh, P.K. Kashkarov, Effect of Zn Doping on Structure and Electrical Properties in Co_3O_4/Zn Nanocomposites with Different Morphology, ChemistrySelect. 8 (2023) e202301785.

[6] K. Li, X. Chang, X. Qiao, S. Yu, X. Li, F. Xia, Q. Xue, Bimetallic metal–organic frameworks derived hierarchical flower-like Zn-doped Co_3O_4 for enhanced acetone sensing properties, Appl. Surf. Sci. 565 (2021) 150520.

[7] L. Du, H. Sun, Y. Liu, Metal-organic framework-derived hierarchical flower-like Mo-doped Co_3O_4 for enhanced triethylamine sensing properties, J. Alloys Compounds. 900 (2022) 163470.

[8] A.S. Tale, S.D. Thakre, Effect of Sn Doping on Structural Properties of Cobalt Oxide Nanoparticles Synthesized by Sol Gel Method.

[9] H. Albargi, R. Marnadu, G. Sujithkumar, A.S. Alkorbi, H. Algadi, M. Shkir, A. Umar, G. Sreedevi, Deposition of nanostructured Sn doped Co_3O_4 films by a facile nebulizer spray pyrolysis method and fabrication of p-Sn doped Co_3O_4/n-Si junction diodes for opto-nanoelectronics, 332 (2021) 113067.

[10] L. Wang, J.C. Xu, Y.B. Han, H.X. Jin, B. Hong, D.F. Jin, J. Gong, X.L. Peng, H.L. Ge, X.Q. Wang, Nanocasting synthesis and highly-improved toluene gas-sensing performance of Co_3O_4 nanowires with high-valence Sn-doping, Chem.Phys. 560 (2022) 111573.

[11] M. Mayakannan, S. Gopinath, S. Vetrivel, Synthesis and characterization of antibacterial activities nickel doped cobalt oxide nano particles, Mater.Chem.Phys. 242 (2020) 122282.

[12] R. Sharma, D.P. Bisen, U. Shukla, B.G. Sharma, X-ray diffraction: a powerful method of characterizing nanomaterials, 4 (2012) 77-79.

[13] X. Tong, Z. Hai, D. Cui, L. Gao, Q. Zhang, H. Xu, Y. Ma, C. Xue, J. Liu, Investigation of lattice distortion of Co_3O_4 nanoparticles prepared by a carbon-assisted method, 159 (2016) 17-20.

[14] H. Sun, L. Liu, Metal-Organic frameworks-derived 2D spindle-like Sn-doped Co_3O_4 porous nanosheets as efficient materials for TEA detection, Sensors Actuators B: Chem. 338 (2021) 129825.

[15] L. Xu, G. Zheng, F. Xian, J. Su, The morphological evolution of ZnO thin films by Sn ions doping and its influence on the surface energy and photocatalytic activity, Mater.Chem.Phys. 229 (2019) 215-225.

[16] G. Furlanetto, L. Formaro, Precipitation of Spherical Co_3O_4 Particles, J.Colloid Interface Sci. 170 (1995) 169-175.

[17] C.S. Jincy, P. Meena, Synthesis, characterization, and NH_3 gas sensing application of Zn doped cobalt oxide nanoparticles, 120 (2020) 108145.

[18] S. Fareed, R. Medwal, J.V. Vas, I.A. Khan, R.S. Rawat, M.A. Rafiq, Tailoring oxygen sensing characteristics of Co_3O_4 nanostructures through Gd doping, Ceram.Int. 46 (2020) 9498-9506.

[19] J. Zhang, J. Ling, K. Gu, G.G. Levchenko, X. Liang, Enhanced xylene sensing performance of hierarchical flower-like Co3O4 via In doping, 32 (2023) 068104.

[20] C. Qin, Z. Wei, B. Wang, Y. Wang, Sn and Mn co-doping synergistically promotes the sensing properties of Co_3O_4 sensor for high-sensitive CO detection, Sensors Actuators B: Chem. 390 (2023) 133930.

[21] M.M. Rahman, A.Z. Shafiullah, A. Pal, M.A. Islam, I. Jahan, B.B. Saha, Study on optimum IUPAC adsorption isotherm models employing sensitivity of parameters for rigorous adsorption system performance evaluation, 14 (2021) 7478.

[22] K. Shingange, H.C. Swart, G.H. Mhlongo, H_2S detection capabilities with fibrous-like La-doped ZnO nanostructures: A comparative study on the combined effects of La-doping and post-annealing, J.Alloys Compounds. 797 (2019) 284-301.

[23] P. Qiao, L. Zhang, M. Zhu, Y. Yin, Z. Zhao, H. Sun, J. Dong, L. Bie, Acetylene sensing enhancement of mesoporous ZnO nanosheets with morphology and defect induced structural sensitization, Sensors Actuators B: Chem. 250 (2017) 189-197.

[24] A. Boontum, D. Phokharatkul, J.H. Hodak, A. Wisitsoraat, S.K. Hodak, H_2S sensing characteristics of Ni-doped $CaCu_3Ti_4O_{12}$ films synthesized by a sol-gel method, Sensors Actuators B: Chem. 260 (2018) 877-887.

[25] M.C. Biesinger, B.P. Payne, A.P. Grosvenor, L.W. Lau, A.R. Gerson, R.S.C. Smart, Resolving surface chemical states in XPS analysis of first row transition metals, oxides and hydroxides: Cr, Mn, Fe, Co and Ni, Appl.Surf.Sci. 257 (2011) 2717-2730.

[26] L.S. Sundar, G.O. Irurueta, E.V. Ramana, M.K. Singh, A. Sousa, Thermal conductivity and viscosity of hybrid nanfluids prepared with magnetic nanodiamond-cobalt oxide (ND-Co_3O_4) nanocomposite, 7 (2016) 66-77.

[27] C. Linder, S.G. Rao, A. Le Febvrier, G. Greczynski, R. Sjövall, S. Munktell, P. Eklund, E.M. Björk, Cobalt thin films as water-recombination electrocatalysts, 404 (2020) 126643.

[28] G. Greczynski, L. Hultman, Self-consistent modelling of X-ray photoelectron spectra from air-exposed polycrystalline TiN thin films, Appl.Surf.Sci. 387 (2016) 294-300.

[29] S.F. Shen, M.L. Xu, D.B. Lin, H.B. Pan, The growth of urchin-like Co_3O_4 directly on sensor substrate and its gas sensing properties, Appl.Surf.Sci. 396 (2017) 327-332.

[30] S. Bai, J. Guo, X. Shu, X. Xiang, R. Luo, D. Li, A. Chen, C.C. Liu, Surface functionalization of Co_3O_4 hollow spheres with ZnO nanoparticles for modulating sensing properties of formaldehyde, Sensors Actuators B: Chem. 245 (2017) 359-368.

[31] B.R. Thamaga, T.J. Theka, R.G. Motsoeneng, L. Coetsee-Hugo, H.C. Swart, D.E. Motaung, Remarkable surface area engineering of nanosheet-assembled hierarchical pn Ag-loaded NiO-CeO_2 heterostructure for superior ethanol sensing performance, J.Alloys Compounds. 976 (2024) 173110.

[32] R.S. Dima, D.M. Tshwane, K. Shingange, R. Modiba, N.E. Maluta, R.R. Maphanga, Adsorption of NH_3 and NO_2 Molecules on Sn-Doped and Undoped ZnO (101) Surfaces Using Density Functional Theory, 10 (2022) 2027.

[33] J.P. Perdew, Density functional theory and the band gap problem, 28 (1985) 497-523.

[34] S. Selcuk, A. Selloni, DFT U study of the surface structure and stability of Co_3O_4 (110): dependence on U, 119 (2015) 9973-9979.

[35] D. Liu, E. Pervaiz, S. Adimi, T. Thomas, F. Qu, C. Huang, R. Wang, H. Jiang, M. Yang, Theoretical study on W-Co_3O_4 (1 1 1) surface: Acetone adsorption and sensing mechanism, Appl.Surf.Sci. 566 (2021) 150642.

[36] V. Kumar, J. Jung, Enhancement of gas sensing by doping of transition metal in two-dimensional As_2C_3 nanosheet: A density functional theory investigation, Appl.Surf.Sci. 599 (2022) 153941.

[37] M. Singla, D. Sharma, N. Jaggi, Effect of transition metal (Cu and Pt) doping/ co-doping on hydrogen gas sensing capability of graphene: A DFT study, Int J Hydrogen Energy. 46 (2021) 16188-16201.

[38] Y. Li, Y. Xu, X. Li, The sensing mechanism of HCHO gas sensor based on transition metal doped graphene: Insights from DFT study, 338 (2022) 113460.

[39] Y. Qin, Z. Ye, DFT study on interaction of NO_2 with the vacancy-defected WO_3 nanowires for gas-sensing, Sensors Actuators B: Chem. 222 (2016) 499-507.

[40] S. Navale, M. Shahbaz, A. Mirzaei, S.S. Kim, H.W. Kim, Effect of Ag addition on the gas-sensing properties of nanostructured resistive-based gas sensors: an overview, 21 (2021) 6454.

Chapter 6

Conclusion and future work

6.1 Conclusion

In summary, pristine Co_3O_4 sheet-like structures were successfully synthesized through hydrothermal technique by varying the oven duration as 6, 12 and 24 hours and the products were labelled Co_3O_4_6hrs Co_3O_4_12hrs and Co_3O_4_24hrs, respectively. Gas sensing tests revealed high response and selectivity to ethylene (C_2H_4), with the Co_3O_4_6hrs sensor exhibiting the highest response of 49.6 and rapid response/recovery times of 27/42 s. The good gas sensing performance of Co_3O_4_6hrs was attributed to the combination of high surface area and significant defects observed from BET and PL characterizations.

The doping effect of transitional metals namely Sn and Zn on Co_3O_4 structures was further investigated. Both dopants were successfully incorporated on the Co_3O_4 crystal lattice with evident presence of new extra peaks on the XRD at doping levels above 1wt% for Zn doped products, and new extra peaks at doping level from 0.5wt% for Sn doped products. SEM studies revealed that the incorporation of these dopants led to a change in morphology from uniform sheet-like structures morphology to hierarchical flower like morphology and exhibited increased surface area from BET. Further, XPS studies confirmed incorporation of these dopants and revealed high oxygen defects for Sn doped Co_3O_4 hierarchical structures. High surface area and large number of defects is beneficial for gas sensing as they provide more active sites for gas molecules adsorption/desorption processes. Some of the processes involved in gas sensing mechanisms such as adsorption cannot be studied experimentally, hence DFT calculations were employed for a better understanding of gas-surface reaction, detailing the gas sensing mechanism between Co_3O_4 (311) plane surface and C_2H_4 gas. Pure Co_3O_4 (311) surface was cleaved and optimised together with C_2H_4 gas molecules and adsorption simulations were ran. The adsorption energies of -1.440 eV and -1.428 eV for the pristine system were obtained for both physisorption and chemisorption approaches respectively. The observed negative values of the adsorption energies (E_{ads}) indicated strong adsorption interactions and stability.

Furthermore, the pristine Co_3O_4 (311) surface was doped with Sn and Zn, and their doping effect was investigated in both adsorption approaches. Their successful incorporation into the Co_3O_4 lattice led to increased adsorption energies to -1.526 eV (physisorption) and -1.457 eV (chemisorption) for Sn and

reduced adsorption energies to -1.407 eV (physisorption) and -0.689 eV (chemisorption) for Zn. The introduction of these dopants revealed distinct behaviors associated with each dopant which were attributed to the complex reactions between the material properties, surface structure, defects, and dopant effects. Sn has shown possible capabilities of enhancing gas sensing performance of Co_3O_4 for C_2H_4 detection.

6.2 Future work

This work has laid a solid foundation by combining both experimental and computational approaches, based on the findings and insights obtained several aspects for future research still need to be explored including:

- Consider lower Sn doping concentration to investigate the threshold concentration at which formation of new extra peaks start occurring, as Sn samples displayed two phases on the XRD ,not showing exactly at what concentration does Sn phase start from.
- Explore gas sensing studies experimentally to compliment the DFT studies and determine the effect of doping concentration.
- Usage of advanced computational modeling can be considered, by using advanced applications such as VASP and extending beyond DFT by looking at advanced methods such as molecular dynamics, this could provide more accurate results and representations of gas-surface interactions, assisting with a deeper understanding of the gas sensing mechanism.
- Another aspect to delve into is the long-term stability of Co_3O_4-based gas sensors over extended periods, this will help determine the durability and reliability these sensors.